

JOURNAL OF SCIENCES



University of Tehran

Abu Reyhan al-Biruni
(973-1048)
Iranian Scientist

ISLAMIC REPUBLIC OF IRAN

ISSN 1016-1104

Vol. 34, No. 3, Summer 2023

CONTENTS

INSTRUCTIONS TO AUTHORS	203
BIOLOGY:	
• Formulation and Evaluation of Gelatin Nanoparticle Moisturizing Gel from Mesocarp Extract of Watermelon [<i>Citrullus lanatus</i> (Thunb.) Matsum. & Nakai] as an Antioxidant	205
◦ S. D. Okzelia, S. A. Azzahara, K. Kosasih, S. I. Yanti	
CHEMISTRY:	
• Anticancer Effect and Safety Profile of a 4-Pyridyl Linked Triazolotriazine Derivative against Colorectal Tumor	217
◦ R. Monfared, S. Farzipour, S. Dadashpour, Z. Zakeri Khatir, S. J. Hosseinimehr, F. Talebpour Amiri, H. Irannejad	
GEOLOGY:	
• Microstructures and Crystal Size Distribution (CSD) of Chromites from Gysian Silvana Ophiolite Serpentinites, Urmia, Iran	227
◦ M. Modjarrad	
MATHEMATICS, STATISTICS, AND COMPUTER SCIENCES:	
• Heavy Tailed Distribution of Binary Classification Model	239
◦ D. M. Oladimeji, E. S. Oguntade, S. O. Olarenwaju	
• Bootstrap Confidence Intervals for the Parameter of the Poisson-Sujatha Distribution and Their Applications to Agriculture	247
◦ W. Panichkitkosolkul, and Ch. Ponkaew	
PHYSICS:	
• Qutrit Teleportation and Entanglement Evolved by the One-Axis Counter-Twisting Hamiltonian under the Intrinsic Decoherence	255
◦ A. Naji	
PERSIAN TRANSLATION OF ABSTRACTS	263



In the Name of Allah, the Beneficent, the Merciful

JOURNAL OF SCIENCES

ISLAMIC REPUBLIC OF IRAN

CHAIRMAN AND EDITOR

Mohammad Reza Noori-Dalooi, Ph.D.

EDITORIAL BOARD

Alireza Abbsai, Ph.D.

University of Tehran, Tehran, Iran

Abdolhossein Amini, Ph.D.

University of Tehran, Tehran, Iran

Aziz N. Behkami, Ph.D.

Shiraz University, Shiraz, Iran

Farshad Ebrahimi, Ph.D.

Shahid Beheshti University, Tehran, Iran

Hassan Ebrahimpzadeh, Ph.D.

University of Tehran, Tehran, Iran

Mehdi Ghandi, Ph.D.

University of Tehran, Tehran, Iran

Mehdi Khoobi, Ph.D.

Tehran University of Medical Sciences, Tehran, Iran

Hassan Mehdian, Ph.D.

Kharazmi University, Tehran, Iran

Mohsen Mohammadzadeh, Ph.D.

Tarbiat Modares University, Tehran, Iran

Mohammad Reza Noori-Dalooi, Ph.D.

Tehran University of Medical Sciences, Tehran, Iran

Abdolhamid Riazi, Ph.D.

Amir Kabir University, Tehran, Iran

Jafar Zafarani, Ph.D.

Isfahan University, Isfahan, Iran

Hossein Zakeri, Ph.D.

Kharazmi University, Tehran, Iran

EDITORIAL ASSISTANT

Zahra Roshani

MANAGERIAL ASSISTANTS

Hasan Noori-Dalooi

Elaheh Poorakbar

TYPESETTING AND LAYOUT

Ali Azimi

Journal of Sciences, Islamic Republic of Iran is published quarterly by The University of Tehran,

16th St., North Kargar Ave, Tehran, Islamic Republic of Iran

Tel.: (0098-21)88334188, 88012080-212

Fax: (0098-21) 88334188

P.O. Box 13145-478

http://jscienc.es.ut.ac.ir

E-mail: jscienc.es@ut.ac.ir

E-mail: nooridalooi@sina.tums.ac.ir

ISSN 1016-1104

Instructions to Authors

1. General Policy

The *Journal of Sciences, Islamic Republic of Iran (J. Sci. I. R. Iran)* is published quarterly by the University of Tehran. Contributions from all fields of basic sciences may be submitted by scientists from all over the world.

The papers submitted to this journal should not have been published previously, except in the form of a brief preliminary communication, nor submitted to another journal. The decision to accept a contribution rests with the Editorial Committee of the *J. Sci. I. R. Iran*. Manuscripts will be considered for publication in the form of articles, preliminary communications, notes and review articles. The work should be original or a through review by an authoritative person in a pertinent field.

2. Copyright

Submission of a manuscript implies that the author(s) agree to transfer copyright to the *J. Sci. I. R. Iran* when the contribution is accepted for publication. Reproduction of the text, figures, or tables of this journal is allowed only by permission of the Editorial Committee.

3. Preparation of Manuscripts

3.1. General considerations. Manuscripts must be submitted in English according to Journal Instructions (It is necessary to submit at least 2 files including "Title page" and "Main file"). They **must be** typewritten in **Microsoft Word** (all versions). Authors are requested to reserve margins of at least 3 cm at the top and bottom of each page and at least 4 cm on the left-hand side.

Tables and illustrations (both numbered in Arabic numerals) should be prepared on separate pages. Tables require a heading and figures a legend, also prepared on a separate page. In Electronic submission, figures should be with the following caveats: all figures should be submitted at a minimum of 300 dpi and saved as TIFF files (avoid submitting JPEG files) after your text file.

Manuscripts should be kept to a minimum length and should be subdivided into labeled sections (**Introduction, Materials and Methods, Results, Discussion, Acknowledgement, References**). A current issue of *J. Sci. I. R. Iran* should be consulted.

3.2. Title page. The title of a manuscript should reflect concisely the purpose and findings of the work in order to provide maximal information for a computerized title search. Abbreviations, symbols, chemical formulae, references, and footnotes should be avoided.

The authors' full first names, middle initials and last names should be given, followed by the address(es) of the contributing department(s). (e.g. Department, Faculty, University, City, Country).

Telephone, Fax and Email of corresponding author should be footnoted on the bottom of the first page of each manuscript. Footnotes may be added to indicate the present mailing address(es) of the author(s). (e.g. *Corresponding author, Tel: 00982188012080, Fax: 00982188012081, E-mail: jsciences@ut.ac.ir).

Special types of print should be indicated as follows:

Type	Mark	Symbol	Example	Example (Printed)
Boldface ^a	Single underline	—	<u>Introduction</u>	Introduction
Italic ^b	Wave-like underline	~	<u>In vivo</u>	<i>In vivo</i>
Small capital ^c	Double underline	==	0.2 <u>m</u>	0.2 M
Boldface italic ^d	Underline with wavy line	~	<u>R</u>	<i>R</i>

a) Headings, designated numbers of chemical compounds, subheadings.

b) Configurational prefixes ((R)-, (S)-, cis-, trans-, tert-, etc); Latin words or abbreviations, words in languages other than English; trade names of compounds (first letter should be capitalized); names of authors if mentioned in the text.

c) Symbols of molar and normal concentrations (M and N), D- and L-, the names or initials of the nomenclature of species.

d) Italicized terms and prefixes in headings.

The total number of pages (including references, tables, copies of formula collections (if any), schemes and figures should be marked in the upper left-hand corner of the first page of each copy. The complete address, including phone number, and E-mail address of the correspondence author should also be given.

3.3. **Main File:**

a) The title of the article (The first letter of each word must be capital).

b) Abstract should be self-explanatory and intelligible without references to the text and titles, it must not exceed 250 words.

c) At least between three to five keywords should be chosen by the author(s).

d) Introduction

e) Materials and Methods

f) Results and Discussion (they can be separate section too)

g) Figures and Tables (if There are any)

Theoretical articles must have atleast two main title : Introduction and Results.

3.4. *References.* References may be numbered alphabetically or sequentially in the order they are cited in the text. References typed with double spacing are to be listed in numerical order at the end of the main text. They should be addressed according to the following examples:

Journals:

Noori-Daloi M.R., Swift R.A., Kung H.J., Crittenden L.B., and Witter R.L. Specific integration of REV proviruses in avian bursal lymphomas. *Nature*, **294** (5841): 574-576 (1981).

Noori Daloi M.R., Saffari M., Raoofian R., Yekaninejad M., Saydi Dinehkabodi O., and Noori-Daloi A.R. The multidrug resistance pumps are inhibited by silibinin and apoptosis induced in K562 and KCL22 leukemia cell lines. *Leukemia Research*, **38** (5): 575-580 (2014).

Books:

Rang G.M. and Petrocelli S.R. *Fundamentals of Aquatic Toxicology*. Hemisphere Publishing Corporation, New York, 1129 p. (1991).

Chapters in Books:

Walsh J.H. Gastrointestinal hormones. In: Johnson L., Christensen J., Jackson M., Jacobson E., and Walsh J.H. (Eds.), *Physiology of the Gastrointestinal Tract*, 2nd Ed., Raven, New York, pp. 181-254 (1987).

Thesis:

Kossir A. Extraction liquid-liquid du Zinc (II) en milieu cyanure. Application ala valorization des mineraux de zinc oxides, Ph.D. *Thesis*, University of Paris (VI), 116 p. (1991).

Please note that papers with incorrect formatted references will be returned.

4. Forwarding Address

Manuscripts should be submitted to the journal site (<http://jsciences.ut.ac.ir>).

M.R. Noori-Daloi, Ph.D.
J. Sci. I. R. Iran
University of Tehran
P.O. Box 13145-478 Tehran, I. R. Iran
<http://jsciences.ut.ac.ir>
E-mail: jsciences@ut.ac.ir

Formulation and Evaluation of Gelatin Nanoparticle Moisturizing Gel from Mesocarp Extract of Watermelon [*Citrullus lanatus* (Thunb.) Matsum. & Nakai] as an Antioxidant

S. D. Okzelia^{1*}, S. A. Azzahara¹, K. Kosasih², S. I. Yanti¹

¹ Department of Pharmacy, Universitas Bani Saleh, Bekasi, Indonesia

² Faculty of Pharmacy, Universitas Pancasila, Jakarta, Indonesia

Received: 22 November 2022 / Revised: 13 June 2023 / Accepted: 20 June 2023

Abstract

Human skin might get attacked by free radicals therefore, antioxidants are needed. Mesocarp of watermelon [*Citrullus lanatus* (Thunb.) Matsum. & Nakai] has natural antioxidant compounds such as citrulline. Antioxidant compounds were formulated into gel preparation with nanoparticle technology that aimed to facilitate the absorption of an active substance. The purpose of this study was to formulate an antioxidant moisturizing gel that contained gelatin nanoparticles of mesocarp extract of watermelon (GNMW). The stages of research included the extraction, production, and characterization of nanoparticles, formulation of gel preparations with various concentrations of 0.0114% (F1), 0.0228% (F2), and 0.0342% (F3), evaluation of gel preparations, observation of antioxidant activity using DPPH method and skin moisture test. The nanoparticles produced had an irregular shape, size of 200.3 nm, polydispersity index of 0.288, and zeta potential value of +16.11 mV. The nanoparticle gel had a slightly viscous texture, clear color, and homogeneous, with a pH value of 6.61 – 7.22; viscosity of 14740 – 17180 cP; spread-ability of 5.3-6.5 cm; and did not irritate the skin. The results of the antioxidant activity of the extract and nanoparticles were 110.90 µg/mL and 114.16 µg/mL, respectively. Nanoparticle gel of F1, F2, and F3 had IC₅₀ values of 149.52 µg/mL; 138.44 µg/mL; and 127.10 µg/mL, respectively. The gels could increase skin moisture content in the range of 38.81% - 63.19%. Mesocarp extract of watermelon which was made into nanoparticles with gelatin carrier could be formulated into a moisturizing gel, met good gel parameter standards, and had moderate antioxidant activity.

Keywords: Nanoparticle moisturizing gel; GNMW; Nanoparticle antioxidant gel.

Introduction

The skin is the outermost part that covers all parts of the body. Antioxidants are needed to protect the body from free radical attacks such as UV rays. One natural product that has the potential as a natural antioxidant and is believed to neutralize free radical in the human body is watermelon (*Citrullus lanatus*). This fruit is in high

demand because of its sweet and fresh taste and can be functioned as a skin moisturizer. Due to the high demand for watermelon consumption, the large amount of watermelon peel waste has also increased. Waste produced from watermelon white peel (mesocarp) is about 30% per fruit (1). The mesocarp of watermelon (MW) has a natural antioxidant compound in the form of citrulline, which is higher than its endocarp (flesh of

* Corresponding author: Tel: +6281374281562; Email: sd.okzelia@gmail.com

watermelon) by 60% or about 15.6 mg/g dry weight.

MW was reported to contain flavonoid compounds that can act as an antioxidant also with an IC_{50} value of 31.42 $\mu\text{g/mL}$ (2). One of the topical dosage forms that have been developed is gel. A gel is a semisolid-shaped preparation made from small inorganic particles or large organic molecules and penetrated by a liquid. One of the important factors in gel formulation is the selection of a gelling agent. Fujiastuti & Sugihartini have formulated a gel preparation contained *Centella asiatica* L extract in various type of gelling agent such as HPMC, Carbopol and CMC sodium. The result showed that Carbopol was the best type of gelling agent because it gave the strongest adhesive power and minimal irritation effects (3). Carbopol expands when dispersed in air in the presence of alkaline substances such as triethanolamine or diisopropanol amine to form semisolid preparations. Carbopol behaves like a non-Newtonian fluid, but as long as the shear stress is below certain values, the gel will not flow and reversible, elastic deformation will occur (4).

Nowadays, many topical dosage industries compete for the maximum ability of the active substance. Nanoparticle technology has become a new trend in the development of drug delivery systems because it has the advantage that is easier to pass through intracellular spaces.

Mahmoudi et al. showed that the modification of *Physalis alkekengi* L. extract into nanoparticle could increase antioxidant activity (5). Biopolymers that have been widely used as carriers in nanoparticle technology are gelatin because they have good biocompatibility and biodegradability properties. Gelatin is a protein obtained from the hydrolysis of collagen. Gelatin has several advantages, such as low cost, easy bioavailability, opportunities to be combined with crosslinkers, easily decomposed, and has the ability to interact with cells without causing toxicity (6). Nejat et al. showed that gelatin could be used to prepare cardamom extract-loaded gelatin nanoparticles as an effective targeted drug delivery system to treat glioblastoma (7).

Formulation of gelatin nanoparticles containing mesocarp extract of watermelon [*Citrullus lanatus* (Thunb.) Matsum. & Nakai] is of great necessity. This study aimed to utilize watermelon peel waste through the formulation of a gel preparation that has an antioxidant activity which is made into a nanoparticle preparation with a gelatin carrier. To the best of our knowledge, no studies have previously been conducted on the formulation of gelatin nanoparticles containing mesocarp extract of watermelon as an antioxidant for gel preparation. Measurement of antioxidant activity was carried out using the DPPH (2,2-diphenyl-1-picrylhydrazyl) method. The DPPH method was chosen

because it is simple, easy, fast, sensitive, and requires a small number of samples.

Materials and Methods

1. Chemicals and plant materials

DPPH (2,2-diphenyl-1-picrylhydrazyl), ascorbic acid, DMSO (Dimethyl Sulfoxide) and acetone solvent were purchased from Sigma Aldrich (USA). Other chemicals were obtained from the chemical warehouse of the Pharmacy Department, Sekolah Tinggi Ilmu Kesehatan Bani Saleh with pharmaceutical grade. Mesocarp of watermelon sample was obtained from fresh watermelons at watermelon plantations in Saptomulyo Village, Kota Gajah, Lampung Province, Indonesia.

2. Simplicia preparations

Fresh watermelon fruits were cut and separated between the mesocarp and endocarp. MW then washed, cut into cubes with the size of 1 cm x 1 cm x 1 cm, and dried under indirect sunlight for 7 days. Dried MW was then crushed until a powder of certain fineness was obtained (2). Powdered MW was macroscopically observed, including color, odor, and shape, and then observed the fineness degree using a sieving pan.

3. Extraction of the simplicia

Specific weights (1.20 kg) of powdered MW were macerated using 70% ethanol in ratio of 1:10 for 2x24 hours with occasionally stirred, then stored in a dark or sun-tight room and filtered. The residue was then re-macerated and the filtrates in each maceration process were gathered and evaporated using a rotary evaporator until a concentrated extract of MW was obtained (8).

4. Characterization of extract

Water content, pH, solubility, and phytochemical screening were carried out toward the extract of MW.

5. Phytochemical screening

Phytochemical screening including alkaloids, flavonoids, saponins, steroids/triterpenoids and tannins was carried out toward the extract of MW.

A specific amount (0.6 g) of MW extract was added 3 mL of 2 N HCl solution, then divided into 3 test tubes. Mayer's, Dragendorff's, and Wagner's reagent were added to each tube sequentially, then the changes that occurred were observed. Alkaloids are positive if there is a precipitate or color change in at least two of the three experiments above. The positive reaction of alkaloids is the formation of a yellow or white precipitate with Mayer's reagent, an orange precipitate with Dragendorff's reagent, and the formation of a reddish-brown color with

Wagner's reagent (9).

A specific amount (0.2 g) of MW extract was added with 1 mL of concentrated HCl and 0.2 g of Mg powder. The positive reaction of flavonoids is indicated by the formation of red, orange, or yellow color (9).

A specific amount (0.5 g) of MW extract was added 10 mL of hot water, cooled, then shaken vigorously for 10 seconds. The positive reaction of saponins is indicated by the formation of 1 – 10 cm foam which is stable for not less than 10 minutes and does not disappear with the addition of 1 drop of 2 N HCl (9).

A specific amount (0.2 g) of MW extract was added with Liebermann-Burchard reagent. The positive reaction of steroids is indicated by the formation of a greenish blue color whereas the positive reaction of triterpenoids is indicated by the formation of purple color (9).

A specific amount (0.1 g) of MW extract was added 10 mL of hot water, boiled, and filtered. To the filtrate, 2 drops of gelatin 1% was added. The positive reaction of tannins is indicated by the formation white precipitate (9).

6. Gelatin nanoparticle of MW preparation

Gelatin nanoparticle was made by the desolvation method as described by Coester et al. with modification (10). A specific amount (100 mg) of MW extract was dissolved in a mixed solvent (15 mL of ethanol and 10 mL of DMSO). A specific amount (100 mg) of gelatin was dissolved in 25 mL of water with constant heating at a temperature of 40 °C using a magnetic stirrer at speed of 1000 rpm until a clear solution was obtained. The gelatin solution was then adjusted its pH until 3 with the addition of 0.1 M HCl or 0.1 M NaOH solution. MW extract solution was then added to the gelatin solution followed by the addition of Pluronic F-68 (300 mg) while stirring continuously using magnetic stirrer at speed of 1000 rpm. 30 mL acetone were then added drop by drop. After 10 minutes, 0.2 mL of glutaraldehyde was added then stirred for 3 hours at a temperature of 40 °C to bind the nanoparticles. Nanoparticles were then purified by being placed into a dialysis tube soaked with water for 24

hours. Furthermore, nanoparticles were dried using freeze dryer at a constant temperature of -45 °C (11). An organoleptic test of gelatin nanoparticle of MW (GNMW) was carried out.

7. GNMW characterization

GNMW was characterized by its particle size and polydispersity index using a Particle Size Analyzer at 20° C (12), zeta potential, morphology using Scanning Electron Microscope, solubility, and functional group using Fourier Transform Infrared Spectrophotometer.

8. Gel preparation

Water was heated at a temperature of 70 °C. A specific weight (0.5 mL) of Carbopol 940 was developed with 20 times of hot water for 30 minutes, then stirred quickly in the mortar until a gel mass was formed. Specific weights (2 g) of TEA (triethanolamine) were added and then ground until homogenous. A specific weight (0.5 mL) of phenoxyethanol was dissolved with 15 mL of propylene glycol and 0.1 g of sodium metabisulfite with 5 mL of water, then placed in the mortar and stirred until homogenous. GNMW was dissolved with the remaining water, placed in the mortar and stirrer until homogenous then added with water until 100 g (13). Formulation of GNMW gel is shown in Table 1.

9. Evaluation of GNMW gel

Evaluation of GNMW gel included organoleptic test, pH, homogeneity, viscosity, spread-ability, irritation test, humidity test, and antioxidant activity test using the DPPH method.

10. Irritation test

Irritation test was performed on 10 volunteers (male and female), who were selected by age criteria of 20-35 years old and never had skin problems before (14). GNMW gel of F0, F1, F2, and F3 were applied on the upper forearm, covered with gauze, and plastered. After being left for 1 hour, the plaster was opened and seen for the symptoms caused such as itching, redness, or

Table 1. Gel formulation of GNMW

Substances	Formulation				Function
	F0	F1	F2	F3	
GNMW (%)	-	0.0114	0.0228	0.0342	Active ingredients
Carbopol 940 (%)	0,5	0,5	0,5	0,5	Gelling agent
TEA (%)	1	1	1	1	Buffer
Propylene glycol (%)	15	15	15	15	Humectant
Phenoxyethanol (%)	0,5	0,5	0,5	0,5	Preservative
Sodium metabisulfite (%)	0,1	0,1	0,1	0,1	Antioxidant
Water (%)	ad 100	ad 100	ad 100	ad 100	Solvent

swelling (15).

11. Skin moisture test

A skin moisture test was performed on 10 volunteers. Volunteers were conditioned at room temperature for 30 minutes (16). Five areas of 6 cm² were marked (17). Before applying the GNMW gel, a moisture test was conducted on dull forearm skin. GNMW gel of F0, F1, F2, and F3 were applied on the forearm. The negative control was the dull forearm skin. Skin moisture was measured hourly for 3 hours using Skin Moisture Analyzer (18).

12. Antioxidant activity assay

Antioxidant activity assay was carried out toward MW, GNMW, and GNMW gel preparations using vitamin C as the positive control. A specific amount of samples (1 mL) were added by 1 mL of DPPH solution and 3 mL of ethanol, homogenized by a vortex mixer for 1 minute then incubated at 37 °C for 30 minutes. Absorbance was measured at a maximum wavelength of 517 nm with a UV-Vis Spectrophotometer. The experiment was performed 3 times for replication. The IC₅₀ value was obtained from linear regression equation $y = ax + b$ where x was the concentration value of the sample solution and y was the percent inhibition against DPPH (19).

13. Statistical analysis

To estimate the statistical significance of the measured values, ANOVA (Analysis of Variance) was performed using SPSS v. 22 including the data of normality, homogeneity, spread-ability, pH, viscosity and antioxidant activity. The data obtained from antioxidant activity tests were calculated for IC₅₀ value using linear regression method.

ANOVA was performed to estimate the statistical significance of the measured values, including IC₅₀ value. Shapiro-Wilk test was performed to determine the normality of the data, while Levene statistical test was performed to determine the homogeneity of the data.

Results and Discussion

1. *Simplicia* preparations

A total amount of 27.63 kg of MW was cut into cubes to support the drying process. The drying process aimed to extend the shelf life of *Simplicia*. Dried MW was crushed to produce smaller particle sizes so the extraction process would be more effective. The finer the *simplicia* powder produced, the larger the surface area of the powder, so the higher the contact between the powder and the solvent. The dried *Simplicia* obtained was stored

at a temperature of 15-30 °C. Dried MW was a powder, brownish-yellow color, and had a characteristic odor.

2. Extraction of the *simplicia*

Maceration was carried out for the extraction process. The principle was “*like dissolved like*”, which meant that a compound would be dissolved in a solvent with the same properties. The maceration method was chosen because of the simple and practical extraction process. Stirring during the maceration process was carried out to homogenous the concentration of the solution and could optimize the secondary metabolite retrieval. In the maceration process, *Simplicia* would undergo a breakdown of the cell wall due to the pressure difference between inside and outside the cell, so that the secondary metabolites present in the cytoplasm would be dissolved in organic solvent (20). 70% ethanol was used as a solvent in the maceration process because it could attract both polar and nonpolar compounds, and is nontoxic compared to other solvents. Remaceration was carried out to fully retrieve the secondary metabolite contained in the sample. The filtrate obtained was a solid green color. The macerates were then evaporated to produce a concentrated extract. The final result of this extraction process was a reddish-brown thick extract of MW with a yield of 25.025%. MW extract was viscous, reddish-brown in color, and had a characteristic odor.

3. Characterization of extract

The water content of the MW extract was 19.51% which met the standard value of good water content for viscous extracts (5-30%). High water content could facilitate microbial growth.

The pH of MW extract was obtained at 5.13 which tent to be acidic. The optimum pH value for the production of gel preparation is 4-7. Too high a pH value would cause the gel to be less stable.

A solubility test was carried out to determine the degree of solubility of extracts in various solvents as well as to determine the polarity of extracts that would have an effect when selecting solvents for the manufacture of nanoparticle and gel preparations.

Based on the results of the solubility test, MW extract was very soluble in water and propylene glycol, soluble in ethanol and DMSO, and very slightly soluble in acetone.

Phytochemical screening was necessary to identify the class of secondary metabolite compounds of GNMW extract. The phytochemical screening results stated that MW extract contained alkaloids, flavonoids, and saponins compounds. The result is shown in Table 2.

Table 2. Secondary metabolites screening result of MW extract

Secondary metabolite compound	Reagent	Result
Alkaloid	Mayer	-
	Dragendorff	+
	Wagner	+
Flavonoid	Wilstatter	+
	FeCl ₃ 1%	-
Tannin	Water	+
Saponin	Liebermann-Burchard	-
Steroid	Liebermann-Burchard	-
Terpenoid		

(+) : Contain secondary metabolite compound

(-) : Did not contain secondary metabolite compound

4. GNMW preparation

The production of GNMW was carried out by the desolvation method which is a bottom-up type nanoparticle formation method. The synthesis of nanoparticles was conducted from small molecules size and then forming larger particles using chemical methods. The desolvation method was chosen because it was more economical, non-toxic, and easy to apply by using two types of solvents to avoid damaging factors including increased flow rate, heating, and stirring which could interfere with the tertiary structure of the protein from gelatin. The extract was dissolved with a mixed solvent in the form of ethanol and DMSO, aimed to dissolve the secondary metabolite compounds contained in the extract. A mixed solvent was used to completely dissolve the extract with gelatin solution which could easily attach to the nanoparticles formed (21).

Gelatin is a protein obtained through the hydrolysis of collagen from the skin, white connective tissue, and cartilage. The gelatin used was type B gelatin, because it has better potential in terms of delivery (4). Type B gelatin is obtained from bovine bones through alkaline hydrolysis which has an isoelectric point (IEP) value of 4-5 (22). Gelatin is denatured at temperatures above 37 °C but its molecular weight also does not change at that temperature so this study was performed at a temperature of 40 °C to dissolve gelatin with water (23).

The extract solution was then mixed into the gelatin solution. Production of GNMW was carried out using a magnetic stirrer at a temperature of 40 °C and a speed of 1000 rpm. The increasing speed of stirring, the smaller the particle size and the low value of the polydispersity index formed, due to the increased surface stabilization to prevent aggregation (11). Pluronic F-68 was then added to the mixed solution which functions as a surfactant that could increase the dissolution rate of the active substance by lowering the aggregation of active substance particles, resulting in good stability. The mixed solution of MW extract, gelatin, and pluronic F-68 was then set at its pH until 3. The pH adjustment aimed to keep the polymer away from its isoelectric point so that

gelatin did not easily form aggregates allowing for an increase in zeta potential. The smaller the pH value, the smaller the size of the nanoparticle because the maximum solubility of gelatin was at a pH value far from its isoelectric point (pH 4-5 for type B gelatin) (11).

Acetone was added as a desolvating agent. The addition of acetone drop by drop caused turbidity of the gelatin solution so that high and low-weight gelatin molecules could separate and indicated the formation of nanoparticles (24). The use of acetone as a desolvating agent is more effective in the synthesis of nanoparticles because the hydrophobic bond in gelatin increases so that the desolvation process is more effective and produced a low polydispersity index (25). The addition of glutaraldehyde as a cross-linking agent has the potential to improve the stability of particles and emulsions (26), beside that, it can also reduce solubility and decrease decomposition speed, and increase mechanical strength because gelatin has low mechanical strength and fast decomposition speed if used in nanoparticle synthesis (27). Glutaraldehyde has an aldehyde group (-CHO) that reacted with the amino group of gelatin, resulting in the formation of an aldimine bond (CH=N). One molecule of glutaraldehyde can bind to two amine groups.

The GNMW solution was then stirred for 3 hours using a magnetic stirrer. The particle size was directly proportional to the length of stirring time. The longer the stirring process, the smaller the particle size that will be produced. The increase in the length of stirring time caused the greater strength of the solvent molecules to contact with gelatin so that more and more particles split into nano-sized particles (28). The nanoparticle solution was then purified by the dialysis method using a dialysis tube soaked in water for 24 hours. The water of dialysis baths was changed every 2 hours. Dialysis tubes served to separate particles with different molecular weights. Larger molecular weights could be retained and smaller molecular weights would be liberated (29). The dialysis tube used had a molecular weight of 12 kDa, while the average relative molecular weight of commercial gelatin is between 20-70 kDa so that gelatin nanoparticles could

be retained by the pores of the dialysis tube and produced a purer nanoparticle solution. The resulting nanoparticles were in the form of suspensions, yellowish-clear in color with a characteristic odor.

5. GNMW characterization

Measurement of particle size and polydispersity index was carried out based on the Dynamic Light Scattering (DLS) method. This method is usually used for the measurement of suspended particles in liquids. The advantage of this method is that it can analyze very small samples of less than 3 μL . DLS works based on the principle of measuring Brownian particle motion, which is the free movement of particles due to friction from the surrounding solvent molecules. The particle size obtained was 200.3 nm. The requirements for the size of the nanoparticles needed in the drug delivery system are 50-300 nm (30). It could be concluded that the particle size met the requirements. The increase in particle size could be affected by the pH value and stirring speed.

The polydispersity index value shows a description of the particle size distribution. The polydispersity index value provides information about the stability of the dispersion system formed for a longer period and the drug release profile (31). The particle size is said to be uniform if the value of the polydispersity index is small. The requirement for the value of the polydispersity index of nanoparticles is 0-1. If the value of the polydispersity index is close to 1, it indicates that the particle size distribution shows high diversity and contains large particles or aggregates that have precipitated. A polydispersity index value of 0-0.5 indicates a uniform particle size distribution (32). The polydispersity index value was 0.288. It could be concluded that the polydispersity index value met the requirements and was monodispersed which indicated that GNMW had a uniform particle size distribution so they tend to be stable.

Zeta potential is a parameter of electric charge between colloidal particles which is influenced by changes in the interface with the dispersing medium, due to the dissociation of functional groups on the particle surface or ionic absorption that appears in the liquid dispersion medium and the occurrence of the solvation effect. Zeta potential was measured using the Electrophoretic Light Scattering (ELS) technique or Laser Doppler Microelectrophoresis. When the suspension is given an electric current, every charged particles will move at a speed and direction by its zeta potential value (32). The zeta potential measurement is said to be eligible if it has a zeta value less than -25 mV and greater than +25 mV because it has high stability and can prevent the formation of particle aggregation on the

surface charge (23). The zeta potential value of GNMW was +16.11 mV. The zeta potential was positive because the nanoparticles contain MW extract which made an acidic atmosphere. When the pH is low, the amine group (NH_4^+) in gelatin will react with glutaraldehyde. Positively charged nanoemulsions are more effective in the diffusion process inside the skin because the positively charged particles of the nanoemulsion system can carry the drug into the skin optimally and then encourage drug penetration through the skin. The level of skin binding with positively charged drugs is higher than with negatively charged drugs because it is known that the skin is negatively charged at neutral pH (34).

FTIR measurement on gelatin nanoparticles of MW extract showed that there was an interaction between gelatin and watermelon mesocarp extract, which was indicated by a shift in the wave number in the O-H group from 3267.57 cm^{-1} for MW extract and 3286.78 cm^{-1} for gelatin to 3377.47 cm^{-1} . The shift of the amide band ($\text{C}=\text{O}$), arose from the stretching vibration of the N-H group which was combined with the -OH group through hydrogen bonds. The wave number of the amide group shifted to a lower direction when a cross-linking agent such as glutaraldehyde was added. This was associated with the cleavage of hydrogen bonds to maintain the helical structure of gelatin (35). The result of FTIR is shown in Figure 1.

SEM characterization results showed that the size of all nanoparticles was in nanometers. The particle size measured by SEM was larger than that measured by DLS. This phenomenon could be happened because the intensity of Rayleigh scattering light is proportional to the sixth power of the diameter of nanoparticles. Hence, the signal of larger particles will be easy to record, and the smaller particles will be missed (36). The powder was sticky and piled up, resulting in an irregular shape. This is because the sample did not dry completely and shake well. The result of SEM is shown in Figure 2. The particle size measured by SEM was larger than that measured by DLS. This phenomenon could be happened because the intensity of Rayleigh scattering light is proportional to the sixth power of the diameter of nanoparticles. Hence, the signal of larger particle is easy to be recorded, and the smaller one will be missed.

6. GNMW drying method

The method used in the drying process of GNMW was freeze drying. Freeze drying method is the best method used in the development of pharmaceutical preparations because it is suitable for use in samples that are thermolabile so that it does not damage the compounds contained, produces more attractive colors, and is more stable in quality (no changes in odor, color,

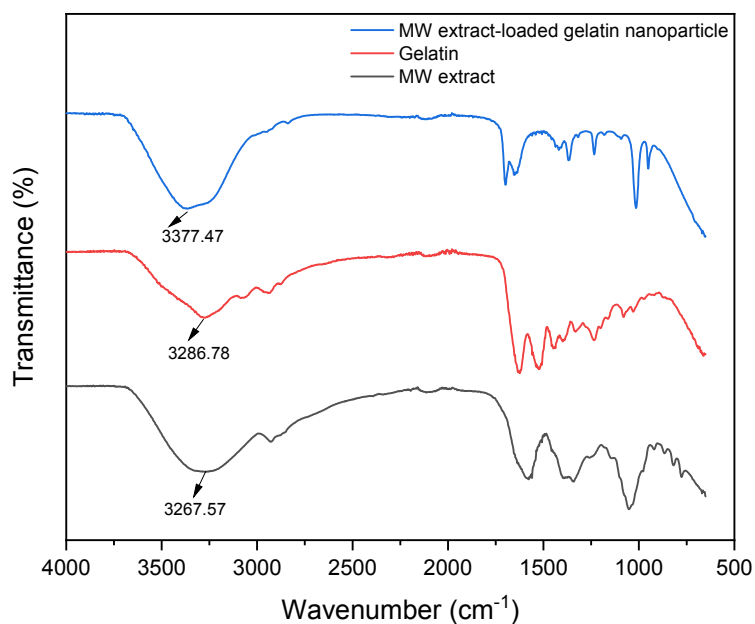


Figure 1. FTIR spectra of MW extract, gelatin, and MW extract-loaded gelatin nanoparticle

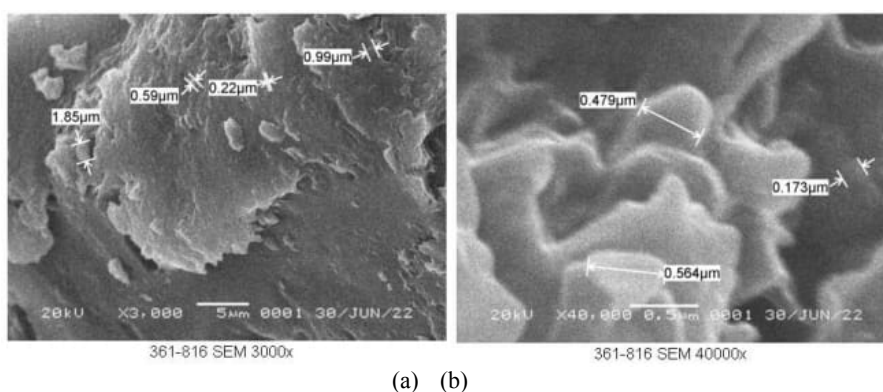


Figure 2. SEM characterization results of GNMW at a magnification of 3,000x (a) and 40,000x (b)

and other organoleptic parameters). A specific amount (100 mL) of GNMW suspension was freeze-dried for 48 hours. GNMW powder was obtained for 0.4108 g. GNMW powder was pale yellow with a characteristic odor. GNMW powder was soluble in water, very slightly soluble in propylene glycol, and practically insoluble in ethanol.

7. Gel preparation

Gel preparation was conducted by developing Carbopol 940 g with 20 times of water at a temperature of 70 °C then allowed to stand for 30 minutes so that Carbopol 40 powder could absorb water and expand optimally. TEA is one of the neutralizing agents that will ionize Carbopol and will create a negative charge on the polymer, resulting in a repulsion force that will cause the

formation of an extended three-dimensional structure that looks like a honeycomb formation in the gelling process, so that the gel will have a stable consistency and an increase in viscosity (37). Phenoxyethanol has antimicrobial activity. The concentration of phenoxyethanol that can be used in topical preparations is 0.5% - 0.1% (37). Propylene glycol was used as a humectant that would maintain the water content in the gel preparation so that the gel had good stability. In addition, propylene glycol could increase solubility, so that the active substance would dissolve and penetrate easily into the skin. The maximum concentration of propylene glycol that can be used in topical preparations as a humectant is 15% (38). Sodium metabisulfite was used as an external antioxidant to prevent oxidation in gel preparations. As stated in Maia et al., sodium

Table 3. pH, viscosity, and spread-ability value of GNMW gels

Evaluation parameters	F0	F1	F2	F3	Standard value
pH	7.23 ± 0.03	7.08 ± 0.12	6.96 ± 0.11	6.68 ± 0.07	6.0 – 8.0
Viscosity (cP)	14,673 ± 8.27	15,427 ± 189.03	16,720 ± 131.15	17,073 ± 94.52	3,000 – 50,000
Spread ability (cm)	6.4 ± 0.1	5.8 ± 0.1	5.62 ± 0.08	5.47 ± 0.15	5 – 7

metabisulfite was used as an antioxidant for vitamin C because it possesses limited stability as an antioxidant agent. To assess the vitamin C chemical stability in semisolid cosmetic formulations, several aspects must be regarded like exclusion of the oxygen, protection against the light and temperature, and the utilization of an efficient antioxidant system (39). GNMW gel containing MW extract which is supposed to have antioxidant activity like vitamin C as a positive control, also requires external antioxidants to provide optimal antioxidant activity to the gel preparations. The concentration of sodium metabisulfite that can be used as an antioxidant in pharmaceutical preparations is 0.01%-1% (38).

8. Evaluation of GNMW gel

GNMW gel produced was clear. There was no difference in the results of the organoleptic test on F0, F1, F2, and F3. GNMW gels had a neutral pH of 6,7 - 7,3 so they were safe for use on the skin. The homogeneity test on all gel formulations showed homogeneous results, indicated by the absence of lumps or coarse granules in the preparation. The results obtained met the requirements of the gel homogeneity test. The homogeneity test is related to the therapeutic effectiveness of the preparation. If the preparation is homogeneous, it is ensured that the concentration of the active substance is uniform, so that it will be evenly dispersed on the skin. The viscosity of GNMW gels was 14,580 – 17,180 cP. The value of viscosity increases with the increase in the concentration of the active substance. This is because MW extract contains 21.03% of pectin compound which can be used as a gelling agent (40) and in the process of making watermelon mesocarp extract nanoparticles using gelatin which functions as a thickening agent. The viscosity met the requirements, which are in the range of 3,000 – 50,000 (41). The spread-ability of all gel formulations was in the range of 5.3 – 6.5 and met a good spread-ability standard value. The value of pH, viscosity and spread-ability are shown in Table 3.

9. Irritation test

The irritation test was performed by applying the preparations on the upper forearm of the volunteers. The

skin of the upper forearm was chosen because the area has a thin and sensitive horn layer, so the absorption of the sample is quite large. There is a minimal movement in that area, so the attached sample can be in contact with the skin for a long time. The irritation test was carried out by the patch tester method to protect the sample from external influences (42). Based on the results of the GNMW gels irritation test, there was no irritant reaction in all volunteers.

10. Skin moisture test

Skin moisture is a condition that is influenced by the water and oil levels in the skin. If the moisture content is insufficient, it can cause dry skin or xerosis cutis. The water content in the stratum corneum in normal skin is about 10% in the outer layer and about 30% in the deeper layer. A decrease in the water content in the stratum corneum to less than 10% can cause the skin to become scaly, rough, and dry. Normal skin has a moisture content of 30-50% (43).

The results of the moisture test showed that GNMW gel with various concentration of 0% (F0), 0.0114% (F1), 0.0228% (F2), and 0.0342% (F3) could increase skin moisture after 3 hours of use. The moisture content of the panelists dull skin (without applying GNMW gel preparation) had an average value of 26.770% - 32.720%. After the application of GNMW gel preparations of F0, F1, F2, and F3 the moisture content increased from 38.810% - 63.190% (Figure 3.). The increase in skin moisture occurs due to the increased concentration of GNMW added to each formula. Okzelia & Mardiyah showed that the higher the concentration of MW extract added to the gel preparation, the higher the percentage of skin moisture (44). GNMW also played a role as an antioxidant to prevent the skin from drying out due to UV exposure. MW extract had compounds in the form of citrulline and flavonoids as natural antioxidants. With this ability, MW extract can prevent skin cells from being damaged, including skin dryness so that the skin was kept moist.

11. Antioxidant activity assay

The principle of measuring antioxidant activity with the DPPH method is that there is a change in the intensity

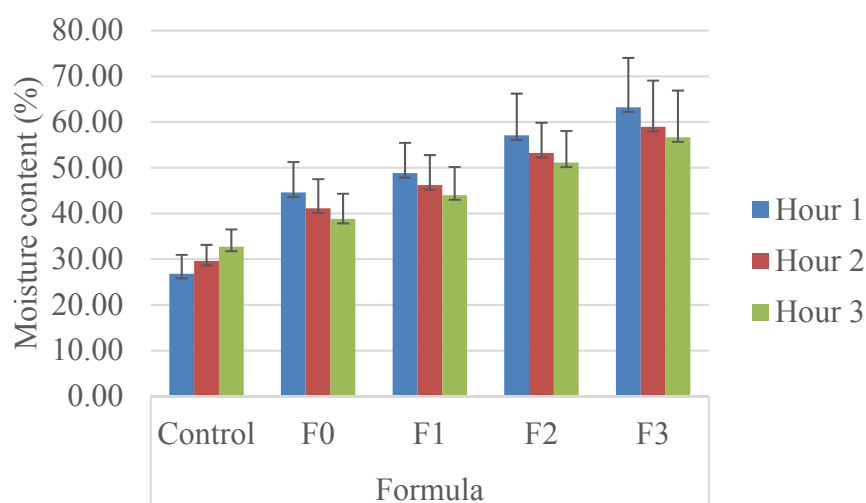


Figure 3. Profile of moisture content of GNMW gels toward volunteers skin

Table 4. Antioxidant activity test result using the DPPH method

Sample	IC ₅₀ value (µg/mL) ± SD
Vitamin C	7,89 ± 0,22
MW extract	110,90 ± 1,74
GNMW	114,16 ± 2,15
GNMW gels:	
F0 (basis)	161,62 ± 0,88
F1	149,52 ± 0,93
F2	138,44 ± 3,89
F3	127,10 ± 0,94

of the purple color from DPPH to pale purple to yellow. This happens because there is a reaction of the DPPH molecule with the hydrogen atom given by the compound molecule in the sample so that it is reduced to DPPH-H which forms the compound 2,2-diphenyl-1-picrylhydrazyl (45). The maximum wavelength of DPPH was scanned using a UV-Vis spectrophotometer. The results showed that the maximum wavelength of 100 ppm DPPH solution was 517.1417 with an absorbance of 0.757. The decrease in DPPH absorbance was measured against the control absorbance (DPPH in ethanol in a ratio of 1:3, without adding a sample). Qualitative analysis of the decrease in absorbance was indicated by a change in the color of the DPPH solution from pale purple to yellow. The intensity of the color of the solution is directly proportional to the increase in the concentration of the sample. A compound is categorized to have very active antioxidant activity if the IC₅₀ value is < 50 µg/mL, active is 50-100 µg/mL, moderate is 101-250 µg/mL, weak is 250-500 µg/mL, and inactive is >500 µg/mL (46). The result of the antioxidant activity assay of MW, GNMW, and GNMW gel preparations and vitamin C is shown in Table 4.

Vitamin C as positive control had a very active

antioxidant activity because it can donate hydrogen atoms and form relatively stable ascorbyl free radicals. MW extract had moderate antioxidant activity because it contained flavonoid compounds that function as antioxidants. In flavonoid compounds, there are free hydroxyl groups that have an activity to capture radicals and function to ward off new free radicals by breaking the chain reaction and turning them into more stable compounds. The increase in the IC₅₀ level indicated a decrease in the antioxidant activity of GNMW and GNMW gels, which could be due to the mixing the active substance in the form of an extract containing antioxidants with other additives in the produced nanoparticle. In addition, the results showed that as the concentration of antioxidant gel increased, IC₅₀ values decreased, indicating a significant effect of increasing concentration on antioxidant activity (p<0.05). The comparison of antioxidant activity is shown in Figure 4.

Conclusion

Antioxidant moisturizing gels had been formulated using GNMW extract in various concentration of 0.0114% (F1), 0.0228% (F2), and 0.0342% (F3) which met evaluation parameters criteria such as pH, viscosity,

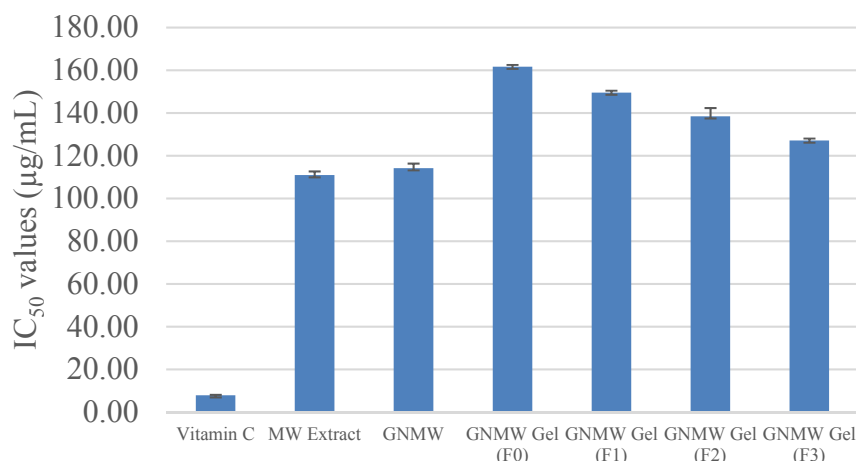


Figure 4. Comparative profile of IC₅₀ value of vitamin C, MW extract, GNMW, and GNMW gels

spread-ability, did not irritate the skin, had an IC₅₀ value in the range of $127,10 \pm 0,94 - 149,52 \pm 0,93$ µg/mL and could increase 38,81% - 63,19% skin moisture content.

The antioxidant activity of developed GNMW moisturizing gel in this study categorized as medium. The concentration of GNMW extract could be further increased to obtain antioxidant activity with a strong or very strong category.

Acknowledgment

All authors would like to thank the Indonesian Ministry of Research, Technology and Higher Education and Sekolah Tinggi Ilmu Kesehatan Bani Saleh's Research and Community Service Institute (Research Grant Contract No. 008/LIT-LPPM/STIKES-BS/VI/2022) for financial supports of this work.

References

- Oseni OA, Okoye VI. Studies of Phytochemical and Antioxidant Properties of The Fruit of Watermelon (*Citrullus lanatus*). (Thunb.). *J Pharm Biomed Sci.* 2013; 27(27):508–514.
- Amin A, Riski R, Sutamanggala NR. Antioxidant Activity of Mesocarp Extract of Watermelon (*Citrullus lanatus* (Thunb) Matsun & Nakai) Using ABTS Method. *J Pharma Med Sci.* 2021; 6(1):1–5.
- Fujiastuti T, Sugihartini N. Sifat Fisik dan Daya Iritasi Gel Ekstrak Etanol Herba Pegagan (*Centella asiatica* L.) dengan Variasi Jenis Gelling Agent. *J Farm Indones.* 2015;12(1):11-20.
- Shafiei M, Balhoff M, Hayman NW. Chemical and Microstructural Controls on Viscoplasticity in Carbopol Hydrogel. *J Polymer.* 2018; 139:44-51.
- Mahmoudi R, Ardakani MT, Verdom BH, Bagheri A, Mohammad-Beigi H, Aliakbari F, et al. Chitosan nanoparticles containing *Physalis alkekengi*-l extract: Preparation, optimization and their antioxidant activity. *Bull Mater Sci.* 2019;42(131):1–6.
- Yasmin R, Shah M, Khan SA, Ali R. Gelatin Nanoparticles: A Potential Candidate For Medical Applications. *Nanotechnol Rev.* 2017;6(2):191–207.
- Nejad H, Rabiee M, Varshochian R, Tahriri M, Jazayeri HE, Rajadas J, et al. Preparation and Characterization of Cardamom Extract-Loaded Gelatin Nanoparticles as Effective Targeted Drug Delivery System to Treat Glioblastoma. *J React Funct Polym.* 2017; 120:46-56.
- Okzelia SD, Hendrati D, Iljas N. Isolasi dan Pemisahan Senyawa Alkaloid dari Buah Mahkota Dewa (*Phaleria macrocarpa* Boerl.) dengan Metode Kromatografi Cair. *J Nursing Health.* 2017; 1(2):1–7.
- Marjoni MR. Modul Praktikum Fitokimia. Bitread Publishing. Bandung; 2019.
- Coester CJ, Langer K, Briesen H von, Kreuter J. Gelatin nanoparticles by two-step desolvation - a new preparation method, surface modifications and cell uptake. *J Microencapsul.* 2000; 17(2):187–193.
- Kharia AA, Singhai AK. Effective parameters for formulation of gastro adhesive nanoparticles: Screening by design-of-experiments approach. *J Microencapsul.* 2014; 31(4):399-405.
- Suryani, Wahyuni, Ariastika D, Rahmanpiu. Formulasi Nanopartikel Kurkumin dengan Teknik Gelasi Ionik Menggunakan Kitosan, Tripolifosfat dan Natrium Alginat serta Uji Stabilitasnya Secara In Vitro. *J Farm Sains Kesehat.* 2016; 2(1):17–21.
- Rahmawati DA, Setiawan I. The Formulation and Physical Stability Test of Gel Fruit Strawberry Extract (*Fragaria x ananassa* Duch.). *J Nutraceutical Herb Med.* 2019; 2(1):1–7.
- Ali A, Akhtar N, Mumtaz AM, Khan MS, Iqbal FM, Zaidi SS. In vivo skin irritation potential of a cream containing *Moringa oleifera* leaf extract. *Afr J Pharm Pharmacol.* 2013; 7(6):289–293.
- Lestari U, Syamsurizal, Farid F. Irritation Test and Effectiveness of The Clean Power Activated Charcoal Palm Shells (*Elaeis guineensis* Jacq) as Adsorbent Dirt on The Hair. *Indo J Pharm Res.* 2021; 1(1):13–18.

16. Leelapornpisid P, Mungmai L, Sirithunyalug B, Jiranusornkul S, Peerapornpisal Y. A novel moisturizer extracted from freshwater macroalga [*rhizoclonium hieroglyphicum* (C. agardh) k tzing] for skin care cosmetic. *Chiang Mai J Sci.* 2014;41(5–2):1195–1207.
17. Keng PS, Basri M, Zakaria MRS, Rahman MBA, Ariff AB, Rahman RNZA, et al. Newly synthesized palm esters for cosmetics industry. *Ind Crops Prod.* 2009;29(1):37–44.
18. Hidayat AF, Aryani R, Hannisah I. Preparation of Moisturizing Lotion Containing Silkworm (*Bombyx mori* L.) Sericin Nanoparticles. *Indonesian J Pharma Sci Technol.* 2022;9(1):1.
19. Rizkiah S, Okzelia SD, Efendi SA. Formulasi dan Evaluasi Gel dari Ekstrak Kulit Putih Semangka (*Citrullus Lanatus* [Thunb.] Matsum. & Nakai) Sebagai Pelembap Kulit. *J Sabdariffarma.* 2021;9(2):33–46.
20. Najib A. Ekstraksi Senyawa Bahan Alam. Yogyakarta: Deepublish. Yogyakarta; 2018.
21. Syarmalina, Wirawan D, Rahmat D. Formulasi Nanopartikel Ekstrak Temu Lawak Berbasis Kitosan Sebagai Antijerawat Nanoparticles Formulation of Temulawak Extract Based on Chitosan As Antiacne. *Med Sains.* 2019;3(2):153–158.
22. Kementerian Kesehatan RI. Farmakope Indonesia. Edisi VI. Jakarta: Kementerian Kesehatan RI. Jakarta; 2020.
23. Farrugia CA, Groves MJ. Gelatin Behaviour in Dilute Aqueous Solution: Designing a Nanoparticulate Formulation. *J Pharm Pharmacol.* 2010;51(6):643–649.
24. Shamarekh KS, Gad HA, Soliman ME, Sammour OA. Towards the Production of Monodisperse Gelatin Nanoparticles by Modified One Step Desolvation Technique. *J Pharm Investig.* 2020;50(2):189–200.
25. Etoriki AM, Gao M, Sadeghi R, Maldonado-Mejia LF, Kokini JL. Effects of Desolvating Agent Types, Ratios, and Temperature on Size and Nanostructure of Nanoparticles from α -Lactalbumin and Ovalbumin. *J Food Sci.* 2016;00(0):1–10.
26. Dai H, Li Y, Ma L, Yu Y, Zhu H, Wang H, et al. Fabrication of Cross-Linked β -Lactoglobulin Nanoparticles as Effective Stabilizers for Pickering High Internal Phase Emulsions. *Food Hydrocoll.* 2020;109:1–34.
27. Hong S, Choi DW, Kim HN, Park CG, Lee W, Park HH. Protein-Based Nanoparticles as Drug Delivery Systems. *Pharmaceutics.* 2020;12(604):1–28.
28. Syafrijal S, Sumarto S, Dewita D. Karakterisasi Mutu Nanopartikel Kolagen Daging Teripang Pasir (*Holothuria scabra*) Dengan Lama Waktu Pengadukan Berbeda. *Berkala Perikanan Terubuk.* 2018;46(1):1–10.
29. Zhang C, Chung JW, Priestley RD. Dialysis nanoprecipitation of polystyrene nanoparticles. *Macromol Rapid Commun.* 2012 Oct 26;33(20):1798–1803.
30. Sabdoningrum EK, Hidanah S, Chusniati S, Soeharsono. Characterization and Phytochemical Screening of Meniran (*Phyllanthus niruri* Linn) Extract's Nanoparticles Used Ball Mill Method. *Pharmacogn J.* 2021;13(6):1568–1572.
31. Danaei M, Dehghankhold M, Ataie S, Davarani FH, Javanmard R, Dokhani A, et al. Impact of Particle Size and Polydispersity Index on the Clinical Applications of Lipid Nanocarrier System. *Pharmaceutics.* 2018;10(2):57–73.
32. Ealia SAM, Saravanakumar MP. A review on the classification, characterisation, synthesis of nanoparticles and their application. In: *IOP Conf Series: Materials Science and Engineering.* 2017;263(3):1–16.
33. Rahmat D, Salim S. Uji Mukoadhesif Nanopartikel Crude Bromelin dari Perasan Bonggol Nanas Berbasis Hidroksi Propil Selulosa-Sisteamin. *Majalah Farmasetika.* 2019;4(1):113–118.
34. Honary S, Zahir F. Effect of Zeta Potential on the Properties of Nano-Drug Delivery Systems - A Review (Part 1). *Trop J Pharm Res.* 2013;12(2):55–64.
35. Lin J, Pan D, Sun Y, Ou C, Wang Y, Cao J. The Modification of Gelatin Films: Based on Various Cross-linking Mechanism of Glutaraldehyde at Acidic and Alkaline Conditions. *Food Sci Nutr.* 2019;7(12):1–7.
36. Lee WH, Booth JR, Bon SAF. On Particle Size Distributions in Catalytic Chain Transfer Emulsion Polymerization: Chain-Extension and the Use of Derived Macromonomers as Reactive Surfactants in Emulsion Polymerization. *Biomacromolecules.* 2020;21(11):4599–4614.
37. Daood NM, Jassim ZE, Gareeb MM, Zeki H. Studying the Effect of Different Gelling Agent on the Preparation and Characterization of Metronidazole as Topical Emulgel. *Asian J Pharm Clin Res.* 2019;12(3):571–577.
38. Rowe RC, Sheskey PJ, Quinn ME. *Handbook of Pharmaceutical Excipients.* Sixth Edit. USA: The Pharmaceutical Press. USA; 2009.
39. Maia AM, Baby AR, Pinto CASO, Yasaka WJ, Suenaga E, Kaneko TM, et al. Influence of Sodium Metabisulfite and Glutathione on the Stability of Vitamin C in O/W Emulsion and Extemporaneous Aqueous Gel. *Int J Pharm.* 2006;322:130–135.
40. Siskawardani DD, Kartika RA, Warkoyo, Khotimah K. The Study of Watermelon Rind (*Citrullus lanatus*) and Pineapple Fruit (*Ananas comosus* L.) Proportions with Caraganan Addition on Fruit Leather Physicochemical Characteristics. *Food Techno Halal Sci J.* 2018;1(1):71–80.
41. Elmitra. *Dasar-dasar Farmasetika dan Sediaan Semi Solid.* 1st Edition. Deepublish. Yogyakarta; 2017.
42. More BH, Sakharwade SN, Tembhurne SV, Sakarkar DM. Evaluation for Skin Irritancy Testing of Developed Formulations Containing Extract of *Butea monosperma* for Its Topical Application. *Int J Toxicol Appl Pharmacol.* 2013;3(1):10–13.
43. Rohmani S, Ningrum SK, Wardhani WD, Kundarto W. Pengaruh Variasi Konsentrasi Surfaktan Iselux Ultra Mild pada Formulasi Hydrating Facial Wash Potassium Azeloyl Diglycinate. *J Kefarmasian Indonesia.* 2022;12(1):58–68.
44. Okzelia SD, Mardiyah W. Formulasi dan Evaluasi Gel Pelembap Ekstrak Mesokarp Semangka [*Citrullus lanatus* (Thunb.) Matsum. & Nakai] sebagai Antioksidan. *J Pharma Health Res.* 2023;4(1):30–39.
45. Okzelia SD, Nurdaini M. Antioxidant Activity of Pidada (*Sonneratia caseolaris* (L.) Engl.) Fruit Extract by DPPH Method. In: *Singapore International Multidisciplinary Academic Conference (SIMAC).* Singapore; 2019. p. 1–8. <https://www.researchgate.net/publication/338764485>.
46. Marjoni MR, Zulfisa A. Antioxidant Activity of Methanol Extract/Fractions of Senggani Leaves (*Melastoma candidum* D. Don). *Pharm Anal Acta.* 2017;08(08):1–6.

Anticancer Effect and Safety Profile of a 4-Pyridyl Linked Triazolotriazine Derivative against Colorectal Tumor

R. Monfared¹, S. Farzipour^{2,3}, S. Dadashpour¹, Z. Zakeri Khatir¹, S. J. Hosseinimehr^{3*}, F. Talebpour Amiri⁴, H. Irannejad^{1†}

¹ Department of Medicinal Chemistry, Faculty of Pharmacy, Mazandaran University of Medical Sciences, Sari, Islamic Republic of Iran

² Cardiovascular Diseases Research Center, Department of Cardiology, Heshmat Hospital, School of Medicine, Guilan University of Medical Sciences, Rasht, Islamic Republic of Iran

³ Department of Radiopharmacy, Faculty of Pharmacy, Mazandaran University of Medical Sciences, Sari, Islamic Republic of Iran

⁴ Department of Anatomy, Faculty of Medicine, Molecular and Cell Biology Research

Received: 2 October 2023 / Revised: 5 November 2023 / Accepted: 28 November 2023

Abstract

Cancer is the second leading cause of global death, and colorectal cancer is the fourth most common cancer worldwide. In this study, the anticancer effect and safety profile of a 3-(pyridyl-4-l-methylthio) triazolotriazine derivative (**10b**) was investigated. The anti-tumor activity of **10b** was evaluated on HT-29 human colon cancer cell. To confirm the *in vivo* anti-cancer effect of **10b**, human colon tumor xenograft mice was used. Tumor bearing mice were treated with **10b** and paclitaxel for 10 days, then were sacrificed and their heart, liver and tumor tissues were isolated for pathological evaluation. Mice weight and tumor size were measured daily, and mortality was recorded. The results of cellular experiments showed that IC₅₀ of paclitaxel and **10b** was 0.34 and 8.92 μ M after 72 hours, respectively. The results of measuring the weight of mice and tumor size didn't show any significant changes in the **10b** treated groups. Pathological examinations indicated that the extent of hepatotoxicity and cardiac toxicity in mice receiving **10b** was lower than that of the paclitaxel group. Interestingly and hopefully, all mice treated with **10b** remained alive during the experiment but 50% of mice treated with paclitaxel and also 50% of mice in the control group were died. Totally, **10b** showed acceptable *in vitro* anti-tumor activity on HT-29 colorectal cells and no mortality in this group confirms the safety profile of **10b**.

Keywords: Colorectal cancer; Triazolotriazine; Tumor; HT-29; Xenograft.

Introduction

Cancer is the second leading cause of death in the world (1). In 2020, almost 19.3 million new cancer cases and almost 10.0 million cancer deaths occurred Worldwide (2). Cancer is a general term used for a range of dangerous diseases; which may affect different parts of the body. The disease is characterized by a

rapid and uncontrolled formation of abnormal cells. The abnormal cells may cause a tumor or gland to form an abnormal mass in other parts of the body. If this process is not stopped, the complication may progress to the point where it causes the death of an organ (3).

The main treatments for cancer are often surgery, radiotherapy and chemotherapy. Pharmacological agents often provide temporary relief from symptoms,

* Corresponding author: Tel: 09113210663; Email: sjhosseinim@yahoo.com, sjhosseinim@mazums.ac.ir

† Corresponding author: Tel: 09124572673; Email: irannejadhamid@gmail.com

longevity, and sometimes complete recovery. In recent years, a large number of anti-cancer drugs have been identified and developed; But they have many side effects. Therefore, it is necessary to try to find anti-cancer agents with better safety profile and reduced toxicity (4).

Colorectal cancer (CRC) is a heterogeneous disorder with disease-related overlapping subgroups, which may be recognized in primary tumors, primary cultures, xenografts, and traditional cell lines. This disease, also known as bowel, colon, or rectal cancer, ranks among the most common solid tumors worldwide. Most colorectal cancers are caused by aging and lifestyle factors, with only a few cases caused by underlying genetic disorders. Cancer-related mortality is strongly influenced by the high potential of metastasis and drug resistance (5, 6).

Studies on the regulation of signal transduction pathways in normal and malignant cells have provided important information on the mechanisms of oncogenesis and tumor progression. Today, more than 75 types of human tyrosine kinase (RTK) receptors are known, and many of them are involved in oncogenesis. Some types of tyrosine kinase receptors are proto-oncogenes that are involved in all main tumor growth and metastasis events, such as changes in reactive oxygen species, activation of downstream signal transduction molecules, cell proliferation, migration, and survival. Tyrosine kinase receptors are key molecular targets for designing anticancer drugs (7–10).

One of the most important types of these receptors is hepatic growth factor receptor (HGFR), also known as receptor tyrosine kinase c-Met which mediates a diverse set of normal physiological process such as morphogenesis, angiogenesis, proliferation, survival and apoptosis. Aberrant or amplification of HGF/c-Met signaling pathway has been associated with metastatic progression, invasion and developing resistance against the conventional therapies. Therefore, inhibition of this target is a promising strategy in a group of anticancer drugs (11).

Recently, in a research on the design and synthesis of specific c-Met kinase inhibitors, we found compounds with the core structure of triazolotriazine, which showed promising in vitro anti-cancer effect on some tumor cell lines and nanomolar IC_{50} values for the inhibition of the c-Met enzyme (12). Of the several dozen compounds studied, compound 10b was more effective than its congeners with IC_{50} values of 0.74 and 1.14 μ M on HepG2 and A-549 cell lines respectively and an IC_{50} of 4.6 nM towards the inhibition of the c-Met enzyme (Figure 1).

Considering the remarkable suppressive effects of

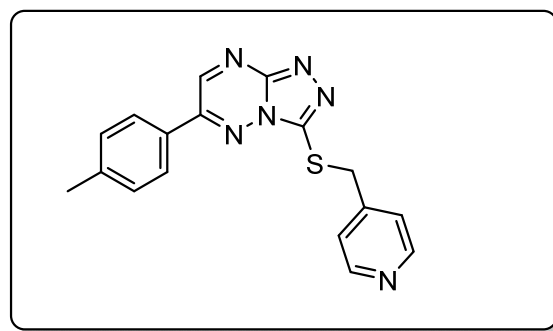


Figure 1. The structure of 3-((Pyridin-4-ylmethyl) thio)-6-(p-tolyl)- [1,2,4] triazolo[4,3-b] [1,2,4] triazine (10b) as a potent c-Met kinase inhibitor.

10b on the tumor cells previously reported; in the current study, we aimed at evaluating the in vitro and in vivo potential of 10b on the HT-29 tumor cells xenografted nude-mice compared to paclitaxel and investigating its organ and tissue toxicity as well as survival and mortality of the mice.

Materials and Methods

In this study, the HT-29 cell line (human colon cancer cells) was purchased from the Pasteur Institute and stored in liquid nitrogen. The cells were cultured in DMEM medium containing 10% fetal bovine serum (FBS), penicillin-streptomycin at 37°C in an atmosphere with 5% CO₂ concentration. Compound 10b was previously synthesized in our lab (12) and paclitaxel was prepared as an injectable liquid at a concentration of 6 mg/ml (Sobhan Pharmaceutical Company, Iran).

In vitro study

MTT assay was performed in order to compare the cytotoxic effect of 10b and paclitaxel on HT-29 colon cancer cells and to determine the IC_{50} values. This test was performed simultaneously on two 96-well plates, whereas 10,000 cells were added to each well in each 96-well plate. The 96-well plates containing the implanted cells were then incubated for 24 hours to allow the cells to reach their logarithmic growth stage. The new culture medium without drugs was added to rows 1 and 7 as control group. In rows 2 to 6, culture medium containing paclitaxel at concentrations of 0.01, 0.05, 0.1, 0.5 and 1 μ M, and in rows 8 to 12, culture medium containing 10b at concentrations of 0.5, 1, 5, 10 and 50 μ M were added. One plate was then incubated for 48 hours and the other plate for 72 hours to allow the cells to be in sufficient contact with the drugs. After incubation, the culture was removed and 20 μ l of MTT solution with fresh culture medium was added to each

well, and 96-well plates were placed in the incubator for 4 hours. After that, 100 μ l of DMSO solution was added to each well (to dissolve insoluble formazan). It was then mixed for 15 minutes to completely dissolve the formazan. The absorbance of each well was read with an ELISA Reader at 570 / 630 nm (Bioteck, USA). Cells without any treatment were used as control for comparison of absorbance and cell viability (13).

$$\% \text{ Viability} = \frac{\text{OD mean (Treated Well)}}{\text{OD mean (Control Well)}} \times 100$$

OD= optical density

Animal study

The experiments were approved by the Ethical Committee of Mazandaran University of Medical Sciences (ID#IR.MAZUMS.REC.1397.4831). In this study, 30 nude mice in the weight range of 18-22 g and in the age range of 6 to 8 weeks were purchased from Pasteur Amol Institute (IRAN). The mice were kept under standard conditions with sterile water and food. HT-29 tumor cells were injected intraperitoneal at a rate of 5×10^6 per mouse. The tumor was allowed to grow for 2 to 3 weeks, and when the tumor size reached 350-450 mm^3 , in vivo testing was started. Tumor size was calculated by the $(\text{length} \times \text{width}^2 \times 0.5)$ formula. All experiments were performed under a laminar hood and in an aseptic environment.

Mice were divided into three groups: control, paclitaxel and 10b (n= 10). The control group received solvent for ten days. The paclitaxel group received paclitaxel with a concentration of 5 mg/kg for five days and after two days of resting, the second injection was performed and continued to the end of the experiment. The 10b group received the synthesized 10b at a dose of 20 mg/kg at similar schedule injection to paclitaxel. Mice mortality, weight, and tumor size were measured daily.

Histopathological examinations

Tumor, heart and liver tissues were fixed in 10% formalin buffer. The fixed tissue was dehydrated in a series of stratified alcohols, clarified in xylene, and molded vertically in paraffin. Sections of 5 μ m-thick were prepared using rotating microtome, and used for histopathological evaluation. Semi-quantitative tissue damage for each slide were considered on a scale of 0 (normal), 1 (mild), 2 (low), 3 (moderate) and 4 (severe) (14).

Statistical analysis

All data were evaluated by Graphpad prism software (USA). All data were expressed as mean \pm standard deviation. $P < 0.05$ was accepted as a statistically

significant change.

Results

MTT assay

The percentage of cell survival against different concentrations of paclitaxel is shown in Figure 2. As illustrated in the Figure 2, the rate of cell mortality increases with higher concentrations of paclitaxel and also after passing 72 h of the drug treatment. The highest toxicity was observed in the group containing paclitaxel at the dose of 1000 nM after 72 hours and the lowest mortality rate belonged to the group receiving 10 nM after 48 hours. After 48 hours, the cytotoxic effect of paclitaxel in HT-29 cells was calculated as an IC_{50} value of $0.86 \pm 0.18 \mu\text{M}$ and after 72 hours it was $0.34 \pm 0.09 \mu\text{M}$.

The percentage of cell survival in different concentrations of 10b is shown in Figure 3. As represented, the cell mortality rate was the highest in the group containing 10b at a dose of 50 μM , and after 72 hours of the drug treatment. Among the groups receiving 10b, the lowest mortality rate belonged to the group receiving 0.5 μM dose after 48 hours. Accordingly, increasing the drug concentration increased the cytotoxicity of 10b. IC_{50} of the cytotoxic effect of 10b in HT-29 tumor cells was calculated and was shown to be $17.50 \pm 5.22 \mu\text{M}$ after 48 hours and $8.92 \pm 2.35 \mu\text{M}$ after 72 hours of the treatment.

Animal experiments

Body weight

The weight of mice in the three groups were recorded daily during the treatment period and the corresponding variation curves are represented in Figure 4. As illustrated, the weight of mice in control and 10b groups was associated with a slight increase until day 3 and after that remained relatively constant. Mice in the paclitaxel group lost weight in the fifth and sixth day of the treatment, although the difference in weight of mice between the three groups was not statistically significant.

Tumor size

According to the represented data in Figure 5, the size of tumors in the control and paclitaxel groups changed similarly during the treatment and totally was associated with a slight increase at the end of the treatment. In the case of 10b, the volume of tumors increased constantly during the study, although the difference in tumor size between the three groups was not statistically significant.

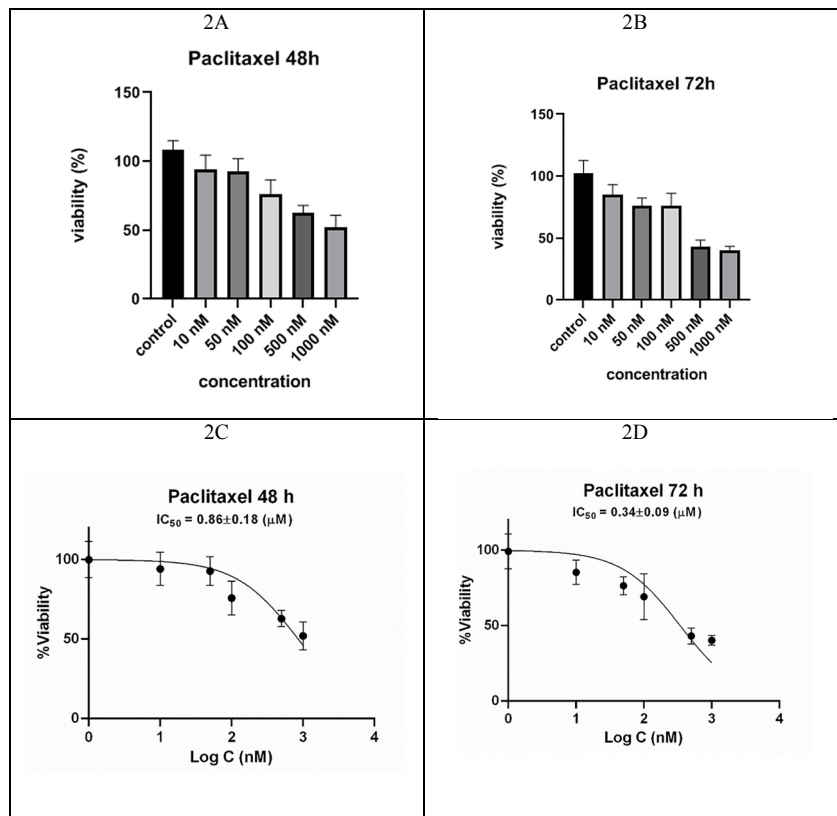


Figure 2. Cell viability percentage exposed to different doses of paclitaxel, A) after 48 and B) after 72 hours and the corresponding IC₅₀ value curves C and D.

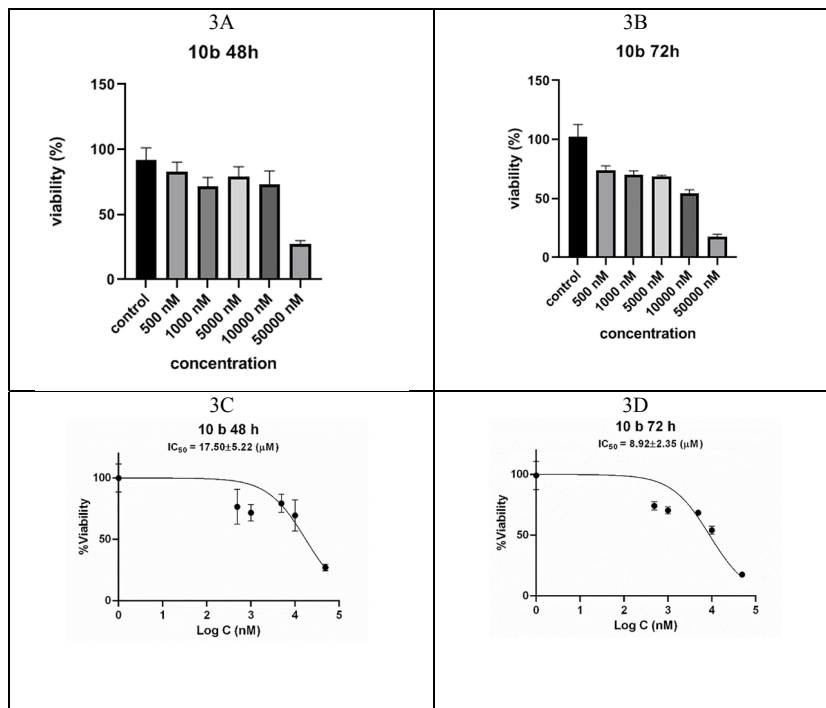


Figure 3. Cell viability percentage exposed to different doses of 10b, A) after 48 and B) after 72 hours. IC₅₀ curves of **10b** against HT-29 cell line after 48 (C) and 72 hours (D).

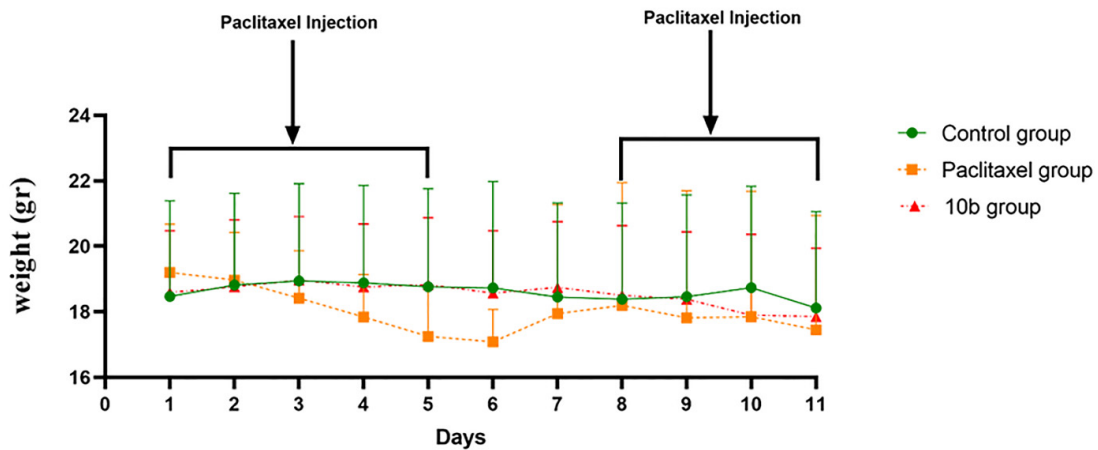


Figure 4. The results of measuring the weight of mice in different groups during the treatment period (Mean \pm SE).

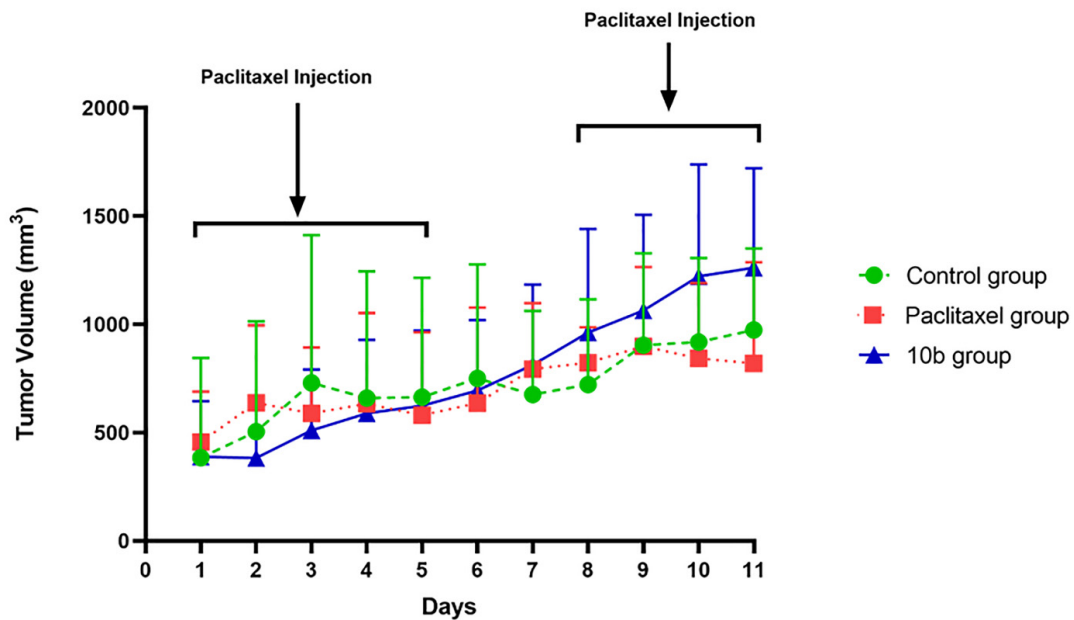


Figure 5. The results of measuring the size of the tumor in different groups studied and on different days (Mean \pm SE).

Mice survival analysis

As shown in Figure 6, in each of the paclitaxel and control groups, five mice died during the study. Interestingly, no mortality was observed in the group 10b. The survival rates of mice in control, paclitaxel and 10b groups were 50, 50 and 100%, respectively.

Tumor histopathology

Figure 7 shows the microphotography of the tumor mass in all groups. In the control group, the tissue structure of the tumor mass shows high mitotic division. Tissue necrosis is not seen except in the central part due to lack of nutrients reaching the cells. But in groups

paclitaxel and 10b, with high density nucleus of tumor cells and foamy vacuolated tumor cells are more common than in the control group. These changes are more evident in group paclitaxel than in group 10b. Quantitative evaluation showed that the rate of tumor tissue necrosis in the paclitaxel group increased significantly compared to the control group ($P < 0.001$). The rate of tumor tissue necrosis in group 10b was significantly increased compared to the control group ($P < 0.05$). In addition, the rate of tumor tissue necrosis was higher in the paclitaxel group than in the 10b group, but this increase was not statistically significant.

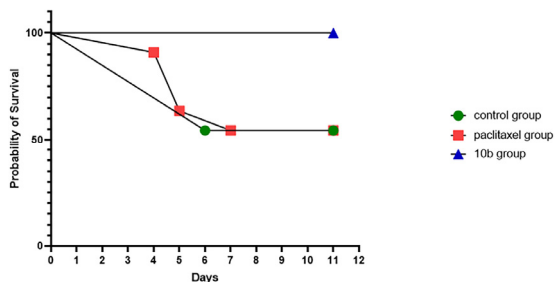


Figure 6. Mice mortality in the studied groups.

Liver pathology

Figure 8 shows the microphotography of the liver tissue in all groups. In the control group, the liver shows a normal structure (sinusoid, hepatocyte, kupffer cells). But in groups paclitaxel and 10b, hepatocyte necrosis, sinusoidal dilatation, proliferation of kupffer cells, congestion, and hemorrhage were seen. This injury was more severe in group paclitaxel than in group 10b. Quantitative evaluations showed that liver damage in the group receiving paclitaxel was significantly higher than in the control group ($P < 0.001$). Also, liver damage

in mice receiving compound 10b was significantly higher than in the control group ($P < 0.01$); But no statistically significant difference was observed between 10b and paclitaxel groups.

Cardiac pathology

Figure 9 shows the microphotography of the heart tissue in all groups. In the control group, the heart tissue shows a normal structure. But in groups paclitaxel and 10b, necrosis, infiltration of inflammatory cells, edema, eosinophilic myocytes and hemorrhage were seen. This injury was more severe in group paclitaxel than in group 10b. Quantitative evaluation showed that heart damage was significantly higher in both groups receiving paclitaxel and 10b compared to the control group ($P < 0.0001$). Also, heart damage was lower in mice receiving compound 10b compared to the paclitaxel group, but this reduction was not statistically significant.

Discussion

The 1,2,4-triazine ring is a widely used scaffold for many biologically active compounds, natural or synthetic, with a wide range of pharmacological effects.

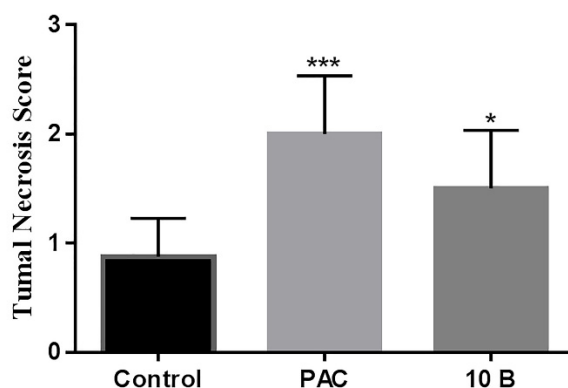
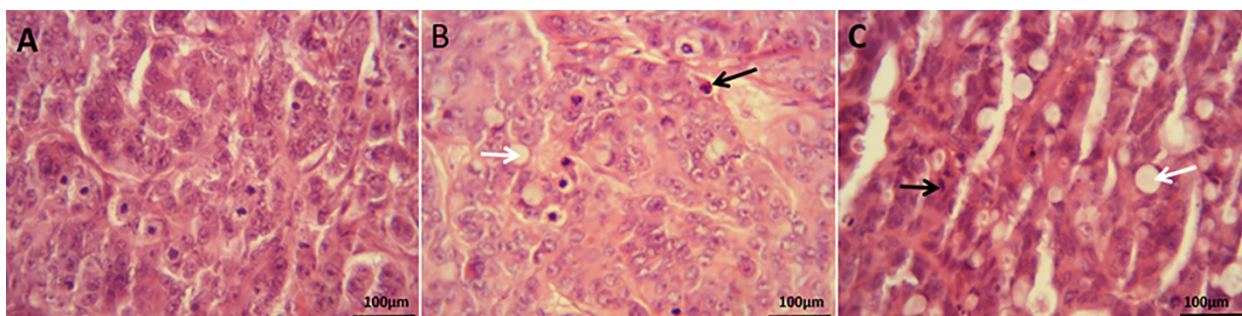


Figure 7. Results of tumor pathology in the studied groups. A) tissue sample from the control group. B) tissue sample from paclitaxel group and C) tissue sample from group 10b. Black arrow: with high density nucleus of tumor cells. White arrow: foamy vacuolated tumor cells. Hematoxylin and eosin staining. 20% magnification, load scale: 100 μm.

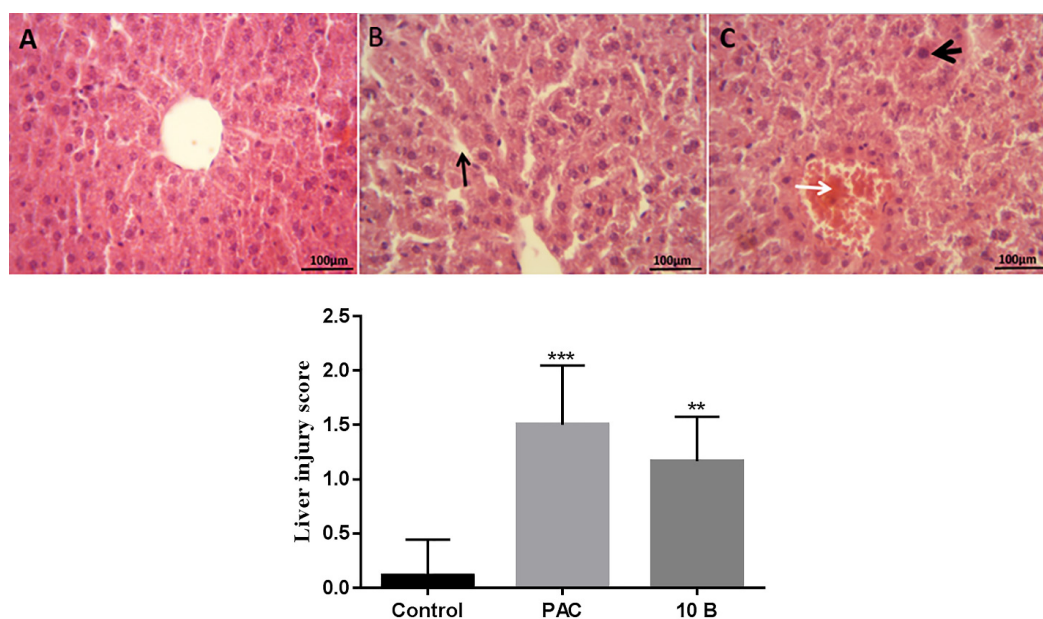


Figure 8. Results of liver tissue pathology. A) tissue sample from the control group. B) tissue sample from paclitaxel group and C) tissue sample from group 10b. Thin black arrow: Sinusoidal dilatation. Thick black arrow: Hepatocyte eosinophilia. White arrow: Lobular center venous congestion. Hematoxylin and eosin staining. 20% magnification, load scale: 100 μ m.

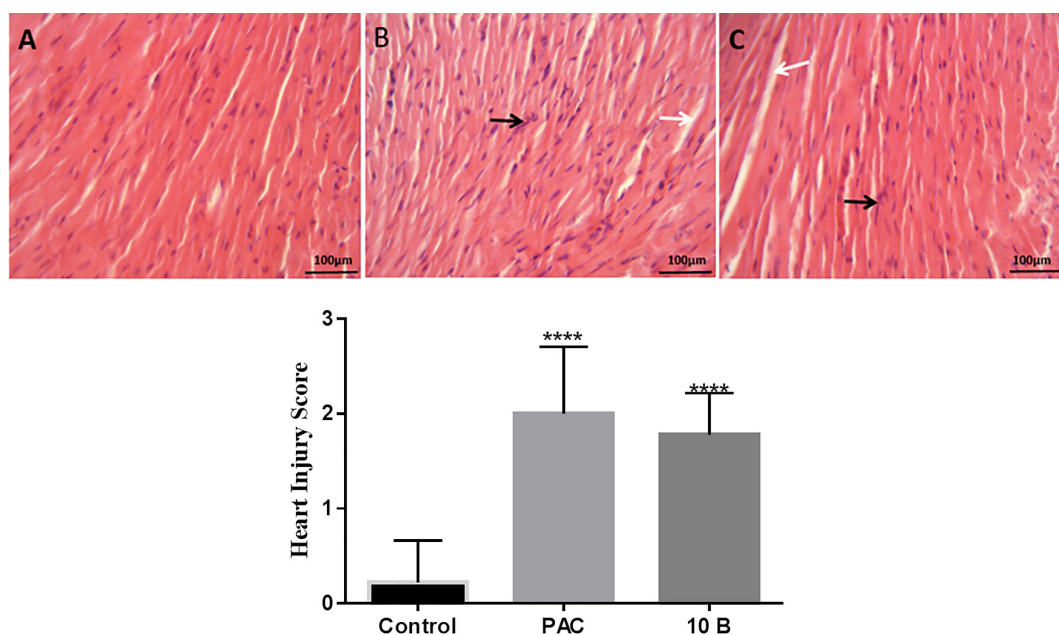


Figure 9. Results of heart tissue pathology. A) tissue sample from the control group. B) tissue sample from paclitaxel group and C) tissue sample from group 10b. Black arrow: Infiltration of inflammatory cells. White Arrow: Inflation. Hematoxylin and eosin staining. 20% magnification, load scale: 100 μ m

In particular, it is known as anti-tumor, anti-HIV, antimicrobial, anti-inflammatory, neuroprotective, anti-Alzheimer's. The NCNN sequence of 1,2,4-triazine ring is considered as an essential component for various pharmacological activities (15). The triazolotriazine

nucleus has been considered as a main interacting fragment in the design of the c-Met tyrosine kinase inhibitors because it has electron-deficiency due to the presence of the several nitrogen atoms. The electron-deficiency of the triazolotriazine nucleus makes it a

prominent motif to interact with the electron-rich Tyr1230 through a π - π stacking in the active site. This interaction infers affinity and selectivity to the c-Met inhibition (16). Accordingly, we investigated the *in vitro* and *in vivo* anti-cancer effect and cytotoxicity of our recently synthesized triazolotriazine derivative, 3-((Pyridin-4-ylmethyl)thio)-6-(p-tolyl)-[1,2,4]triazolo[4,3-b][1,2,4]triazine (10b) in HT-29 colon cells and tumor-induced nude mice.

The results of cellular MTT assay showed that increasing the dose of paclitaxel is associated with elevated cell mortality. In addition, the IC_{50} of paclitaxel was 0.86 and 0.34 μ M after 48 and 72 hours, respectively. Increasing the dose of compound 10b also increased cell mortality and the IC_{50} of this compound after 48 and 72 hours was 17.50 and 8.92 μ M, respectively. The results indicate that paclitaxel was more effective than 10b in inducing cell death. The potential of paclitaxel on increasing cancer cell mortality was 23 times greater than that of the 10b.

The results obtained from measuring the size of the tumors showed that there was no significant change in comparison between the control, paclitaxel and **10b** groups. This means that none of the two drugs were successful in inhibiting the growth of the colon tumor size in mice. Probably, this failure was due to the inappropriately chosen dosage regimens either in the drug concentration or the length of time for the drug consumption.

The results of measuring the weight of mice did not show any significant change between the three groups. This means that neither of the two compounds paclitaxel and **10b** had a significant effect on the mice weight.

Enlargement of the tumor led to necrosis of cells in the central part of the tumor mass. But in the tumor cells of the mice that received 10b and paclitaxel, vacuolation and nucleation of the nucleus were seen. Also, fibrous fibers in the structure of the tumor tissue in mice receiving 10b and paclitaxel were more than the control group. All of these tumor tissue alterations indicated that paclitaxel and 10b exhibited anti-tumor activity.

The histopathological examinations were performed for side effects induced by paclitaxel and 10b in normal tissues in mice. The tissue structure of the liver lobules in the control group was completely normal. Changes in the liver structure of mice receiving paclitaxel including lobular central venous congestion, Kupffer cell proliferation, sinusoidal dilatation, and eosinophilic hepatocytes were evident of the tissue damage. While, these changes were less severe in the group receiving **10b**. Cardiac muscle fibers in the control group had a normal structure. Infiltration of polymorphonuclear cells, activated fibroblasts, and edema were seen in the

heart structure of mice receiving paclitaxel. These changes were also seen in group 10b with less severity. According to the observations, the extent of hepatotoxicity and cardiac toxicity in mice receiving 10b was lower than that of the paclitaxel group.

Mortality rates were high in the control and paclitaxel treated mice as compared to 10b group. It is meant that tumor bearing mice died in the control and paclitaxel groups due to the enlargement of the tumor and its side effects, while the mortality rate was zero in 10b treated mice. It is cleared that 10b exhibited no significantly tumor growth inhibition whereas tumor histopathological findings and survival assessment were promising for 10b in this study.

Several studies have been reported considering the *in vivo* efficacy of some similar triazolotriazine derivatives on the xenograft tumor growth. Correspondingly, compound **1** (Figure 10) was identified as a highly potent compound with IC_{50} values of 0.24, 0.85, and 0.46 nM in the c-Met enzymatic activity, cellular activity in EBC-1 lung cell line, and MKN45 gastric cell line, respectively. *In vivo* usage of compound **1** at 25 mg/kg showed remarkable antitumor activity in c-Met-driven EBC-1 and MKN45 xenograft models with an inhibitory rate of 96.5%. Besides, oral administration of compound **1** at a 25 mg/kg dose led to complete tumor regression in the EBC-1 xenograft mouse model with minimal toxicity(16). Compound **2** is an exclusively selective c-Met inhibitor with IC_{50} of 0.006 μ M. This compound was tested for tumor growth inhibition (TGI) and its relationship to the inhibition of the c-Met autophosphorylation in a c-Met amplified GTL-16 xenograft tumor model. In efficacy studies for compound **2**, no weight loss was observed at any dose level. Tumor regression (-34% TGI) was seen with a dose of 100 mg/kg, and tumor stasis (100% TGI) was achieved at 30 mg/kg. Although compound **2** was a potent inhibitor of the c-Met receptor tyrosine kinase with high protein kinase selectivity, its broad phosphodiesterase family inhibition resulted in myocardial degeneration in rats, therefore it was terminated as a preclinical candidate(17). Compound **3** (SGX523) is extremely selective for c-Met with an IC_{50} of 4 nM and is orally bioavailable in all species tested, making it a useful tool for investigating the role of c-Met in animal models. Therefore, compound **3** was administrated to nude mice with established tumors to see whether this compound is sufficient to control the growth of xenografts derived from U87MG human glioblastoma cells and H441 human lung carcinoma cells. Administration of compound **3** at a dose of 30 mg/kg led to apparent tumor regression of U87MG. Additionally, the growth

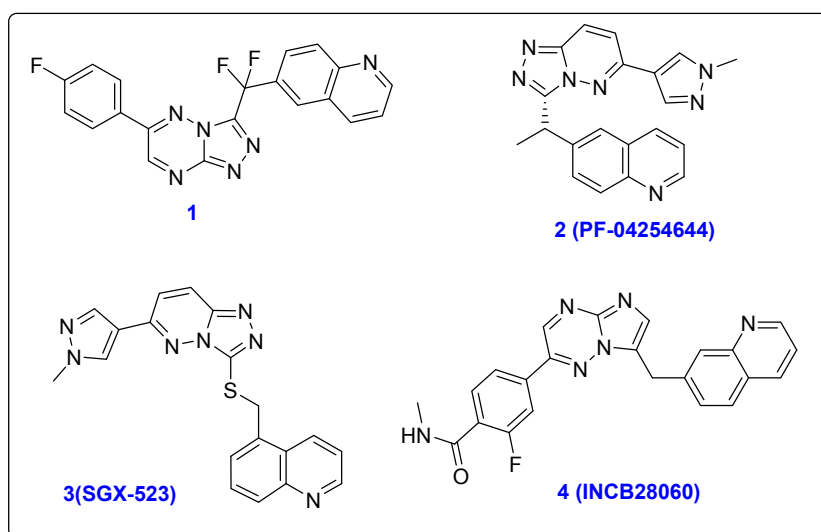


Figure 10. The representative selective c-Met inhibitors with antitumor activity.

of H441 tumors in mice treated with compound **3** at 30 mg/kg reduced tumor c-Met autophosphorylation levels. Unfortunately, a phase I clinical trial to assess the safety of SGX523 had to be stopped due to kidney toxicity(18). Compound **4** (INCB28060) is a new c-Met inhibitor with an IC_{50} of 0.13 nM in a cell-based assay and more than 10,000-fold selectivity against a broad panel of human kinases. The S114 cell-derived mouse tumor model (S114 cell line stably expresses human HGF and c-MET) was used to evaluate *in vivo* activities of compound **4**. Treatment with small molecule **4** at 0.3 mg/kg led to nearly 50% inhibition of c-Met phosphorylation. Oral administration of this compound inhibited c-Met phosphorylation and tumor growth in c-Met-driven mouse tumor models in a time- and dose-dependent manner, with no evidence of toxicity or weight loss(19).

Totally, the results of the previous studies indicate that toxicity evaluation of the drugs is an integral part of the lead optimization process and *in vivo* safety profile of a drug-like compound assures that the entire process will proceed almost with confidence.

Conclusion

In this study, we evaluated the potential of compound **10b** as an anti-cancer agent on HT-29 colon cells and HT-29 xenograft nude mice. *In vitro* assays showed that compound **10b** is an effective inhibitor for HT-29 cancer cell lines with IC_{50} = 8.92 μ M, compared to the standard drug paclitaxel (IC_{50} = 0.34 μ M). No apparent toxicity in weight loss and morbidity was observed with the administration of **10b** in mice, revealing acceptable safety. Happily, the extent of

hepatotoxicity and cardiac toxicity in mice receiving **10b** was lower than that of the paclitaxel group. These findings suggested that compound **10b** is unlikely to exert severe unfavorable effects in host organs and tissues at therapeutically relevant doses. Although, **10b** failed to considerably reduce tumor size, but its high survival potential in mice receiving **10b** and tumor histopathological findings were promising in this study.

Human and Animal Rights

All experiments were accomplished in accordance with the ethical standards and protocols approved by the Committee of Animal Experimentation of Mazandaran University of Medical Sciences, Sari, Iran (Ethics Code: IR.MAZUMS.REC.1397.4831).

Acknowledgment

This study was accomplished through grant number 4831 from the Mazandaran University of Medical Sciences, Sari, Iran.

Conflict of interest

Authors declare no conflict of interest.

References

1. Fitzmaurice C, Abate D, Abbasi N, Abbastabar H, Abd-Allah F, Abdel-Rahman O, et al. Global, Regional, and National Cancer Incidence, Mortality, Years of Life Lost, Years Lived With Disability, and Disability-Adjusted

- Life-Years for 29 Cancer Groups, 1990 to 2017: A Systematic Analysis for the Global Burden of Disease Study. *JAMA Oncol.* 2019 Dec;5(12):1749–68.
- Sung H, Ferlay J, Siegel RL, Laversanne M, Soerjomataram I, Jemal A, et al. Global cancer statistics 2020: GLOBOCAN estimates of incidence and mortality worldwide for 36 cancers in 185 countries. *CA Cancer J Clin.* 2021;71(3):209–49.
 - López-Lázaro M. The stem cell division theory of cancer. *Crit Rev Oncol Hematol.* 2018;123:95–113.
 - Noori-Dalooi MR, Ebadi N. Pharmacogenomics and cancer stem cells. *Med Sci J Islam Azad University-Tehran Med Branch.* 2015;25(1):1–15.
 - Buczacki SJA, Popova S, Biggs E, Koukorava C, Buzzelli J, Vermeulen L, et al. Itraconazole targets cell cycle heterogeneity in colorectal cancer. *J Exp Med.* 2018;215(7):1891–912.
 - Cesaro P, Raiteri E, Demoz M, Castino R, Baccino FM, Bonelli G, et al. Expression of protein kinase C β 1 confers resistance to TNF α -and paclitaxel-induced apoptosis in HT-29 colon carcinoma cells. *Int J cancer.* 2001;93(2):179–84.
 - Bottaro DP, Rubin JS, Faletto DL, Chan AM-L, Kmieciak TE, Vande Woude GF, et al. Identification of the hepatocyte growth factor receptor as the c-met proto-oncogene product. *Science* (80-). 1991;251(4995):802–4.
 - Cooper CS, Park M, Blair DG, Tainsky MA, Huebner K, Croce CM, et al. Molecular cloning of a new transforming gene from a chemically transformed human cell line. *Nature.* 1984;311(5981):29–33.
 - Gherardi E, Birchmeier W, Birchmeier C, Woude G Vande. Targeting MET in cancer: rationale and progress. *Nat Rev cancer.* 2012;12(2):89–103.
 - Takeuchi K, Ito F. Receptor tyrosine kinases and targeted cancer therapeutics. *Biol Pharm Bull.* 2011;34(12):1774–80.
 - Zhang Y, Xia M, Jin K, Wang S, Wei H, Fan C, et al. Function of the c-Met receptor tyrosine kinase in carcinogenesis and associated therapeutic opportunities. *Mol Cancer.* 2018;17(1):1–14.
 - Dadashpour S, Küçükılınç TT, Ayazgök B, Hosseinimehr SJ, Chippindale AM, Foroumadi A, et al. Discovery of novel 1,2,4-triazolo-1,2,4-triazines with thiomethylpyridine hinge binders as potent c-Met kinase inhibitors. *Future Med Chem [Internet].* 2019 May;11(10):1119–36. Available from: <https://www.future-science.com/doi/10.4155/fmc-2018-0412>
 - Rezaie-Tavirani M, Fayazfar S, Heydari-Keshel S, Rezaee MB, Zamanian-Azodi M, Rezaei-Tavirani M, et al. Effect of essential oil of *Rosa Damascena* on human colon cancer cell line SW742. *Gastroenterol Hepatol from bed to bench.* 2013;6(1):25.
 - Tomayko MM, Reynolds CP. Determination of subcutaneous tumor size in athymic (nude) mice. *Cancer Chemother Pharmacol.* 1989;24(3):148–54.
 - Khatir ZZ, Irannejad H. Pharmacologic Activities of 5, 6-Diaryl/heteroaryl-3-substituted-1, 2, 4-triazines as a Privileged Scaffold in Drug Development. *Mini Rev Med Chem.* 2021;21(19):2874–928.
 - Zhan Z, Peng X, Liu Q, Chen F, Ji Y, Yao S, et al. Discovery of 6-(difluoro (6-(4-fluorophenyl)-[1, 2, 4] triazolo [4, 3-b][1, 2, 4] triazin-3-yl) methyl) quinoline as a highly potent and selective c-Met inhibitor. *Eur J Med Chem.* 2016;116:239–51.
 - Cui JJ, Shen H, Tran-Dubé M, Nambu M, McTigue M, Grodsky N, et al. Lessons from (S)-6-(1-(6-(1-Methyl-1 H-pyrazol-4-yl)-[1, 2, 4] triazolo [4, 3-b] pyridazin-3-yl) ethyl) quinoline (PF-04254644), an Inhibitor of Receptor Tyrosine Kinase c-Met with High Protein Kinase Selectivity but Broad Phosphodiesterase Family Inhibit. *J Med Chem.* 2013;56(17):6651–65.
 - Buchanan SG, Hendle J, Lee PS, Smith CR, Bounaud P-Y, Jessen KA, et al. SGX523 is an exquisitely selective, ATP-competitive inhibitor of the MET receptor tyrosine kinase with antitumor activity in vivo An Exquisitely Selective Kinase Inhibitor. *Mol Cancer Ther.* 2009;8(12):3181–90.
 - Liu X, Wang Q, Yang G, Marando C, Koblisch HK, Hall LM, et al. A Novel Kinase Inhibitor, INCB28060, Blocks c-MET--Dependent Signaling, Neoplastic Activities, and Cross-Talk with EGFR and HER-3 INCB28060, a c-MET Kinase Selective Inhibitor. *Clin cancer Res.* 2011;17(22):7127–38.

Microstructures and Crystal Size Distribution (CSD) of Chromites from Gysian Silvana Ophiolite Serpentinites, Urmia, Iran

M. Modjarrad*

Faculty of Sciences, Department of Geology, Urmia University, Urmia, Islamic Republic of Iran

Received: 17 July 2022 / Revised: 11 June 2023 / Accepted: 22 June 2023

Abstract

One of the components of Gysian Silvana ophiolite in the south of Urmia and the continuation of the Neo-Tethys in the northwestern of Iran is serpentinites with lizardite/chrysotile and magnetite phases as the main mineral and chromite (Cr-spinel) and some rare olivine and orthopyroxenes. A variety of microstructures such as mesh, sieve, lamellar, fibrous, and hourglass were identified. The existence of lizardite plates (001) crosswise in the margin of a low crystallized mass nucleus of net texture is determined by microstructures. Due to the lack of antigorite in the serpentinites, the depth of subduction of the Neo-Tethys slab in this part of Iran may be low. The crystal size distribution (CSD) of the Gysian serpentinite chromites was studied. We discriminate three types of CSD patterns for chromite crystals, extract nucleation, and growth parameters from intercept and slope values of the patterns. The first type is a linear steady-state pattern with a nucleation rate/growth rate (J/G) of about 12 and $Gt=1.28$; the second type has a non-linear concave downtrend which is the result of annealing or Ostwald ripening at a small size part with $J/G=13-15$ and $Gt=1.33$. The third type is complex and shows nucleation density with two separate parts. It could be modeled by two crystal populations, small and large sizes overlapping linear patterns. The J/G for small crystals was twice for large sizes and multiple nuclei have less growth. The Gt was 1.60 for small and 1.10 for those large sizes. Assuming the constant crystal growth rate in silicate materials is 10^{-9} cm/s, the time for the growth of large chromites is six times longer than that of small crystals. These two segmental CSD patterns probably present arising processes or alteration production of mafic minerals as small chromites.

Keywords: Chromite; CSD; Gysian; Urmia; Iran.

Introduction

According to the manner and style of placement, ophiolites are divided into the following two categories (1, 2): active marginal ophiolites, in which ophiolite spots

are found in ruptures inside, and active continental margins, and often they have a melange form and, secondly, the ophiolites of the collision zones are found at the collision of the plates. Serpentinization is one of the most common alteration processes in ophiolites

* Corresponding author: Tel: +98 9143450452; Email: m.modjarrad@urmia.ac.ir

through which chemical reactions of water with peridotites produce serpentine group minerals including chrysotile, lizardite, and antigorite (3, 4). According to some researchers, studying how serpentinites is formed could have critical applications for understanding the large-scale geodynamics of that area (5, 6). Serpentinization occurs in a vast range of pressures and temperatures. A principal story of subduction zones is the return (recirculation) of hydrated rocks into the mantle and the so-called "subduction factory" (7). The progression of serpentinization causes a decrease in the seismic velocity of rocks (8).

The texture of rocks and parameters such as size offers important evidence about the petro-physical procedures complicated in rock formation (9-12). The CSD analysis eventually improves our knowledge of magmatic progressions. Therefore, the crystal size analysis should be added to other experimental and

geochemical studies to obtain more complete results from the origin of the magma. One of the key features of numerical textural studies is the dispersal of crystal sizes. However, the study on the matter was started 120 years ago, but until 30 years ago, the investigations did not obtain much development. The main paper by Cashman and Marsh (13) focused on this subject.

Geological setting

Gysian region is located in the geological map of 1: 10,000 Silvana (14) in the south of Urmia between longitudes of N44' 44" to 44' 56" and latitudes of E37' 07" to 37' 16". This region is a continuation of the northwest of the Sanandaj-Sirjan zone in terms of structural location. Sanandaj-Sirjan zone, the most complex structural zone in Iran, and the Palaeozoic and Mesozoic rocks have been marked by at least two syn-

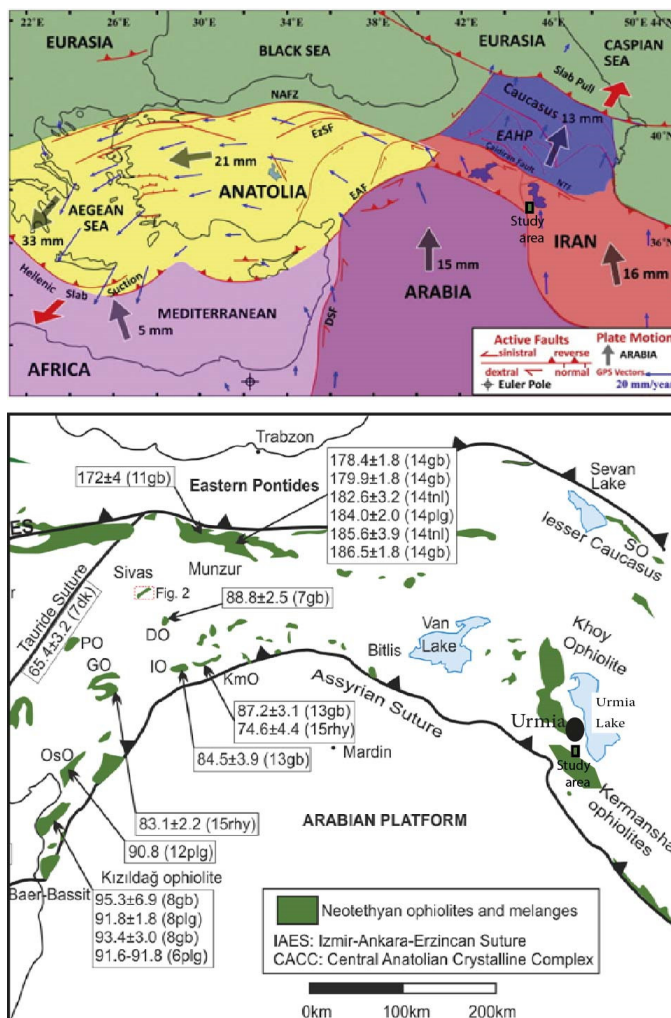


Figure 1. Location of Northwest of Iran (study area) in large scale geodynamic map of the region in relation to the Neo-Tethys subduction between the Arabian plate and Central Iran micro-continents.

tectonic dynamo-thermal deformations (15). This zone is part of the Zagros Mountains and the Alpine-Himalayan Orogenic System, which is formed by the convergence between the northern part of Gondwana and southern Eurasia (16). The direct direction of this zone in the distance between Urmia and Esfandageh locally represents the strike-slip system, which shows the dominance of the shear tectonic regime (straight line) at the junction of two Arabian-Iranian tectonic plates (17-18). The Sanandaj-Sirjan area extends from the Sabzevaran fault in the southeast to the Turkish-Iranian border in northwestern Iraq and from there to southeastern Anatolia, Turkey (Figure 1). Neo-Thetys

subduction probably began in the Cretaceous (19). Subduction to the north of Neo-Tethys in the Early Jurassic (below the Turan platform in Eurasia) separates a new set of northwestern trends from the passive margin of Gondwana, including the Sanandaj-Sirjan subcontinent and the Lesser Caucasus (20) and the subcontinents of Kirsehir and Sakarya in Turkey (21) and the formation of the Pindos Ocean (20).

Security considerations have so far prevented detailed studies in the Iran-Iraq boundary, so this article is one of the first introduces of the Gysian Silvana ophiolite in southern Urmia (Figure 2a). So far, there has been no ophiolite spot in large-scale maps of the foothills of

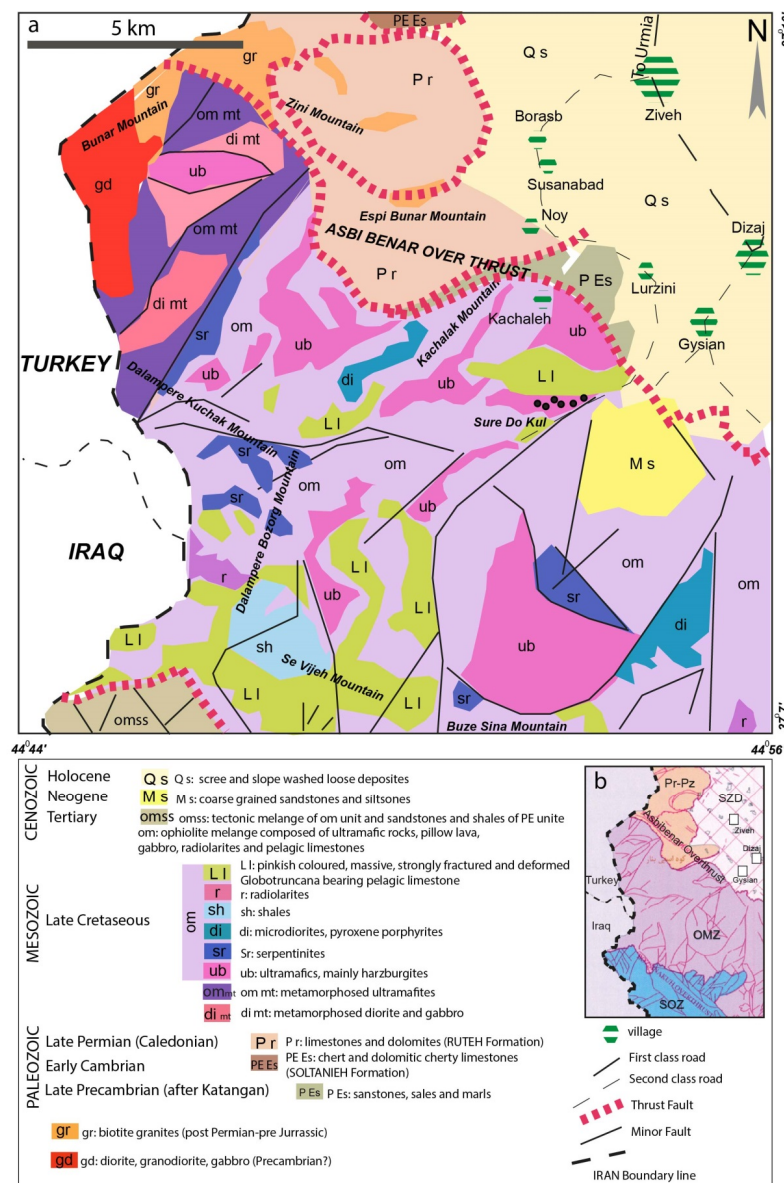


Figure 2. a: Simplified geological map of the Gysian Silvana ophiolitic region (14). b: The Silvana ophiolite subzones.

southeastern Turkey in Hakkari province (eastern Turkey), including the Goleman and Elazig ophiolites (22); after entering Iran, the ophiolites of Kermanshah (23) and Kurdistan Province. The author hopes to present the results of this research as a starting point for research on these ophiolites. The age of the ophiolite formation is most likely the Late Upper Cretaceous to Paleocene, such as another part of the Sanandaj-Sirjan zone, related to the NeoTethys ocean subduction. Ar-Ar, dating from the ophiolite rocks of Dalamper Mountain, Silvana, shows an age of 94 Ma (24).

Structurally, the Silvana region is divided into five sub-zones (Figure 2b): The ophiolite mixed zone (OMZ), which is characterized by a reverse thrust fault from the north with the Silvana-Ziveh depression zones (SZD), Precambrian-Paleozoic unit (Pr-Pz) and Molasses unit (Mo) is bordered and adjacent to the south with the ophiolite-sedimentary mixed zone (SOZ) and metamorphic zone (MZ).

Materials and Methods

For petrophysical parameters measurement, we practice 2D thin section microphotographs of the samples, using whole slide imaging, microvisioner technique, classified the images, and analyze the file using image processing software, Digimizer for measuring width, length, area, and crystals roundness. CSDCorrections software (25) was used to calculate the CSD patterns in 3D, slope, and intercept values of the curve.

Results

Microstructures

Orthopyroxene crystals are usually altered around or along with fractures and become bastites or other secondary minerals. Basting begins in the presence of existing fractures and gradually takes over the entire crystal. Excess iron is dispersed in the form of magnetite around the crystal, making it easier to identify the mineral boundaries (magnesium-containing components have migrated to serpentine). This is normal in serpentinites (26). Lizardites are low-temperature serpentine minerals that form at lower temperatures (260°C) and are among the most common minerals formed in olivine pseudomorphs. They were significantly found in the lower degrees of metamorphism of the greenschist facies, and due to progressive metamorphism up to the top of the greenschist facies, they converted into high-temperature serpentine polymorphs (27).

In the microscopic sections of the study area, the serpentinization of the olivines began around the crystal and its fractures and expanded to lizardite. Due to

progressive serpentinization, no trace of pseudomorphic olivine remains, and only serpentine mineral is seen along with magnetite. The mineral content of lizardite was high. Chrysotile begins to grow in the rock when there are olivines left in the rock, and they have become lizardite sheets. At this stage, the chrysotile begins to grow as very thin fibrous in the veins. Chrysotile fibers need support for nucleation and growth, and when used to grow from the wall surface, they use the exact location as support. This type of nucleation is called heterogeneous nucleation. Chrysotile is detectable in fibrous form and is more common in fractures and fissures in the form. It grows in the form of thin blades utterly perpendicular to the fracture wall. In general, two types of chrysotile filaments are seen in the study area vertical chrysotile filaments, and the other is oblique filaments. The presence of chrysotiles in the form of cross fibers in the background of other serpentine minerals indicates the delayed formation of chrysotiles under static conditions. In addition to chromite (cr-spinel crystals), which are coarse-grained and brown in plane-polarized light with a skeletal texture, they are sometimes found in sections of opaque minerals (magnetite). These minerals are finely dispersed throughout the section. Mesh texture is prevalent in these rocks. The serpentine from these textures is lizardite. The streaks around the olivine follow precisely the original shape of the crystal. If the primary fractures in the olivine grains are common and parallel, the serpentinization and formation of lizardite veins also occur in parallel with these regular fractures and finally form the band texture of the olivine (28). With the removal of pressure and an increase in the volume of peridotite rocks, regular and multifaceted fractures are formed in olivine by the fluid flow of the fractures (29). They begin to grow, with more fluid penetrating the fractures and continuing the process of serpentinization; lizardite grows in the same way as before and moves toward the center of the olivine. This cycle continues until there is no olivine left or the fluid enters is over.

Next, the remaining olivines between the mesh, hourglass, polygonal, or band textures are re-affected by the serpentinization process, and destroyed, leaving no grains and they have been substituted by serpentine and magnetite. The development of lizardite in the central part can depend on factors such as the difference in fluid composition at this stage compared to the previous stage, the difference in temperature and pressure conditions during the reaction, or the difference in olivine composition in the center relative to the margin (30). The studied samples are similar to those of Oman ophiolite mantle peridotites and serpentinized ophiolites of Kerman province, which tolerate 60% serpentinization

and include mesh and pseudomorphic textures containing chrysotile and magnetite streaks (31). Fabric for relative preferential orientation has also been observed in these rocks. Schistosity is caused by the orientation of serpentine grains, which can result from simultaneous growth with their tectonics (32). At the boundary of the olivine fragments, due to stretching, empty spaces are created that are suitable for the growth of any serpentine mineral. In serpentinite, due to serpentine sheet minerals, when the stress is received, the sheets slide on top of each other and form regular processes. By forming a preferential orientation, both horizontal (slippery) and vertical (slightly elongated) stresses are better tolerated by the rock. The ribbon or strip growth of chrysotiles has also been observed in rocks in meso- and microscopic samples, usually accompanied by veins and masses of magnetite. This texture may be related to deformations that correspond with the replacement of rocks on the ground. When orthopyroxene crystals have become bastitization, or the remnants of intact olivine crystals act as porphyroclasts and serpentines with a striped texture are placed around the crystal, the ocular texture is formed.

The Gysian serpentinite mineralogy (chrysotile and magnetite) is similar to the Alpine serpentinites of Auckland (33). It shows that these rocks have not further subducted to the degree of antigorite formation and have formed at temperatures below 300° C (34). In the following stages, with tectonic action and thrust faults in the region and dehydrating and increasing the rock volume (35) and consequently decreasing the density (36), the ascent to the surface has occurred. This stage is accompanied by deformation and the occurrence of transverse fractures at the ultramafic boundary and may have destroyed some previous fabrics and intensified the sheeted appearance of the rocks, causing the chromite (Cr-spinels) to fragment. The formation of network textures and filling of veins with calcite has also occurred at this stage and near the surface. In contrast, mesh and bastite textures are formed in the first stages of serpentinitization.

Discussion

A close look at the microstructure of serpentinites

In the absence of obvious deformation, serpentinites in the form of isotropic rocks have a mesh texture at the matrix that hosts the bastite blades. Networks usually have specific cores and margins. Bastites and lattice nuclei often have similar mineralogy, a combination of serpentine minerals, including chrysotile, polygonal serpentine, proto serpentine, and lizardite blades. In the core of the networks, the serpentine has a random

orientation, while in the bastite, regular (nanometer-thick) lizardite blades may fill the space between the random serpentines. The lattice rim is more crystalline than anywhere else and consists of lizardite micrometer fragments with an axis perpendicular to the core/rim boundary (37). Thus, in networks, lizardite often grows in regular directions, both of which are detected by compensator blades in a polarizing microscope. The lizardite (001) plates are usually maintained from one network to another, creating a three-dimensional interlocking skeleton with two vertical CPO plates. In Gysian serpentinites, as in the same case (in southern Tuscany, Italy), the thickness of the blue and yellow margins is almost equal in all rocks, and the volume occupied by the nucleus (pink) is larger than the space created by the margins (Figure 3). These fine and precise mineralogical and microstructural differences in the location of minerals have a significant effect on the local strength of serpentinites and cause heterogeneous responses by the rock to stresses (38).

In some Gysian samples, deformable traces have been found in the bastites (Figure 4 a, b), which are folds and kinking in the bastite blades marked by the cleavage levels of pyroxenes. Brittle deformation was also sometimes observed, leading to cracks in the bastites and through which chrysotile veins of the strip or blade type passed (39) (Figure 4 c-g). The progression of the deformity led to more rounding of the bastites and bypassing the lizardite (001) plates around the bastites, which itself created an augen texture (Figure 4 h). Considering the predominant phase of chrysotile and referring to grade petrogenetic diagrams (40) to know the stability field of chrysotile mineral, it is known that the maximum temperature of this mineral is 300 to 400° C at low to medium pressures (less than 10 kbar) (34). Therefore, in the absence of antigorite in these rocks, the depth at which Gysian serpentinites were formed was more minor than 50 km.

An overview of the Mineral chemistry and Whole-rock geochemistry

To achieve the composition of the main minerals in the rocks, several samples were analyzed as EPMA (45). Based on this, the remaining olivines were ferrohorthonolithic composition, Cr-spinels had the chromite composition, clinopyroxenes were hedenbergite, and orthopyroxenes were left over from serpentinitization were ferrosilite (41). The geochemistry of the Gysian rocks is similar to the mantle serpentinites studied along the Neo-Tethys, for example, with the serpentinites of Massio Voltri in the Italian Alps or with the average subducted

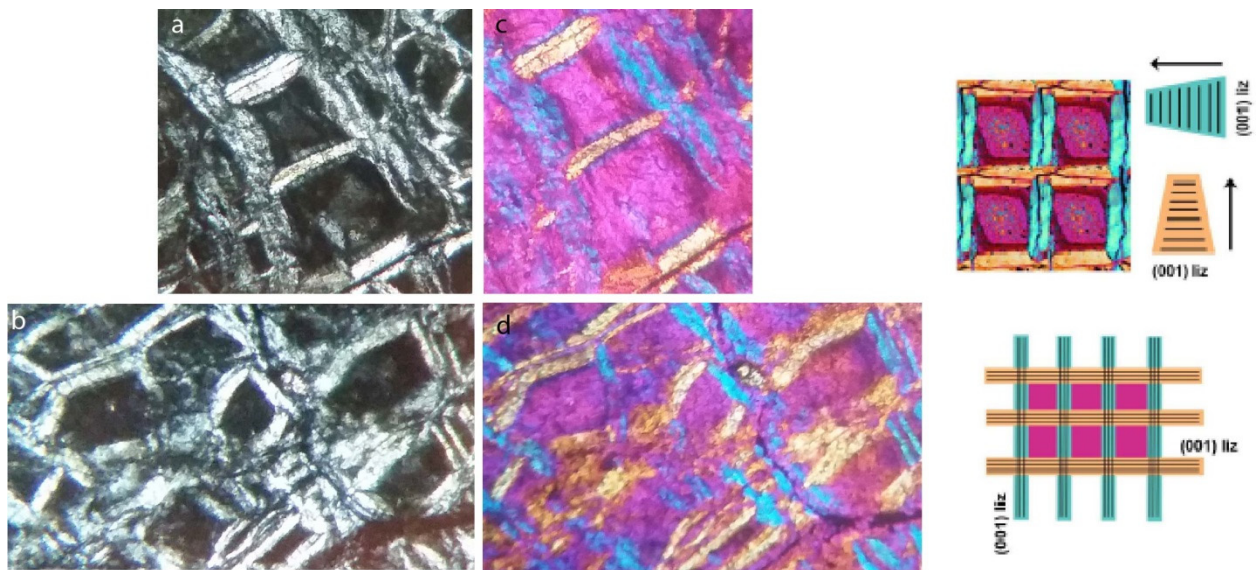


Figure 3. The Microstructures of mesh cells in the Gysian serpentinites. a and b are the cross-polarized photos and c and d taken after gypsum compensator use. The core of each cell, the pink area, is a less crystallized random matter which is surrounded by the lizardite [001] plates, in blue and yellow color.

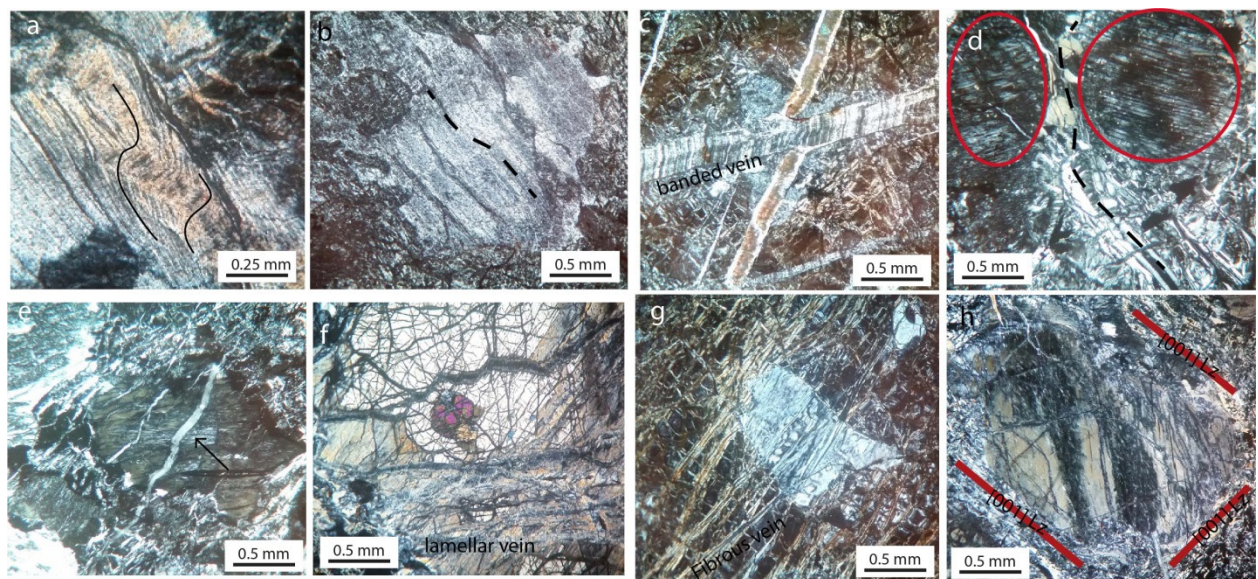


Figure 4. a, b Ductile deformation formed microfolds and kinks in bastites. c to g Brittle deformation including cracks, banded, lamellar and fibrous veins fragmented the bastites. h Progressive deformation formed rounding of bastites which are bypassed with [001] plates of lizardites and result in the augen texture. All of them are XPL.

serpentinites (42). These rocks are 95 to 100% serpentine and their LOI is about 12 to 13%. This number indicates their moderate to high serpentinization. In the triple chart based on LOI, the composition of Gysian serpentinites is precisely similar to the world average serpentinites and is very close to the global standard (UB-N) composition (43).

The content of intermediate metals such as Sc, V, Co,

Ni, Cr, and Cu in these rocks is significant, indicate high levels of olivine and orthopyroxene in the primary protolith and except for the negative anomaly of titanium in other elements similar to the primary mantle (44). Due to the low levels of titanium in these rocks, protoliths from dunite to harzburgite are evaluated. Referring to the geochemical characteristics of three types of serpentinites, including abyssal, mantle wedge, and

subducted, it is clear, especially in terms of the abundance of titanium (more than 30 to 150 ppm) and high Yb (0.1 to ppm), as well as significant enrichment of FME during refertilization, Gysian serpentinites are similar to subducted species (44).

CSD

The dynamic power of kinetic procedures in igneous rocks can be measured under-cooling or super-saturation of the association (45). The resulting crystal population is altered by mechanical factors such as sorting, coarsening, Ostwald ripening, or subsequent mixing (46). The primary functions that control growth textures are the nucleation rate, which is a function of time, and the growth rate, which depends on the time of growth and size. The common assumption is that the growth rate is independent of size. Of course, it is not always possible to ensure that the growth rate is not very dependent. For a crystal in such an environment:

$$n'_V(L) = n'_V(0)e^{-L/G\tau}$$

This is corresponding to the long dimension of all crystals with a linear CSD pattern of size zero to eternity. Items such as Ostwald-ripening in metamorphic rocks (10), mixing of two magmas in volcanic rocks (47), length of magma residence time (12), filter pressing, and crystal accumulations lead to variations and curve in the straight-line CSD pattern (46). The chromite crystals, because of their importance in crystallization history determination, different shapes and sizes in thin sections, characteristic crystals (Figure 5), and economic valuables in the Gysian serpentinites, are selected for CSD studies are selected.

We prepared a large sectional 2D image from the rocks using whole slide imaging (WSI) scanner. Then images are processed with Digimizer software to measure the width, length, area, and other physical data for chromites. To convert the 2D data to 3D, CSDCorrections (25) software is used, and CSD patterns are illustrated in Figure 6. CSD patterns for Gysian

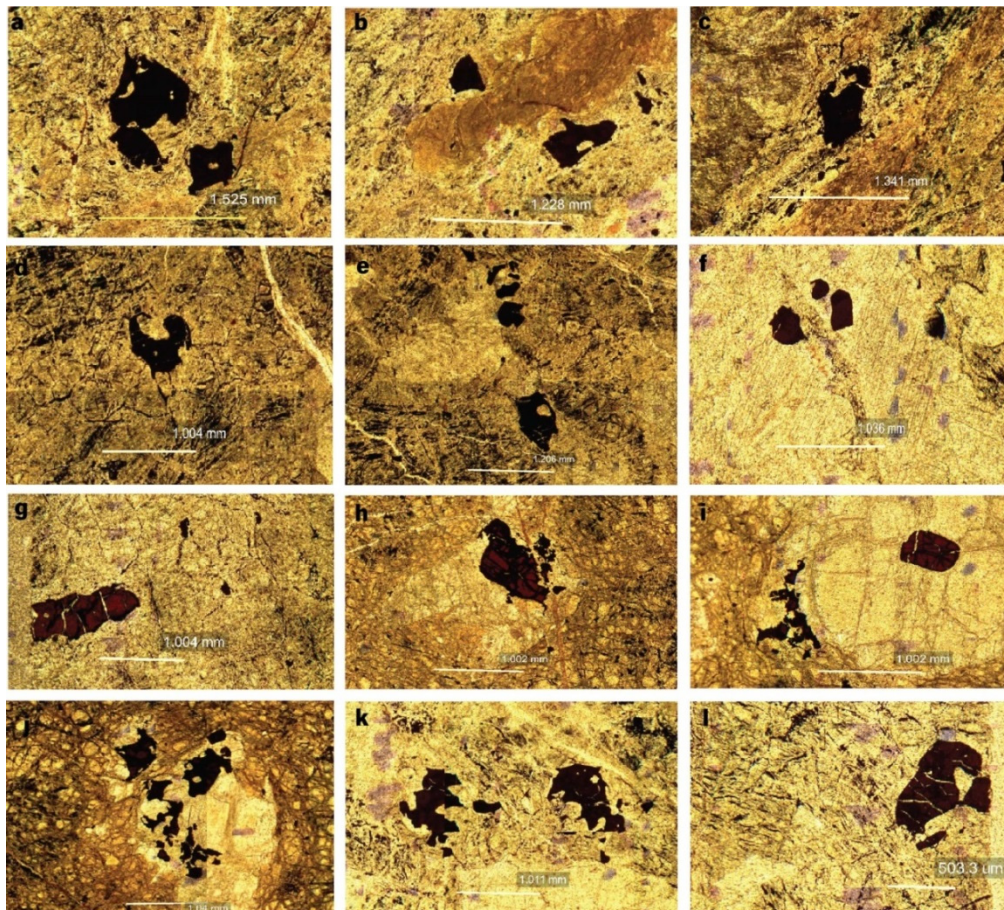


Figure 5. The chromatic spinels at the Gysian serpentinites. All of them gathered in PPL. The fragmentation due to the deformation and decompression in g, h, i, and l are clear.

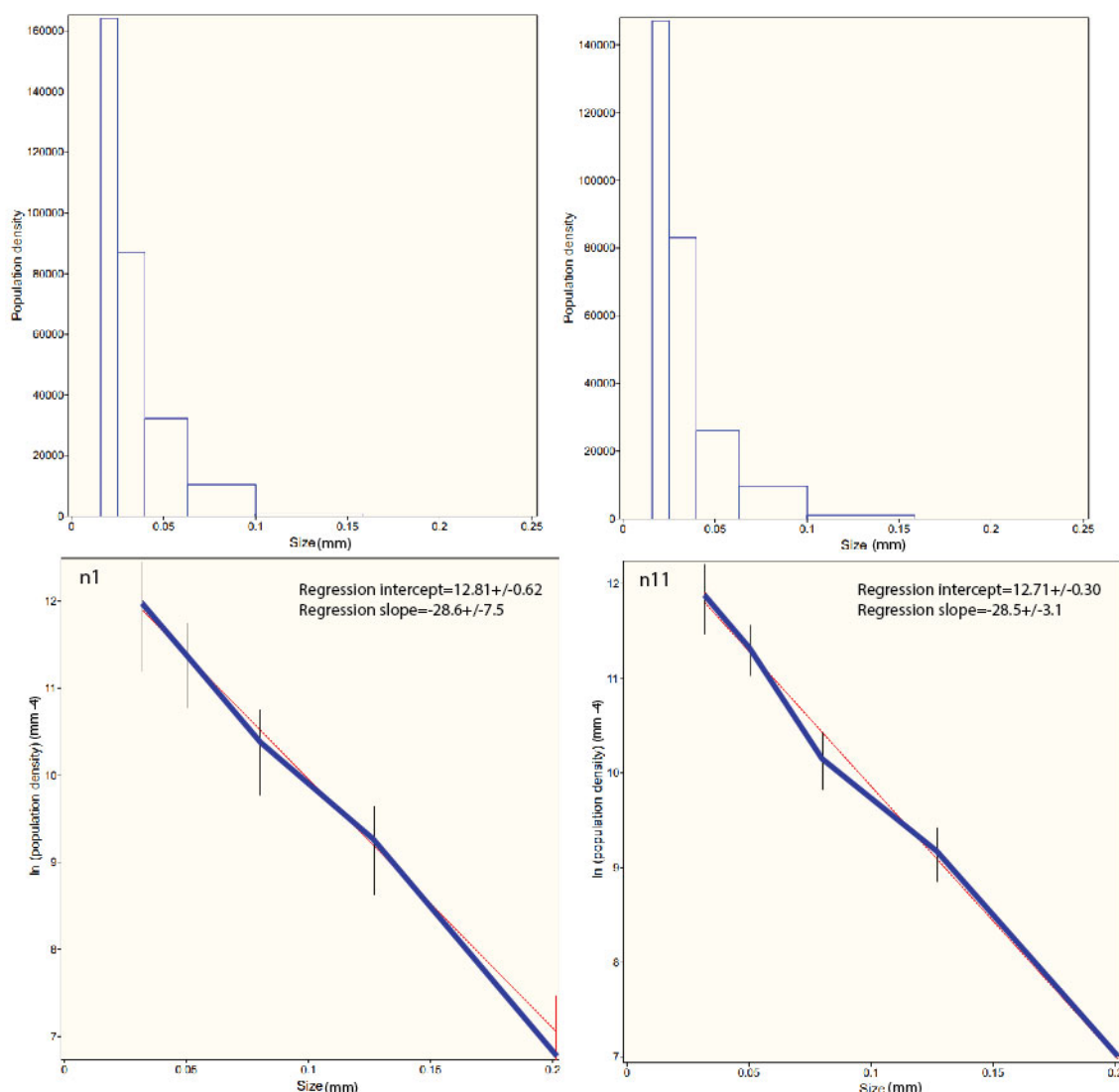


Figure 6. WSI photos of the thin sections, the crystal size histograms and CSD pattern of chromites in Gysian serpentinites. The intercept values (J/G) and slope of regression ($-1/Gt$) are written on the diagrams. There is typically one.

chromites are divided into three types: The first type is the linear pattern, which shows the steady-state crystallization with an intercept value of 12, which equals a nucleation rate/growth rate (J/G) of about 12. The regression slope is -28 which is related to the growth rate, and $Gt=1.28$ (Figure 6).

The second type has a non-linear concave down pattern which is the result of annealing or Ostwald ripening at a small size part with an intercept value of 13-15; therefore, $J/G=13-15$ and $Gt=1.33$ for them led to the slope of the pattern to be equal to -33 (Figure 6).

Coarsening connects the very small crystals to form a large crystal because of the grain boundary area reduction (GBAR) law. Another name for it is Ostwald ripening or

annealing (46). At the considerably deformed rocks, static recrystallization occurs on them, and if a fluid like water is available, it has measurable effects at lower temperatures. The Ostwald ripening caused the initial linear CSD pattern to change to a concave down form at the mean crystal size, and its shape only depends on the rate-adjusting growing. During this phenomenon, the small grains are dissolved and there is a decrease in the gain of large crystals (48). The small grains are unstable because of their high surface Gibbs free energy. If nucleation finishes and growth is possible, the CSD is affected by this ripening (48). It is a widespread occurrence in igneous crystallization. At these composite CSDs, we must interpret the patterns segment by

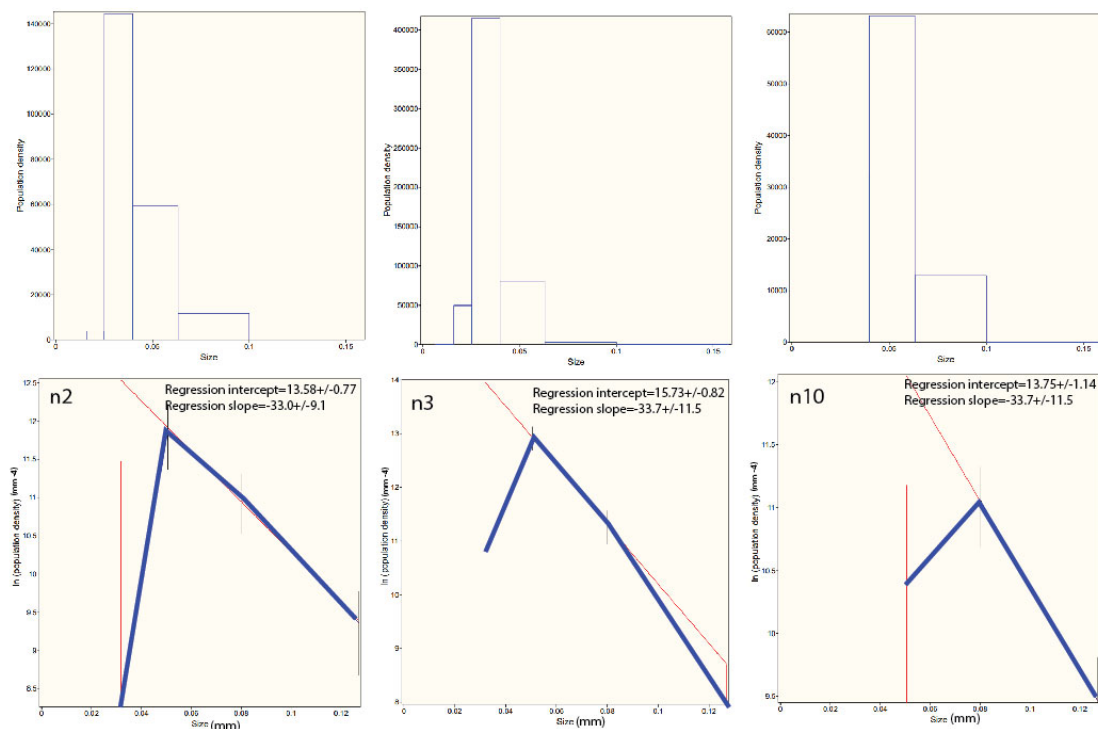


Figure 6. Continued. There is type two with annealing.

segment, and extract of nucleation and growth history is more complicated.

In the second type of CSD of chromites of serpentinites, we observe a single nucleation event followed by ripening during nucleation. Also, post-emplacement annealing may occur rapidly on them. As a result of the resorption of smaller grains, we show a curved pattern on the beginning part of the CSDs.

The third type is more complex and shows two population densities. It could be modeled by two crystal populations, small and large sizes which formed concave-up CSD patterns (Figure 6). The intercept value for small sizes is 12-18 demonstrating that the J/G is 12 to 18 for small crystals. The slope of the patterns for the small part is -40 to -60, indicating a range of Gt from 1.40 to 1.60. For large crystals, intercept values of 9-10 show the J/G to be 9-10 times for them and the slope of -7 to -10 shows that Gt is 1.7 to 1.10 for the large population. The J/G of small crystals is more than large ones, and thus, it is predicted that their growth is less. Considering the constant growth rate for crystals, from silicate materials, 10^{-9} cm/s or 10^{-10} cm/s, and using a slope of the patterns, it is determined that the growth of large chromites is six times longer than that of small crystals. The small crystals may be produced during arising of the residual peridotites or when the mafic minerals such as olivine or pyroxenes alteration exist. In the petrography

part, we show some coarse grains which are fragmented and cracked during arising (Figure 5). It is possible that these occurrences caused an increase in the rate of small grains, too.

Conclusion

One of the components of the Gysian Silvana ophiolite, south of Urmia near Iran's border with Turkey and Iraq, is serpentinites at the continuance of the Neo-Tethys suture zone. The significant phases are chrysotile, and magnetite and some rare cr-spinels (chromite), orthopyroxene, and clinopyroxene coexist among them. Almost all the peridotitic rocks are serpentinitized, and only remnants of mafic minerals remain. Several microstructures show stress and deformation tolerance in these rocks. One of them is the lizardite plates across the mass nucleus of less crystallized serpentine, which was discovered with the help of the compensator. Due to the lack of antigorite in these rocks, the subduction depth in this part of the Neo-Tethys was probably less than 50 km. This indicates the high gradient of the oceanic slab in the northern part of the Neo-Tethys in Iran and the reason for mélangé formation in ophiolite in this section of suture. In these rocks, the chromite size distribution was also investigated, and three types of patterns were separated including straight-line type, convex-up coarsening symptom, and a combination of two statistical

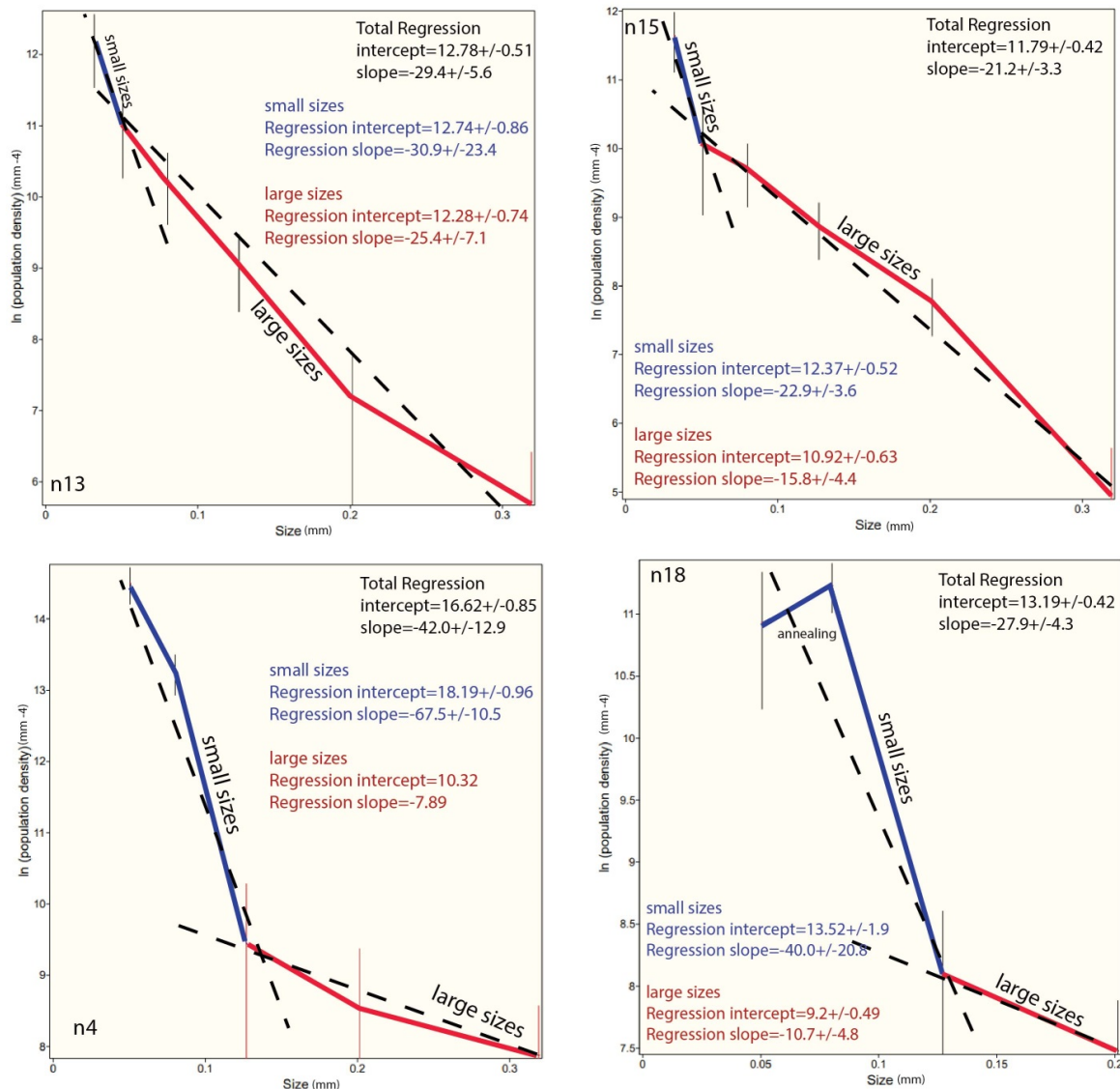


Figure 6. Continued for type three with two population densities.

populations. After the initial crystallization at steady-state (type one), annealing (Ostwald ripening), and co-integration of finer grains, they are constraining concave up in the fine grain part of the CSD pattern (type two). In some rocks, there is evidence of two categories of coarse and fine crystals with two intercept values and different pattern slopes. Such samples may have been caused by the fragmentation of coarse chromite grains confirming an increase in the number of fine grains or the creation of fine crystals due to deformation when rock arises, and decompression and alteration of mafic minerals like olivine take place. The result is that CSD patterns should be interpreted segment by segment and can never be given a general opinion for the whole pattern, especially

when it has a composite shape.

Acknowledgments

The author thanks the editors and reviewers of the Journal. The author received financial support from the Natural Science Foundation of Urmia University.

References

- Alexeiev DV, Kröner A, Hegner E, Rojas-Agramonte Y. Middle to Late Ordovician arc system in the Kyrgyz Middle Tianshan: From arc-continent collision to subsequent evolution of a Paleozoic continental margin. Gondwana

- Res. 2016;39:261-291.
2. Faure M, Lin W, Chu Y, Lepvrier C. Triassic tectonics of the southern margin of the South China Block. *Comptes Rendus Geoscience*. 2016;348(1):5-14.
 3. McCollom TM, Bach W. Thermodynamic constraints on hydrogen generation during serpentinization of ultramafic rocks: *Geochim Cosmochim Acta*. 2009;73(3):856-875.
 4. Frost BR, Evans KA, Swapp SM, Beard JS and Mothersole FE. The process of serpentinization in dunite from New Caledonia. *Lithos*. 2013;178:24-39.
 5. Hilairat N, Reynard B, Wang Y, Daniel I, Merkel S, Nishiyama N, Petitgirard S. High-pressure creep of serpentine, interseismic deformation, and initiation of subduction. *Science*. 2007;318(5858):1910-1913.
 6. Hattori KH and Guillot S. Volcanic fronts form as a consequence of serpentinite dehydration in the forearc mantle wedge. *Geology*. 2003;31(6):525-528.
 7. Tatsumi Y. The subduction factory: how it operates in the evolving Earth. *GSA Today*. 2005;15(7):4.
 8. Mével C. Serpentinization of abyssal peridotites at mid-ocean ridges. *Comptes Rendus Géoscience*. 2003;335:825-852.
 9. Bach W, Garrido CJ, Paulick H, Harvey J, Rosner M. Seawater-peridotite interactions: first insights from ODP Leg 209, MAR 15°N. *Geochemistry, Geophysics, Geosystems*. 2004;5(9):22.
 10. Modjarrad M. Geochemistry and crystal shape, size and spatial distribution in arc-related gabbro, Urmia, NW Iran. *Geochimica Acta*. 2022a; DOI: 10.1007/s11631-022-00557-8.
 11. Moazzen M, Modjarrad M. Contact metamorphism and crystal size distribution studies in the Shivar aureole, NW Iran. *Geol J*. 2005;40:499-517.
 12. Modjarrad M. Crystal size distribution of amphiboles from Bezow dacites, Urmia, Iran. *Neues Jahrbuch Fur Geologie Und Palaontologie Abhandlungen*. 2015;276:101-110.
 13. Modjarrad M, Sheykhbaglou S. Crystal size distribution of amphibole and plagioclase from Zanbil adakitic dacites, Urmia-Iran: Evidence for magma mixing and textural coarsening. *Acta Geodynamic Geomaterials*. 2016;181:89-101.
 14. Cashman KV, Ferry JM. Crystal size distribution (CSD) in rocks and the kinetics and dynamics of crystallization III. *Metamorphic crystallization. Contribut Mineral Petrol*. 1988;99:410.
 15. Hajmolla Ali A, Shahrabi M. Geological map of Silvana, N. 4964. Geological Survey of Iran. 2006; Tehran.
 16. Sheikholeslami MR. Deformations of Palaeozoic and Mesozoic rocks in southern Sirjan, Sanandaj-Sirjan Zone, Iran. *J Asian Earth Sci*. 2015;106:130-149.
 17. Alavi M. Regional stratigraphy of the Zagros fold-thrust belt of Iran and its proforeland evolution. *Am J Sci*. 2004;304(1):1-20.
 18. Allen MB, Kheirkhah M, Emami MH, Jones SJ. Right-lateral shear across Iran and kinematic change in the Arabia-Eurasia collision zone. *Geophysic J Int*. 2011;184(2):555-574.
 19. Aziz H, Asahara Y. Juvenile granite in the Sanandaj-Sirjan Zone, NW Iran: Late Jurassic-Early Cretaceous arc-continent collision. *Int Geol Rev*. 2013;55:1523-1540.
 20. Golonka J. Plate tectonic evolution of the southern margin of Eurasia in the Mesozoic and Cenozoic. *Tectonophysics*. 2004;381(1-4):235-273.
 21. Golonka J, Oszczytko N, Ślącza A. Late Carboniferous-Neogene geodynamic evolution and paleogeography of the circum-Carpathian region and adjacent areas. *Ann Societat Geologorum Poloniae*. 2000;70(2):107-136.
 22. Robertson AHF, Clift PD, Degnan PJ, Jones G. Palaeogeographic and palaeotectonic evolution of the Eastern Mediterranean Neotethys. *Palaeogeography Palaeoclimatol Palaeoecol*. 1991;87(1-4):289-343.
 23. Eren Rizeli M, Wang KL, Bingol AF, Beyarslan M. Mineral chemistry and petrology of mantle peridotites from the Guleman ophiolite (SE Anatolia, Turkey): evidence of a fore arc setting. 13th International Conference on Gondwana to Asia, At: Trivandrum, India. 2016;22.
 24. Shafaii Moghadam H, Li QL, Stern RJ, Chiaradia M, Karsli O, Rahimzadeh B. The Paleogene Ophiolite Conundrum of the Iran-Iraq Border Region. *J Geol Soc*. 2020.
 25. Alizadeh A. Dating of the southern Urmia colored mélange. 30th symposium of Earth Sciences of Iran 2012; Tehran.
 26. Higgins MD. Measurement of crystal size distributions. *Am Mineral*. 2000;85:1105-16.
 27. Page BM, De Vito LA, Coleman RG. Tectonic emplacement of serpentinite southeast of San Jose, California. *Int Geol Rev*. 1999;41:494-505.
 28. Azer MK, Khalil AE S. Petrological and mineralogical studies of Pan-African serpentinites at Bir Al-Edeid area, Central Eastern Desert, Egypt. *J Afr Earth Sci*. 2005;43(5):525-536.
 29. Francis GH. The serpentinite mass in Glen Urquhart, Invernesshire, Scotland. *Am J Sci*. 1956;254:201-226
 30. Hopkinson L, Beard JS and Boulter CA. The hydrothermal plumbing of a serpentinite-hosted detachment: Evidence from the West Iberia non-volcanic rifted continental margin. *Marine Geol*. 2004;204:301-315.
 31. Boudier F, Baronnet A, Mainprice D. Serpentine mineral replacements of natural olivine and their seismic implications: Oceanic lizardite versus subduction-related antigorite. *J Petrol*. 2009;51(1-2):495-512.
 32. Mohammadi N, Ahmadipour H, Peighambari S. Investigation of deformational behavior of serpentinites in Baft ophiolitic malange (Kerman) and its effects on the seismic potential of the region. *Iran J Geol*. 2013;6(24):3-17.
 33. Reinen LA. Seismic and aseismic slip indicators in serpentinite gouge. *Geology*. 2000;28(2):135-138.
 34. O'Brien J, Rodgers KA. Alpine-type serpentinites from the Auckland Province—III. Petrography, mineralogy, petrochemistry, and petrogenesis. *J Royal Soc New Zealand*. 1974;4(2):141-159.
 35. Evans BW. The serpentinite multisystem revised: chrysotile is metastable. *Int Geol Rev*. 2004;46:479-506.
 36. Iyer K, Austrheim H, John T, Jamtveit B. Serpentinization of the oceanic lithosphere and some geochemical consequences: constraints from the Leka Ophiolite Complex, Norway. *Chem Geol*. 2008;249:66-90.
 37. Christensen NI. Serpentinites, peridotites, and seismology. *Int Geol Rev*. 2004;46(9):795-816.
 38. Viti C, Mellini M. Mesh textures and bastites in the Elba retrograde serpentinites. *Eur J Mineral*. 1998;10:1341-1359.

39. Viti C, Collettini C, Tessei T, Tarling MS, Smith S. Deformation Processes, Textural Evolution and Weakening in Retrograde Serpentinites. *Minerals*. 2018;8:241.
40. Roumejon S, Cannat M, Pierre Agrinier P, Godard M, Andreani M. Serpentinization and Fluid Pathways in Tectonically Exhumed Peridotites from the Southwest Indian Ridge (62–65-E). *J Petrol*. 2015;56(4):703-734.
41. Bromiley GD, Pawley AR. The stability of antigorite in the systems MgO–SiO₂–H₂O (MSH) and MgO–Al₂O₃–SiO₂–H₂O (MASH): the effects of Al³⁺ substitution on high pressure stability. *Am Mineral*. 2003;88:99–108.
42. Rezaie MDA, Modjarrad M (2018). The Ultramafic rocks of Silvana ophiolite. 25th symposium of crystallography and mineralogy of Iran. 2018; Yazd, Iran.
43. Deschamps F, Godard M, Guillot S, Hattori K. Geochemistry of subduction zone serpentinites: A review. *Lithos*. 2013;178:96-127.
44. Abdollah K, and Modjarrad M. Serpentinites of Ziveh Gysian south of Urmia, 3th international Congress of Earth Sciences of Iran. 2018; Tehran.
45. Modjarrad M. Petrology of the Maku - Poldasht young lavas: Attitude to the olivine and bubbles sizedistribution. *Applied Geochemistry (AAG)*, in press 2022b; (in Persian).
46. Cashman KV. Crystal Size Distribution (CSD) Analysis of Volcanic Samples: Advances and Challenges. *Front Earth Sci*. 2020;8.
47. Higgins MD. Quantitative textural measurements in igneous and metamorphic petrology. Cambridge University Press. 2006; New York, 277p.
48. Modjarrad M. Crystal size distribution studies on the leucite, pyroxene and olivine at the eastern Urmia Lake volcanic rocks- magma mixing possibility and residence time at the chamber. *Iran J Crystallography Mineral*. 2019;27:55-68 (in Persian).
49. Marsh BD. On the interpretation of crystal size distributions in magmatic systems. *J Petrol*. 1998;39:553–600.

Heavy Tailed Distribution of Binary Classification Model

D. M. Oladimeji*, E. S. Oguntade, S. O. Olarenwaju

Department of Statistics, Faculty of Sciences, University of Abuja, Abuja, Nigeria

Received: 8 August 2023 / Revised: 3 November 2023 / Accepted: 12 November 2023

Abstract

The proposed research incorporates the utilization of a heavy-tailed skewed distribution referred to as the inverse Weibull as a link function in the context of a binary classification model. This selection is motivated by the need to address the existence of rare or extreme events in random processes. The study introduces a model that relies on the Inverse Weibull (TYPE II) distribution, and the estimation of model parameters is accomplished through the application of maximum likelihood methods. When the outcomes are compared to those derived from other link functions such as TYPE I (Complementary log) and TYPE III (Weibull) based on extreme value distributions using standard classification data as well as real-life data, it becomes apparent that the Inverse Weibull (TYPE II) model exhibits exceptional performance. This assessment of performance takes into account several criteria, encompassing the Akaike information criterion, Bayesian information criterion, Area under the curve, and Brier scores. In conclusion, the study establishes that the proposed model demonstrates considerable robustness in its performance, rendering it a viable choice for the modeling of binary classification problems.

Keywords: Extreme value Distribution; Inverse-Weibull; Classification Model; Heavy-Tailed Distribution.

Introduction

Classification involves determining the category to which an observation belongs. The application of classification models extends across various aspects of life. In the realm of medical science, the significance of classification models cannot be overstated, given the field's structure and operations. A common scenario is assigning a diagnosis to a patient based on observable patient characteristics, including gender, blood pressure, and the presence or absence of specific symptoms. These individual observations are often transformed into quantifiable properties referred to as features or covariates. Classifiers function by comparing

observations to previous ones using a similarity or distance measure.

Unique modeling approaches for classification problems include linear discriminant models, probit models, and logit models, which are commonly employed by frequentist statisticians. Bayesian statisticians, on the other hand, use methods like naïve Bayes and Bayesian networks. Additional methods include dynamic linear models (1), nonlinear models, hidden Markov models, and more (2).

In the general linear model, numerous link functions have been developed by researchers for modeling classification data, which include the inverse Gaussian, logistic distribution, and a class of two-parameter link

* Corresponding author: Tel: 23407032325611; Email: oladimejidamilare@yahoo.com

functions that also generalize the logit model. Some studies have explored skewed distributions, such as the Weibull (3, 4). However, the Weibull distribution, being a member of the Extreme Value distribution family, exhibits a lighter tail compared to the Gumbel distribution. This characteristic may limit its capability to capture extreme or rare events resulting from random processes.

In this proposed study, we adopt a heavy-tailed skewed distribution known as the inverse Weibull as a link function within a binary classification model. This choice enables us to account for extreme or rare events that may occur in random processes.

Materials and Methods

1. Extreme Value Distribution

Extreme Value Theory (EVT) is a branch of statistics that deals with the stochastic behavior of extreme events found in the tails of probability distributions. A stochastic model represents a situation where uncertainty is present, essentially a model for a process that exhibits some degree of randomness. EVT's primary goal is to predict the probabilities of rare events that are greater (or smaller) than previously recorded events. An extreme value distribution serves as a limiting model for the maximums and minimums within a dataset (5). A limiting distribution simply models how large (or small) your data is likely to become. Let Y be a random variable, represented as $Y = (y_1, y_2, y_3, \dots)$. Extreme value distributions are categorized into three groups: Type I, Type II, and Type III. These three types are defined as follows, with parameters μ , α , and β , corresponding to the location, scale, and shape parameters, respectively.

Type I

$$f_I(y) = \frac{1}{\beta} \exp\left\{-\frac{y-\mu}{\beta} - \exp\left(\frac{y-\mu}{\beta}\right)\right\} y \in \mathcal{R} \quad (1)$$

$$F_I(y) = \exp\left\{-\exp\left(\frac{y-\mu}{\beta}\right)\right\} \quad (2)$$

Type II

$$f_{II}(y) = \left(\frac{\alpha}{\beta}\right) \left(\frac{y-\mu}{\beta}\right)^{-\alpha-1} e^{\left\{-\left(\frac{y-\mu}{\beta}\right)^{-\alpha}\right\}} \quad (3)$$

$$y \geq \beta, \alpha > 0$$

$$F_{II}(y) = \exp\left\{-\left(\frac{y-\mu}{\beta}\right)^{-\alpha}\right\} \quad (4)$$

Type III

$$f_{III}(y) = \left(\frac{\alpha}{\beta}\right) \left(\frac{\mu-y}{\beta}\right)^{\alpha-1} e^{\left\{-\left(\frac{\mu-y}{\beta}\right)^{\alpha}\right\}} \quad (5)$$

$$y < \mu, \alpha > 0$$

$$F_{III}(y) = \exp\left\{-\left(\frac{\mu-y}{\beta}\right)^{\alpha}\right\} y < \mu \quad (6)$$

The basic idea is that three types of extreme value distributions (EVD Types I, II, and II) can model the extremes from any set of data, as long as the distribution is "well-behaved" (5). Figure 1, depicts the tail of the three extreme value distributions the figure shows that TYPE II has a heavier tail than TYPE I and TYPE III.

2. Weibull Distribution and Inverse Weibull Distribution

The Extreme value distribution of type III was named after a Swedish engineer and scientist called Waloddi Weibull, well-known for his work on the

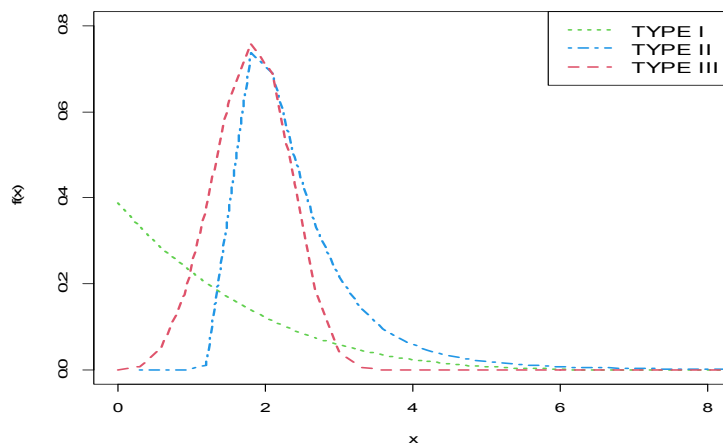


Figure 1. Plot of Extreme Value Distribution

strength of materials and fatigue analysis (6). The Weibull distribution was first created to analyze the distribution of material lifetimes or failure times in the realm of material science. It proved highly valuable in comprehending material behavior and predicting potential failures Let X represent a random variable that denotes the lifetime or time to occurrence of an event. The Weibull distribution is defined as

$$f(x) = \left(\frac{\alpha}{\beta}\right)\left(\frac{x - \mu}{\beta}\right)^{\alpha - 1} e^{-\left(\frac{x - \mu}{\beta}\right)^\alpha} \quad (7)$$

$x \geq \mu, \beta \neq 0, \alpha \in \mathcal{R}$

In equation 7 (above), if $\alpha = 1$, the Weibull distribution function reduces to the Exponential model, whereas for $\alpha = 2$, it mimics the Rayleigh distribution which is mainly used in the telecommunications field (6). Furthermore, it resembles the Normal distribution when $\alpha = 3.5$.

Given that X follows the Weibull distribution of $X \sim w(\mu, \beta, \alpha)$, let $y = \frac{\beta^2}{X - \mu}$'s call it reciprocal transformation to a Weibull distribution X therefore the newly generated distribution is inverse Weibull and is stated as follows:

$$f(y) = \left(\frac{\alpha}{\beta}\right)\left(\frac{y - \mu}{\beta}\right)^{-\alpha - 1} e^{-\left(\frac{y - \mu}{\beta}\right)^{-\alpha}} \quad (8)$$

$y \geq 0, \beta \neq 0, \alpha \in \mathcal{R}$

The following represent essential statistical properties of the Inverse Weibull distribution.

$$E(y) = \int_0^\infty y \left(\frac{\alpha}{\beta}\right)\left(\frac{y - \mu}{\beta}\right)^{-\alpha - 1} e^{-\left(\frac{y - \mu}{\beta}\right)^{-\alpha}} dy$$

$$E(y) = \mu + \beta \Gamma\left(1 - \frac{1}{\alpha}\right) \text{ where } \Gamma \text{ is the gamma function}$$

$$0.5 = \int_0^m \left(\frac{\alpha}{\beta}\right)\left(\frac{y - \mu}{\beta}\right)^{-\alpha - 1} e^{-\left(\frac{y - \mu}{\beta}\right)^{-\alpha}} dy$$

$$\text{Median} = \mu + \frac{\beta}{\alpha \sqrt{\log_e 2}}$$

$$E(y - \mu)^2 = \int_0^\infty (y - \mu)^2 \left(\frac{\alpha}{\beta}\right)\left(\frac{y - \mu}{\beta}\right)^{-\alpha - 1} e^{-\left(\frac{y - \mu}{\beta}\right)^{-\alpha}} dy$$

$$\text{Variance} = \beta^2 \left(\Gamma\left(1 - \frac{2}{\alpha}\right) - \left(\Gamma\left(1 - \frac{1}{\alpha}\right) \right)^2 \right)$$

$$\text{Skewness} = \frac{\Gamma\left(1 - \frac{3}{\alpha}\right) - 3\Gamma\left(1 - \frac{2}{\alpha}\right)\Gamma\left(1 - \frac{1}{\alpha}\right) + 2\Gamma^3\left(1 - \frac{1}{\alpha}\right)}{\sqrt{\left(\Gamma\left(1 - \frac{2}{\alpha}\right) - \Gamma^2\left(1 - \frac{1}{\alpha}\right)\right)^3}}$$

Figure 2 depicts the relationship between extreme value distributions and the inverse Weibull distribution.

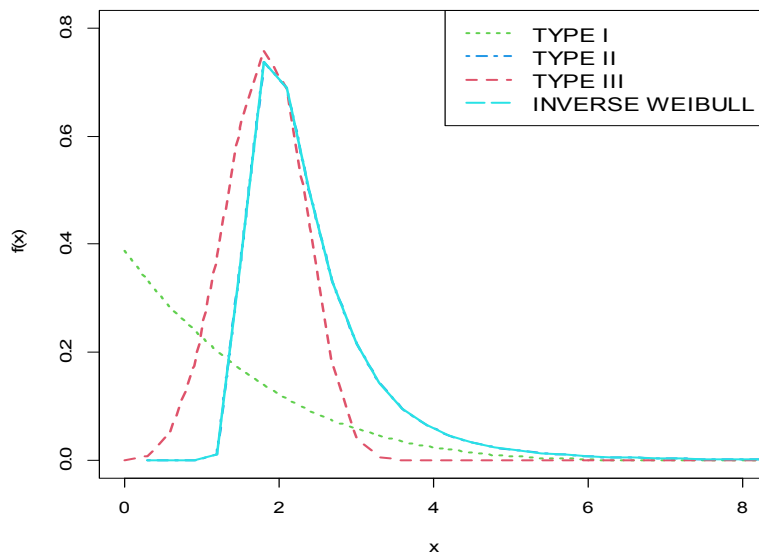


Figure 2. Plot of Extreme Value Distribution and Inverse Weibull distribution

The figure illustrates that the inverse Weibull and TYPE II extreme value distributions are equivalent and exhibit heavier tails compared to other distributions.

3. Inverse Weibull link Function

The study introduces a novel link function that relies on the highly asymmetric (inverse Weibull) distribution. This new link function is expressed as:

$$F(y) = e^{-\left(\frac{y-\mu}{\beta}\right)^{-\alpha}}$$

$$Y = \lambda_0 + \lambda X_i'$$

$$\Pr(y_i = 1 / w_i = \lambda^0_0 + \lambda^0 X_i) = F_y(\lambda^0_0 + \lambda^0 X_i') =$$

$$F_{F_y}(\lambda^0_0 + \lambda^0 X_i')$$

$$e^{-\left(\frac{\lambda^0_0 + \lambda^0 X_i' - \mu}{\beta}\right)^{-\alpha}}$$

$$= e^{-\left(\frac{\lambda^0_0 + \lambda^0_i X_{ii} + \dots + \lambda^0_k X_{ik} - \mu}{\beta}\right)^{-\alpha}}$$

Pr

$$(y_i = 1 / X_i = x_i) = e^{-\left(\frac{\lambda^0_0 - \mu}{\beta} + \frac{\lambda^0_i X_{ik}}{\beta} + \dots + \frac{\lambda^0_k X_{ik}}{\beta}\right)^{-\alpha}}$$

$$\text{let } \lambda_0 = \frac{\lambda^0_0 - \mu}{\beta} \text{ and } \lambda = \frac{\lambda^0_i}{\beta} \dots \frac{\lambda^0_k}{\beta}$$

While

$$\lambda_0 + \lambda x_i' > 0, \alpha > 0, \lambda_0 = \frac{\lambda^0_0 - \mu}{\beta} \text{ and } \lambda = \lambda^0$$

4. Estimation Method

Let Y be a random variable from the Bernoulli distribution then, its Probability Mass function (PMF) is defined as

$$\pi^{y_i} (1 - \pi)^{1-y_i} \quad y=0,1$$

The likelihood function of Bernoulli distribution and Inverse Weibull link is given by

$$L(\pi) = \prod_{i=1}^n \pi_i^{y_i} (1 - \pi_i)^{1-y_i}$$

$$\text{Where } \pi_i = e^{-\left(\psi\right)^{-\alpha}}$$

The likelihood function for the new link function can be written as

$$= \prod_{i=1}^n \left\{ e^{-\left(\psi\right)^{-\alpha}} \right\}^{y_i} \left\{ 1 - e^{-\left(\psi\right)^{-\alpha}} \right\}^{1-y_i}$$

Let $\lambda_0 + \lambda X_i'$ be ψ

Where $\lambda_0 + \lambda X = \Lambda X'$

$$\Lambda = \begin{pmatrix} \lambda_0 \\ \lambda_1 \\ \lambda_2 \\ \vdots \\ \lambda_k \end{pmatrix}$$

Consider a sample of size n from the binary response Y, with $\Pr[Y_i = y_i = 1] = \pi_i$ for $y_i=1, \dots, n$. we denote the observed observation as $U = \{n, Y = y, X = x\}$, where $y = (y_1, \dots, y_n)$ is the observed vector of Y and $X = (1, x_1, \dots, x_r)'$, is the observed design matrix of X $= (1, x_1, \dots, x_r)'$. Also, denote the Log Likelihood as LL.

$$LL = \sum_{i=1}^n y_i \log(\pi_i) + (1 - y_i) \log(1 - \pi_i)$$

$$= \sum y_i \log\left(e^{-\left(\psi\right)^{-\alpha}}\right) + (1 - y_i) \log\left(1 - e^{-\left(\psi\right)^{-\alpha}}\right)$$

$$= \sum -y_i \left(\psi\right)^{-\alpha} + (1 - y_i) \log\left(1 - e^{-\left(\psi\right)^{-\alpha}}\right)$$

Where Λ is a vector? A numerical method will be adopted to obtain the MLE for (Λ, α) .

5. Model Efficiency and Selection

In selecting the most competitive models, this study adopted the Log-likelihood(LL) value, Akaike Information Criterion(AIC), and Bayesian Information Criterion (BIC). Also, for goodness of fit Kolmogorov-Smirnov (KS) statistic was used, for classification performance, model accuracy and Brier Score were used.

Results

1. Roland Fisher Irish Data (Standard Data)

Roland Fisher Iris dataset which contains four features sepal length, sepal width, petal length, and iris Virginica (7). This dataset will be used as standard data to test the proposed model using Virginica as a species of interest while Setosa and Versicolor will be used as

Table 1. Comparison of the link functions under maximum likelihood Estimate for Standard Data

MODEL	LL	AIC	BIC	KS	Brier Score	Accuracy
TYPE II(INVERSE WEIBULL)	98.287	-184.58	-183.517	0.1333	0.1832	82.3%
LOGISTIC	-5.949	21.899	36.953	0.01431	0.0133	98.7%
TYPE I (COM LOG LOG)	-5.689	21.378	36.431	0.0141	0.0133	96.2%
TYPE III (WEIBULL)	9.90E+290	-1.98E+291	-1.98E+291	0.3333	0.3541	66.7%

LL=Loglikelihood, AIC=Akaike Information Criterion, BIC= Bayesian Information Criterion, KS= Kolmogorov-Smirnov

Table 2. Area under the curve for Irish data

	Obs	ROC Area	Std. Err.	[95% Conf. Interval]
Inweibullirish	150	0.8100	0.0261	0.75882 0.86118
Logisticirish	150	0.9986	0.0012	0.99621 1.00000
Comloglogirish	150	0.9990	0.0010	0.99709 1.00000
Weibullirish	150	0.540	0.0194	0.502 0.5779

Std. Err.

references.

The best model based on log-likelihood, AIC, and BIC is TYPE III (Weibull) followed by TYPE II (Inverse Weibull) while the logistic model performed better based on KS and Brier's score followed by TYPE I (Complementary log log). The coefficients of TYPE III (Weibull) distribution result in a very small standard error which makes all the coefficients highly significant. However, it has the lowest accuracy compared to other models (Tables 1 & 2). The Area under the Curve (AUC) in Table 2, revealed that both logistic and TYPE I (Complementary log log) were classified better than TYPE II (Inverse Weibull) and TYPE I (Weibull). However, TYPE II (inverse Weibull) has a higher AUC than TYPE I (Weibull). Also, in Table 3, the TYPE III model consistently reveals strong associations for all factors (constant, sepal length, sepal width, petal length, and petal width) with notably low p-values. The TYPE II and TYPE I models similarly display substantial

associations for certain variables. In contrast, the Logistic model generally suggests less robust associations with elevated p-values and a lack of uniformity in identifying significant predictors.

2. Stillbirth Data

Data used in validating the new proposed model were collected from six primary Health Centres across the six Area Councils of Federal Capital Territory of Nigeria. Data consists of patients who delivered babies in Federal Capital territory clinics in the year 2019. The information elicited from the patient's record were maternal age, antenatal status, birth size, gestational age, and birth outcome (alive or stillbirth).

Maximum likelihood estimates were obtained for the proposed model (Inverse Weibull), Logistic, Complementary log log, and Weibull. The most competitive model was selected based on the model efficiency method which includes Log-likelihood, AIC,

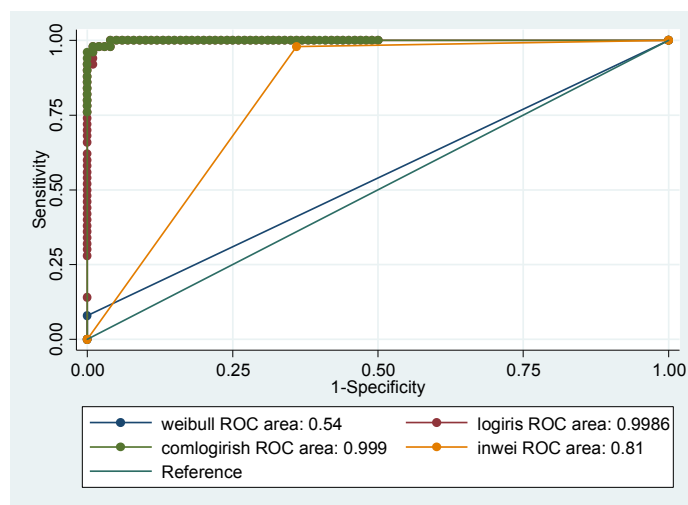


Figure 3. Area under curve for Irish

Table 3. Maximum Likelihood Estimate for Irish Data

	TYPE II (INVERSE WEIBULL)		LOGISTIC		TYPE I (COMPLEMENTARY LOG LOG)		TYPE III (WEIBULL)	
	Coeff(std.error)	p< z	Coeff(std.error)	p< z	Coeff(std.error)	p< z	Coeff(std.error)	p< z
Con	-2.28(1.005)	0.02	-42.638(25.708)	0.097	-31.937(17.511)	0.068	28.05(4.3E-145)	<0.0001
sepal.length	0.318(0.3265)	0.3301	-2.46(2.39)	0.303	-1.4629(1.387)	0.292	161(5.205E-145)	<0.0001
sepal.width	0.4267(0.2575)	0.097	-6.681(4.479)	0.136	-5.224(3.113)	0.093	84.14(9.44E-145)	<0.0001
petal.length	-0.529(0.266)	0.047	9.429(4.737)	0.047	6.1047(2.732)	0.025	99.89(9.44E-145)	<0.0001
sepal.width	2.23(0.431)	<0.0001	18.286(9.743)	0.061	15.1167(7.7519)	0.051	30.89(8.68E-145)	<0.0001
α	4.03(0.391)						80.84(5.72E-146)	

Con=Constant, Coeff=Coefficient, std.error=Standard error

BIC, KS, and Brier score. The inverse Weibull has the highest Log-likelihood, lowest AIC, and BIC, and second minimum both in KS and Brier scores. Also, it has a better sensitivity value than other models and it has almost the same accuracy with logistic (see table 4&5). The coefficient of the model shows that an increase in maternal age reduces the risk of stillbirth, booking for antenatal reduces the risk of stillbirth, increase in birth weight will the risk of stillbirth (see Table 7).

In both data examples, the Weibull model predicted value tend towards zero which was aligned with the assumption on which it was being built which affects its sensitivity and accuracy of prediction(5). Inverse Weibull unlike Weibull has both good sensitivity and accuracy of prediction. Also, the result in Table 6 revealed that both logistic and TYPE I (Complementary

log log) have 75% value of AUC, and TYPE II (Inverse Weibull) has 76% ability to differentiate between stillbirth and livebirth While TYPE I (Weibull) has 50%.

Discussion

The findings of this study show that Type II and logistic link functions are good in binary classification based on the results of model efficiencies such as loglikelihood, AIC, and Area under the curve. This result aligns with Tahir *et al.* (2016), who in their paper illustrated the application of at-site frequency analysis using relatively nontraditional probability distributions, adopting four methods of parameter estimation using annual maximum rainfall series from 1980 to 2015 from three sites: Muzaffarabad, Garhi Dupatta, and Kotli in

Table 4. Comparison of the link functions under maximum likelihood Estimate for Stillbirth data

MODEL	LL	AIC	BIC	KS	Brier Score
TYPE II(INVERSE WEIBULL)	-67.670	147.34	152.541	0.053	0.2126
LOGISTIC	-336.604	683.207	706.213	0.027	0.2147
TYPE I (COM LOG LOG)	-336.718	683.437	698.4899	0.358	0.3379
TYPE III (WEIBULL)	-1.90E+305	5.163E+302	3.8E+305	0.2377	0.2401

LL=Loglikelihood, AIC=Akaike Information Criterion, BIC= Bayesian Information Criterion, KS= Kolmogorov-Smirnov

Table 5. Comparison of Classification performance for different link functions

MODEL	Sensitivity	Specificity	Accuracy
TYPE II(INVERSE WEIBULL)	65.7%	82.7%	78.4%
LOGISTIC	49.1%	87.7%	78.5%
TYPE I (COM LOG LOG)	23.4%	79.5%	66.2%
TYPE III (WEIBULL)	1.14%	76.2%	76.2%

Table 6. Area under curve for stillbirth data

	Obs	ROC Area	Std. Err.	[95% Conf. Interval]
Inweibull	736	0.7650	0.0236	0.69879 0.81131
Logistic	736	0.7538	0.0221	0.71038 0.79720
Comploglog	736	0.7527	0.0224	0.70883 0.79649
Weibull	736	0.5048	0.0041	0.4967 0.5129

Std.Err. standard error

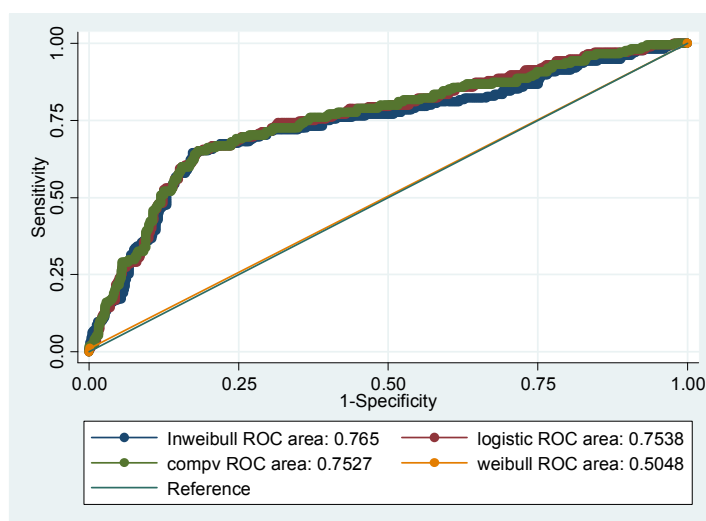


Figure 4. Area under curve for stillbirth Data

Table 7. Maximum Likelihood Estimate for Stillbirth Data

Variables	TYPE II (INVERSE WEIBULL)		LOGISTIC	
	Coeff(std.error)	p< z	Coeff(std.error)	p< z
Con	0.4437(0.2123)	0.03	-1.097(0.778)	0.158
Age	-0.0008(0.0023)	0.725	-0.008(0.009)	0.389
Booked	-2.333(0.3921)	<0.0001	-2.115(0.9937)	<0.0001
birth size	-0.0013(0.000357)	0.017	-0.231(0.151)	0.126
birth month	0.0228(0.0159)	0.154	0.0073(0.0668)	0.913
α	2.25(0.497)		-	-

Con=Constant, Coeff=Coefficient, std.error=Standard error

Azad Jammu and Kashmir, Pakistan (9). Two probability distributions, Fréchet (Type II) and Log-logistic were used as candidate distributions to model the annual maximum rainfall series at given sites. The result of the findings on stillbirth, which indicated that booking antenatal care significantly reduces the likelihood of stillbirth, is in tandem with the findings of Berhe *et al.* (2023) who concluded that "having a good quality of antenatal care significantly reduces antepartum stillbirth (10). Strategies need to be developed on the problems identified to improve the quality of ANC and reduce antepartum stillbirth significantly". This finding also aligns with the position of another study from Lagos State, Nigeria, by Orisakwe *et al.*, (2017), who opined that "The prevalence of stillbirth was high in the hospital during the study period (11). The majority of these deaths occurred during the antenatal period and were common in those women who did not receive ANC in the hospital. There is an urgent need to improve the quality of our obstetric healthcare services and encourage early referral of complicated pregnancies and labor to prevent

unnecessary fetal deaths due to preventable or manageable obstetric conditions". Another study from Ghana (Afulani, 2016) maintained a similar position with this finding; the author concluded that "Good quality ANC can improve birth outcomes in two ways: directly through preventative measures and indirectly through promoting deliveries in health facilities where complications can be better managed (12).

Conclusion

This study has presented a new link function for binary classification problems. The new model is very flexible and capable of handling different types of data either symmetric or skew. The results of comparison with other extreme value distribution link functions in the previous section indicate that Inverse Weibull (TYPE II), Performed better than TYPE I (Complementary log log) and TYPE III(Weibull). In addition, the numerical procedure of the proposed link function is very easy to implement compared to other Extreme value distributions. Therefore, the performance of this proposed model is good and it can be used for

modeling binary classification problems.

References

- Harrison J. Bayesian Forecasting & Dynamic Models. 1999. Available from: <http://scholar.google.com/scholar?hl=en&btnG=Search&q=intitle:Bayesian+Forecasting+and+Dynamic+Models#1>
- Li T-H, Macdonald IL, Zucchini W. Hidden Markov and Other Models for Discrete- Valued Time Series. *J Am Stat Assoc.* 1998;93(444):1525.
- Caron R, Polpo A. Binary data regression: Weibull distribution. *AIP Conf Proc.* 2009;1193:187–193.
- Caron R, Sinha D, Dey DK, Polpo A. Categorical Data Analysis Using a Skewed Weibull Regression Model. 2018;1–17. <https://doi.org/10.3390/e20030176>.
- Almeida M, Blondell L, Peralta JM Jr, K JW Jr, Jun G, Teslovich TM, et al. Independent test assessment using the extreme value distribution theory. *BMC Proceed.* 2016;10(Suppl 7):5–9.
- Rinne H. *The Weibull Distribution.* Taylor & Francis Group, LLC. 2009.
- Fisher RA. The use of multiple measurements in taxonomic problems. *Ann Eugenics.* 1936;7(2):179-188.
- Taylor P, Chen M, Dey DK, Shao O. A New Skewed Link Model for Dichotomous Quantal Response Data. *J Am Stat Assoc.* 2013;37–41.
- Tahir MH, Cordeiro GM, Alzaatreh A, Mansoor M, Zubair M. The logistic-X family of distributions and its applications. *Commun Stat Hteory Methods.* 2016;45(24):7326-49.
- Berhe T, Modibia LM, Sahile AT, Tedla GW. Does quality of antenatal care influence antepartum stillbirth in Hossana City, South Ethiopia? *PLOS Glob Public Health.* 2023;3(1):e0001468.
- Orisakwe IC, Nwofor OK, Njoku CC, Ezedigboh UO. On the analysis of the changes in the temperatures over Abuja, Nigeria. *J Physic Sci Environ Stud.* 2017;3(1):8–17.
- Afulani PA. Determinants of stillbirths in Ghana: Does quality of antenatal care matter? *BMC Pregnancy Childbirth.* 2016;16(1):1–17.

Bootstrap Confidence Intervals for the Parameter of the Poisson-Sujatha Distribution and Their Applications to Agriculture

W. Panichkitkosolkul^{1*} and Ch. Ponkaew²

¹ Department of Mathematics and Statistics, Thammasat University, Pathumthani, 12120 Thailand

² Department of Mathematics, Faculty of Science and Technology, Phetchabun Rajabhat University, Phetchabun, 67000 Thailand

Received: 13 May 2023 / Revised: 3 July 2023 / Accepted: 10 July 2023

Abstract

In a number of real-world situations, one encounters count data with over-dispersion such that the typical Poisson distribution does not suit the data. In the current situation, it is appropriate to employ a combination of mixed Poisson and Poisson-Sujatha (PS) distributions. The PS distribution has been investigated for count data, which is of primary interest to a number of disciplines, including biology, medicine, demography, and agriculture. However, no research has been conducted regarding generating bootstrap confidence intervals for its parameter. The coverage probabilities and average lengths of bootstrap confidence intervals derived from the percentile, basic, and biased-corrected and accelerated bootstrap methods were compared using Monte Carlo simulation. The results indicated that it was impossible to achieve the nominal confidence level using bootstrap confidence intervals for tiny sample sizes, regardless of the other settings. Furthermore, when the sample size was large, there was not much of a difference in the performance of the several bootstrap confidence intervals. The bias-corrected and accelerated bootstrap confidence interval demonstrated superior performance compared to the other methods in all of the cases examined. Moreover, the effectiveness of the bootstrap confidence intervals was proven through their application to agricultural data sets. The calculations offer significant evidence in favor of the suggested bootstrap confidence intervals.

Keywords: Interval Estimation; Poisson Distribution; Mixed Distribution; Count Data; Bootstrap Method.

Introduction

The Poisson distribution is frequently used to model the number of events that occur in a given time and/or location (1). A Poisson distribution applies to data such

as the number of thunderstorms per month, the number of orders a company will receive the next day, the number of calls received per hour at a call centre, the number of defects in a completed product, etc. (2). The Poisson distribution is an essential model for the

* Corresponding author: Tel: +660868929579; Email: wararit@mathstat.sci.tu.ac.th

analysis of count data, but its use is limited due to the equality of its mean and variance (equi-dispersion). In comparison to the Poisson distribution, count data frequently exhibit over-dispersion, with a variance larger than the mean (3, 4). The application of the Poisson distribution to data with over-dispersion can result in inaccurate analyses and incorrect conclusions (5). A possible solution for addressing over-dispersion in count data is to employ a mixed Poisson distribution. This approach assumes that the Poisson parameter, which governs the distribution, is a random variable characterized by a single parameterized distribution (6).

Shanker (7) investigated the mathematical and statistical properties of the Poisson-Sujatha (PS) distribution developed by combining the Poisson and Sujatha distributions. The PS distribution is derived from the Poisson distribution when the Poisson parameter λ (the average number of occurrences) follows a Sujatha distribution. The PS distribution was found to be more appropriate than the Poisson and Poisson-Lindley (8) distributions when applied to two actual data sets.

Shanker (9) introduced the Sujatha distribution as a one-parameter lifetime continuous distribution with a probability density function (pdf) defined as

$$f(x; \theta) = \frac{\theta^3}{2 + \theta + \theta^2} (1 + x + x^2) \exp(-\theta x), \quad (1)$$

where $\theta > 0$ and $x > 0$. The Sujatha distribution is a continuous distribution that consists of a combination of three probability distributions: the exponential distribution, $\exp(-\theta)$, the gamma(2, θ) and the gamma(3, θ) distributions. These three distributions are weighted by their respective proportions $\frac{\theta^2}{2 + \theta + \theta^2}$, $\frac{\theta}{2 + \theta + \theta^2}$, and $\frac{2}{2 + \theta + \theta^2}$, respectively. The aforementioned distribution has been utilized for the purpose of modeling lifetime data within the domains of engineering and biomedical science. Moreover, Shanker (9) demonstrated that the Sujatha distribution outperforms the exponential, Lindley (10), and Akash (11) distributions as a more suitable model. Shanker (9) had examined the important statistical properties of the Sujatha distribution. Figure 1 depicts the pdf plots of the Sujatha distribution with specified values of parameter θ .

The confidence interval, a fundamental component of statistical inference, is a range of values that is highly probable to encompass the real value of the population parameter of interest. It serves as a crucial outcome in numerous statistical analyses and plays a pivotal role in the interpretation of parameter estimations (12). According to our best knowledge, no studies have been done on calculating the confidence interval for a PS distribution parameter. Bootstrap confidence intervals

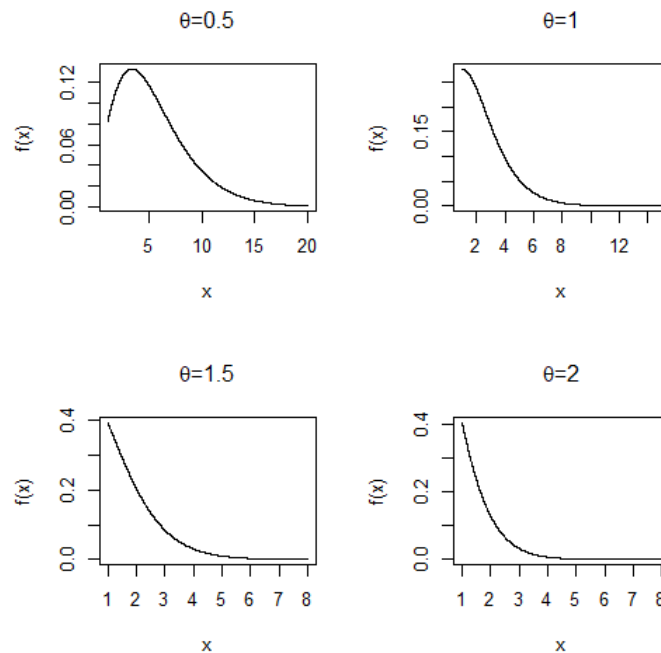


Figure 1. Plots of the pdf of the Sujatha distribution for $\theta = 0.5, 1, 1.5$ and 2

for estimating the parameter quantify the uncertainty associated with statistical inference based on the sample data. The idea is to conduct a simulation study using real data in order to estimate the potential size of sampling error (13). The key objective of the current study is to evaluate the effectiveness of three different bootstrap confidence interval estimations, specifically the percentile bootstrap (PB), the basic bootstrap (BB), and the bias-corrected and accelerated (BCa) bootstrap, in estimating the parameter of the PS distribution. In addition, none of the bootstrap confidence intervals will be exact (i.e., the actual confidence level is precisely equal to the nominal confidence level $1-\alpha$), but they will all be consistent, with the confidence level approaching $1-\alpha$ as the sample size increases (14). Given the inherent limitations in conducting a theoretical comparison of bootstrap confidence intervals, we select to perform a simulated study to assess their respective advantages and disadvantages. In addition, the bootstrap methods were compared in a simulation investigation in a number of studies (see Reiser et al. (15), Flowers-Cano et al. (16), Mostajeran et al. (17)). In the current study, a Monte Carlo simulation was implemented to compare their performance. Based on the chance of coverage and the average length, the simulation results were used to find the method with the best performance.

Theoretical Background

In probability theory, the Poisson distribution is characterized by its probability mass function (pmf), which may be written as

$$p(y; \lambda) = \frac{\exp(-\lambda)\lambda^y}{y!}, \tag{2}$$

where $y = 0, 1, 2, \dots$, e is a constant equal to approximately 2.718282 and λ is a Poisson parameter; $\lambda > 0$. Let X represent a random variable which follows the PS distribution with a parameter θ , which is commonly denoted as $X \sim \text{PS}(\theta)$. According to Shanker (7), the pmf of the PS distribution is defined as

$$p(x; \theta) = \frac{\theta^3}{2 + \theta + \theta^2} \frac{x^2 + (\theta + 4)x + (4 + 3\theta + \theta^2)}{(\theta + 1)^{x+3}}, \tag{3}$$

where $x = 0, 1, 2, \dots$, and $\theta > 0$. Figure 2 shows the pmf plots of the PS distribution for a range of parameter values θ . According to the PS distribution, the expected value (mean) and variance of the random variable X are as follows:

$$E(X) = \mu = \frac{6 + 2\theta + \theta^2}{\theta(2 + \theta + \theta^2)} \quad \text{and}$$

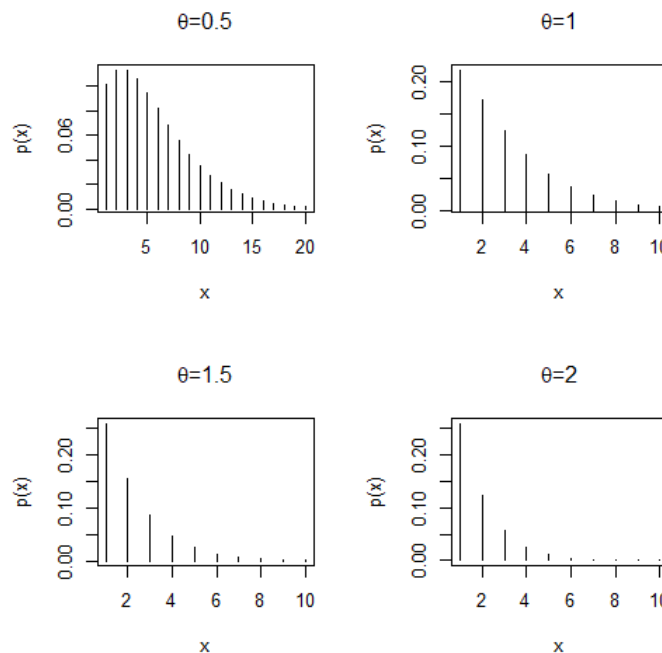


Figure 2. Plots of the pmf of the PS distribution for $\theta = 0.5, 1, 1.5$ and 2

$$Var(X) = \sigma^2 = \frac{12 + 24\theta + 28\theta^2 + 14\theta^3 + 4\theta^4 + \theta^5}{\theta^2(2 + \theta + \theta^2)^2}.$$

Maximizing the log-likelihood function $\log L(x_i; \theta)$ or the logarithm of the joint pmf of X_1, \dots, X_n yields the point estimator of θ . Consequently, the derivation of the ML estimator for θ involves the following procedures:

$$\frac{\partial}{\partial \theta} \log L(x_i; \theta) = \frac{\partial}{\partial \theta} \left[n \log \left(\frac{\theta^3}{2 + \theta + \theta^2} \right) - \sum_{i=1}^n (x_i + 3) \log(\theta + 1) + \sum_{i=1}^n \log [x_i^2 + (\theta + 4)x_i + (4 + 3\theta + \theta^2)] \right]$$

$$= \frac{n(6 + 2\theta + \theta^2)}{\theta(2 + \theta + \theta^2)} - \frac{n(\bar{x} + 3)}{\theta + 1} + \sum_{i=1}^n \frac{x_i + (2\theta + 3)}{[x_i^2 + (\theta + 4)x_i + (4 + 3\theta + \theta^2)]}$$

We obtain the non-linear equation by solving for θ

in the equation $\frac{\partial}{\partial \theta} \log L(x_i; \theta) = 0$:

$$\frac{n(6 + 2\theta + \theta^2)}{\theta(2 + \theta + \theta^2)} - \frac{n(\bar{x} + 3)}{\theta + 1} + \sum_{i=1}^n \frac{x_i + (2\theta + 3)}{[x_i^2 + (\theta + 4)x_i + (4 + 3\theta + \theta^2)]} = 0,$$

$$\bar{x} = n^{-1} \sum_{i=1}^n x_i$$

where \bar{x} denotes the sample mean. According to the inability to find a closed-form solution provided by the ML estimator for θ , numerical iteration techniques such as bisection, Newton-Raphson, and Ragula-Falsi methods can be used to solve the resulting non-linear problem. The paper utilized the maxLik package (18) with the Newton-Raphson method for ML estimation. The statistical software R (19) was employed for this purpose.

Bootstrap Confidence Intervals

The interval estimation, also known as confidence interval, is derived from an estimator that calculates the standard errors of a parameter, denoted as ϕ . Then, the standard error is multiplied by the critical value to add or subtract, giving the $(1 - \alpha)100\%$ two-sided confidence interval for ϕ (for example, $\hat{\phi} \pm z_{1-(\alpha/2)} SE(\hat{\phi})$). This computation is based on the normality assumption of the estimator of ϕ (16). Nevertheless, there are a number of situations in which the normality assumption is not appropriate to make an estimation. In such instances, or when estimating the standard error is exceedingly challenging, it is

reasonable to employ techniques based on the bootstrap method. The computationally intensive bootstrap methods described in this study offer an alternative to assuming the underlying distribution when constructing approximate confidence intervals (20). In this paper, we concentrate on the three bootstrap confidence intervals for the PS distribution parameter. The most frequently employed bootstrap confidence intervals in practice are the PB, BB, and BCa confidence intervals (14). With the use of the boot package (21) and the statistical software R (19), the bootstrap confidence intervals were calculated for this investigation.

Percentile Bootstrap (PB) Confidence Interval

The PB two-sided confidence interval is defined as the range bounded by the $(\alpha/2) \times 100$ and $(1 - (\alpha/2)) \times 100$ percentiles of the distribution for the estimated values of θ acquired from resampling or the distribution of $\hat{\theta}^*$, where θ denotes an important parameter and α denotes the level of significance (22). The procedure for constructing a PB confidence interval for the PS distribution parameter is as follows:

- 1) With a replacement, B random bootstrap samples of the underlying distribution are created, where B is the number of bootstrap replications,
- 2) From each bootstrap sample, a parameter estimate $\hat{\theta}^*$ is determined,
- 3) All parameter estimates from the B bootstrap samples are ranked from smallest to greatest, and
- 4) the $(1 - \alpha)100\%$ PB two-sided confidence interval is created as follows:

$$CI_{PB} = [\hat{\theta}_{(r)}^*, \hat{\theta}_{(s)}^*], \tag{4}$$

where the notation $\hat{\theta}_{(r)}^*$ is the r^{th} quantile of a collection of the parameter estimate $\hat{\theta}^*$ arranged in ascending order, while $\hat{\theta}_{(s)}^*$ is the s^{th} quantile of the aforementioned collection, $r = \lceil (\alpha/2)B \rceil$, $s = \lceil (1 - (\alpha/2))B \rceil$, where $\lceil x \rceil$ stands for the ceiling function of x , and α is the significance level. This study utilized $\alpha = 0.05$ and $B = 2,000$; the two quantiles related to the lower and upper bounds of the PB two-sided confidence interval were $\hat{\theta}_{(r)}^* = \hat{\theta}_{(50)}^*$ (the 50th quantile) and $\hat{\theta}_{(s)}^* = \hat{\theta}_{(1950)}^*$ (the 1950th quantile).

Basic Bootstrap (BB) Confidence Interval

The BB method, often known as the simple bootstrap method, is just as straightforward to implement as the PB method. Consider the quantity of interest to be θ and the estimator of θ to be $\hat{\theta}$. The BB technique presumes that $\hat{\theta} - \theta$ and $\hat{\theta}^* - \hat{\theta}$ follow similar distributions (20). The $(1 - \alpha)100\%$ BB two-sided confidence interval for θ is

$$CI_{BB} = [2\hat{\theta} - \hat{\theta}_{(s)}^*, 2\hat{\theta} - \hat{\theta}_{(r)}^*], \tag{5}$$

where the quantiles $\hat{\theta}_{(r)}^*$ and $\hat{\theta}_{(s)}^*$ represent the same percentile of the empirical distribution of bootstrap estimates $\hat{\theta}^*$ that are utilized in (4) to calculate the PB confidence interval.

Bias-Corrected and Accelerated (BCa) Bootstrap Confidence Interval

The calculation of BCa bootstrap confidence intervals commonly involves the utilization of influence statistics derived from jackknife simulations. However, incorporating jackknife simulation alongside ordinary bootstrapping is computationally expensive for the intended purposes. The BCa bootstrap confidence interval uses a bias-correction element and an acceleration element to correct for the bias and skewness of the bootstrap parameter estimates, mitigating the over-coverage problems seen with the PB confidence interval (22, 23, 24). Davison and Hinkley (25) and Chernick and LaBudde (14) described the mathematical particulars of the BCa adjustment. The bias-correction element \hat{z}_0 is calculated by

$$\hat{z}_0 = \Phi^{-1} \left(\frac{\#\{\hat{\theta}^* \leq \hat{\theta}\}}{B} \right),$$

where Φ^{-1} is the inverse function of the standard normal distribution's cumulative distribution function. The acceleration element \hat{a} is calculated via jackknife resampling, which entails generating n replicates of the initial set of data, where n is the sample sizes. The initial jackknife replication is obtained by omitting the first case ($i = 1$) from the initial sample, the second by omitting the second case ($i = 2$), etc., until a total of n samples, each with a size of $n - 1$, are generated. Based on the jackknife resamples, we obtain the value

of $\hat{\theta}_{(-i)}$. The acceleration factor \hat{a} is given by

$$\hat{a} = \frac{\sum_{i=1}^n (\hat{\theta}_{(\cdot)} - \hat{\theta}_{(-i)})^3}{6 \left\{ \sum_{i=1}^n (\hat{\theta}_{(\cdot)} - \hat{\theta}_{(-i)})^2 \right\}^{3/2}},$$

where $\hat{\theta}_{(\cdot)} = \sum_{i=1}^n \hat{\theta}_{(-i)} / n$. The computation of the

values of α_1 and α_2 are as follows:

$$\alpha_1 = \Phi \left\{ \hat{z}_0 + \frac{\hat{z}_0 + z_{\alpha/2}}{1 - \hat{a}(\hat{z}_0 + z_{\alpha/2})} \right\} \quad \text{and}$$

$$\alpha_2 = \Phi \left\{ \hat{z}_0 + \frac{\hat{z}_0 + z_{1-\alpha/2}}{1 - \hat{a}(\hat{z}_0 + z_{1-\alpha/2})} \right\},$$

where $z_{\alpha/2}$ is the $\alpha / 2$ quantile of the normal distribution with a mean of zero and standard deviation of 1. Then, the $(1 - \alpha)100\%$ BCa bootstrap two-sided confidence interval for the PS distribution parameter is computed by

$$CI_{BCa} = [\hat{\theta}_{(j)}^*, \hat{\theta}_{(k)}^*], \tag{6}$$

where $j = \lceil \alpha_1 B \rceil$ and $k = \lceil \alpha_2 B \rceil$. When the value \hat{z}_0 is set to 0 and \hat{a} is also set to 0, it can be observed that the BCa confidence interval is equal to the PB confidence interval.

Simulation Study

In the current study, the interval estimation for the parameter of the PS distribution was estimated using three bootstrap two-sided confidence intervals. Due to the lack of a direct theoretical comparison, a Monte Carlo simulation investigation was conducted using R (19) version 4.3.1 to include cases with various sample sizes ($n = 10, 30, 50, 100,$ and 500). To observe the effects of both large and small variances, the actual value of the parameter (θ) was chosen from 0.1, 0.5, 0.8, 1 and 1.5. Because Ukoumunne et al. (26) asserted that 2,000 bootstrap samples are enough to estimate the coverage probability for the 95% confidence intervals with a standard error of slightly under 0.5%, the number of bootstrap replications (B) was fixed at 2,000. From the initial pseudo-random sample, n -sized bootstrap samples were generated, and each simulation was repeated 1,000 times. Without sacrificing generality, the level of confidence $(1 - \alpha)$ was set at 0.95. The study

Table 1. Coverage probability and the average length of the 95 %bootstrap confidence intervals for θ of the PS distribution

n	θ	Coverage probability			Average length		
		PB	BB	BCa	PB	BB	BCa
10	0.1	0.894	0.889	0.886	0.0773	0.0773	0.0748
	0.5	0.872	0.862	0.882	0.4663	0.4666	0.4465
	0.8	0.894	0.893	0.903	0.8957	0.8998	0.8367
	1.0	0.914	0.882	0.915	1.2677	1.2641	1.1743
	1.5	0.893	0.883	0.893	2.8157	2.8582	2.4965
30	0.1	0.937	0.912	0.940	0.0433	0.0432	0.0425
	0.5	0.912	0.906	0.915	0.2529	0.2529	0.2474
	0.8	0.908	0.913	0.911	0.4397	0.4397	0.4273
	1.0	0.931	0.939	0.936	0.5904	0.5898	0.5702
	1.5	0.928	0.928	0.940	1.0862	1.0867	1.0256
50	0.1	0.947	0.933	0.948	0.0330	0.0331	0.0327
	0.5	0.942	0.935	0.942	0.1921	0.1924	0.1898
	0.8	0.929	0.931	0.932	0.3350	0.3351	0.3293
	1.0	0.937	0.934	0.947	0.4461	0.4465	0.4371
	1.5	0.935	0.924	0.939	0.7818	0.7812	0.7559
100	0.1	0.943	0.936	0.946	0.0237	0.0237	0.0236
	0.5	0.948	0.932	0.943	0.1343	0.1340	0.1332
	0.8	0.939	0.945	0.942	0.2346	0.2345	0.2324
	1.0	0.956	0.950	0.953	0.3082	0.3081	0.3051
	1.5	0.928	0.953	0.934	0.5359	0.5358	0.5279
500	0.1	0.941	0.948	0.943	0.0106	0.0106	0.0106
	0.5	0.948	0.948	0.946	0.0603	0.0603	0.0601
	0.8	0.953	0.949	0.951	0.1037	0.1037	0.1035
	1.0	0.949	0.949	0.946	0.1365	0.1365	0.1360
	1.5	0.961	0.945	0.958	0.2331	0.2331	0.2322

evaluated the performance of different bootstrap two-sided confidence intervals by examining their coverage probabilities and average lengths. The ideal confidence interval should have a coverage probability that is equal to or very close to the nominal confidence level, indicating that it contains the real parameter. Additionally, the proposed confidence interval with the shortest average length is preferred as it provides the most accurate estimation for the parameter of interest in a given scenario. Therefore, it is evident that in cases where the coverage probability is equal, a smaller average length signifies the suitability of the bootstrap confidence interval for that specific situation.

The study’s findings are presented in Table 1. For the given value of $n=10$, the coverage probabilities of all three bootstrap confidence intervals exhibited a tendency to be below 0.90, indicating that they did not achieve the intended nominal confidence level. In these situations, however, the BCa bootstrap two-sided confidence interval outperformed the others. For a sample size of 30, we again find that no bootstrap confidence interval yields a probability of coverage in excess of the nominal confidence level of 0.95. For $n \geq 50$, each bootstrap confidence interval achieved coverage probabilities close to the nominal level of confidence and had average lengths that were

comparable. Nevertheless, the BCa bootstrap confidence interval exhibited a coverage probability that was more closely aligned with the specified nominal confidence level of 0.95. The coverage probabilities tended to rise along with the sample size, approaching the nominal confidence level of 0.95 as the sample size grew larger. Due to the relationship between variance and θ , the average lengths of the bootstrap confidence intervals increased as the value of θ was increased. Consequently, as the sample size increased, the average lengths of all three bootstrap two-sided confidence intervals decreased, with the BCa bootstrap confidence interval having the shortest average length for all situations examined. Furthermore, when the sample size was small ($n=10$), there was a statistically significant difference in the average length of the BCa bootstrap confidence interval compared to the others. It was observed that the PB and BB confidence intervals for the average length did not differ significantly across sample sizes. In brief, the BCa bootstrap two-sided confidence interval demonstrates superior performance in terms of estimated coverage probability and average length when applied to moderate and large sample sizes ($n \geq 50$).

Applications to Real-World Data

In this section, we demonstrate the applicability of bootstrap confidence intervals for estimating the PS distribution parameter using two real-world data sets.

Application to the Number of Red Mites

This example utilizes the number of red mites in a apple farm collected by Bliss and Fisher (27). Table 2 presents the dataset comprising 150 observations. The sample mean and standard deviation for this data set are 1.1500 and 1.4504, respectively. This study employs the chi-squared goodness-of-fit test to determine if the sample data are likely to be representative of a particular theoretical distribution (28). The chi-square statistic was 3.3889, while the p-value was 0.4950.

Consequently, a PS distribution with $\hat{\theta} = 1.6533$ is appropriate for this data set. Table 3 displays the 95% bootstrap confidence intervals for the PS distribution parameter. The results are consistent with those of the simulation because the average lengths of the BCa bootstrap confidence interval were shorter than those of the PB and BB intervals.

Application to the Number of Corn Borer Larvae Per Plant

McGuire et al. (29) recorded the number of corn borer larvae per plant in the field corn of Northwest Iowa, United States. Table 4 provides the dataset, with a

total sample size of 324. The sample mean and standard deviation for this data set are 0.6481 and 0.9208, respectively. The chi-squared statistic for the chi-squared goodness-of-fit test (28) was 1.1743 and the p-value was 0.5559. Therefore, the data best fits a PS distribution with $\hat{\theta} = 2.4717$. Table 5 shows the 95% bootstrap confidence intervals for the PS distribution parameter. Because the average lengths of the BCa bootstrap confidence interval were shorter than those of the PB and BB confidence intervals, the results were consistent with the simulation results.

Results and Discussion

For estimating the parameter of the Poisson-Sujatha distribution, the percentile bootstrap (PB), the basic bootstrap (BB), and the bias-corrected and accelerated (BCa) bootstrap methods were proposed. When the sample sizes were relatively small ($n = 10$ and 30), the coverage probabilities for all three bootstrap confidence intervals were significantly below the desired threshold of 0.95. When the sample size was large enough ($n \geq 50$), the coverage probabilities and average lengths derived from the three bootstrap confidence intervals did not differ significantly. According to the results of our research, the BCa bootstrap confidence interval was the best for virtually all of the scenarios, both in the

Table 2 .The number of red mites on apple leaves

Number of red mites	0	1	2	3	4	≥ 5
Observed frequency	70	38	17	10	9	6
Expected frequency	66.4433	39.2898	21.7920	11.4538	5.7674	5.2537

Table 3 .The 95 %bootstrap two-sided confidence intervals and corresponding widths using all intervals for the parameter in the number of red mites

Methods	Confidence intervals	Widths
PB)1.4312, 1.9408(0.5096
BB	(1.3598, 1.8787)	0.5189
BCa	(1.4168, 1.9179)	0.5011

Table 4 .The number of corn borer larvae per plant

Number of corn borer larvae	0	1	2	≥ 3
Observed frequency	188	83	36	17
Expected frequency	193.6521	79.5626	31.6015	19.1838

Table 5 .The 95 %bootstrap two-sided confidence intervals and corresponding widths using all intervals for the parameter in the number of corn borer larvae per plant

Methods	Confidence intervals	Widths
PB	(2.2174, 2.7980)	0.5806
BB	(2.1590, 2.7292)	0.5702
BCa	(2.1903, 2.7586)	0.5683

simulation study and while utilizing real data sets. Our findings provided simulation results that correspond to Flowers-Cano et al.'s (16) research work. Using a Monte Carlo Simulation, they compared the coverage of several bootstrap confidence intervals. According to their findings, the coverage probabilities of the BCa bootstrap confidence interval were frequently greater than those of the other confidence intervals.

This study's limitation is that none of the bootstrap confidence intervals were exact, but they were consistent, indicating that the probability of coverage approaches 0.95 as sample sizes increase. In addition, the computation of three bootstrap confidence intervals is difficult and computationally intensive.

However, there are a number of R packages available for computing bootstrap confidence intervals, including the boot package (21), the bootstrap package (30), the semEff package (31), and the BootES package (32). Since R is an open-source programming language, users are allowed to install these packages. Future research could concentrate on the development of confidence intervals for parameter functions, such as the population mean, dispersion index, and coefficient of variation. Additionally, it is important to note that there is currently a lack of research available on the topic of hypothesis testing for the parameter of the PS distribution. The study of these issues can be explored in future research.

References

- Andrew FS, Michael RW. Practical business statistics. 8th ed. San Diego: Academic Press; 2022.
- Siegel AF. Practical business statistics. 7th ed. London: Academic Press; 2017.
- Hougaard P, Lee M-LT, Whitmore GA. Analysis of overdispersed count data by mixtures of Poisson variables and Poisson processes. *Biometrics*. 1997;53(4):1225-1238.
- Ong S-H, Low Y-C, Toh K-K. Recent developments in mixed Poisson distributions. *ASM Sci J*. 2021.
- McElduff F.C. Models for discrete epidemiological and clinical data [PhD Thesis]. London: University College London; 2012.
- Tharshan R, Wijekoon P. A new mixed Poisson distribution for over-dispersed count data: theory and applications. *Reliab: Theory Appl*. 2022;17(1):33-51.
- Shanker R. On Poisson-Sujatha distribution and its applications to model count data from biological sciences. *Biom Biostat Int J*. 2016;3(4):1-8.
- Sankaran M. The discrete Poisson-Lindley distribution. *Biometrics*. 1970;1926(1):145-149.
- Shanker R. Sujatha distribution and its applications. *Stat Transit New Series*. 2016;17(3):391-410.
- Lindley DV. Fiducial distributions and Bayes' theorem. *J R Stat Soc Series B*. 1958;20(1):102-107.
- Shanker R. Akash distribution and its applications. *Int J Prob Stat*. 2015;4(3):65-75.
- Tan SH, Tan SB. The correct interpretation of confidence intervals. *Proc Singapore Healthc*. 2010;19(3):276-278.
- Wood M. Statistical inference using bootstrap confidence intervals. *Signif*. 2004;1(4):180-182.
- Chernick MR, LaBudde RA. An introduction to bootstrap methods to R. 1st ed. Singapore: John Wiley & Sons; 2011.
- Reiser M, Yao L, Wang X, Wilcox J, Gray S. A Comparison of bootstrap confidence intervals for multi-level longitudinal data using Monte-Carlo simulation. In: Chen DG, Chen J. (eds) Monte-Carlo simulation-based statistical modeling. Springer; 2017.
- Flowers-Cano RS, Ortiz-Gómez R, León-Jiménez JE, Rivera RL, Cruz LAP. Comparison of bootstrap confidence intervals using Monte Carlo simulations. *Water*. 2018;10(2).
- Mostajeran A, Iranpanah N, Noorossana R. A new bootstrap based algorithm for Hotelling's T2 multivariate control chart. *J Sci I R I*. 2016;27(3):269-278.
- Henningsen A, Toomet O. maxLik: a package for maximum likelihood estimation in R. *Comput Stat*. 2011;26(3):443-458.
- Ihaka R, Gentleman R. R: a language for data analysis and graphics. *J Comput Graph Stat*. 1996;5(3):299-314.
- Meeker WQ, Hahn GJ, Escobar LA. Statistical intervals: a guide for practitioners and researchers. 2nd ed. New Jersey: John Wiley and Sons; 2017.
- Canty A, Ripley B. boot: bootstrap R (S-Plus) functions. R package version 1.3-28.1, 2022.
- Efron B. The jackknife, the bootstrap, and other resampling plans, in CBMS-NSF regional conference series in applied mathematics, Philadelphia: SIAM; 1982.
- Efron B, Tibshirani RJ. An introduction to the bootstrap. 1st ed. New York: Chapman and Hall; 1993.
- Efron B. Better bootstrap confidence intervals. *J Am Stat Assoc*. 1987;82(297):171-185.
- Davison AC, Hinkley DV. Bootstrap methods and their application. 1st ed. Cambridge: Cambridge University Press; 1997.
- Ukoununne OC, Davison AC, Gulliford MC, Chinn S. Non-parametric bootstrap confidence intervals for the intraclass correlation coefficient. *Stat Med*. 2003;22(24):3805-3821.
- Bliss CI, Fisher RA. Fitting the negative binomial distribution to biological data. *Biometrics*. 1953;9(2):176-200.
- Turhan NS. Karl Pearson's chi-square tests. *Educ Res Rev*. 2020;15(9):575-580.
- McGuire JU, Brindley TA, Bancroft TA. The distribution of european corn borer larvae *pyrausta nubilalis* (Hbn.), in field corn. *Biometrics*. 1957;13(1):65-78.
- Kostyshak S. bootstrap: functions for the book "An introduction to the bootstrap". R package version, 2019.6, 2022.
- Murphy MV. semEff: automatic calculation of effects for piecewise structural equation models. R package version 0.6.1, 2022.
- Kirby KN, Gerlanc D. BootES: an R package for bootstrap confidence intervals on effect sizes. *Behav Res Methods*. 2013;45(4):905-927.

Qutrit Teleportation and Entanglement Evolved by the One-Axis Counter-Twisting Hamiltonian under the Intrinsic Decoherence

A. Naji*

Department of Physics, Faculty of Sciences, Shahid Chamran University of Ahvaz, Ahvaz, Islamic Republic of Iran

Received: 24 Dec 2022 / Revised: 4 Apr 2023 / Accepted: 10 June 2023

Abstract

In this paper, we study the entanglement and quantum teleportation of a two-qutrit state evolved under one-axis counter-twisting Hamiltonian with the intrinsic decoherence effects. The entanglement and fidelity are analyzed as a function of decoherence rate, Hamiltonian coefficient, and magnetic field. It has been seen that the system is constantly entangled. Both the decoherence rate and the Hamiltonian coefficient have a negative correlation with the entanglement and fidelity. The faithfulness and negativity are efficiently optimized by the magnetic fields. We deduced that we can acquire some best fidelity for the system when it is maximally entangled.

Keywords Entanglement; Teleportation; Intrinsic decoherence; One-axis counter-twisting Hamiltonian.

Introduction

The quantum entanglement is a fundamental concept in many quantum information processes, such as quantum teleportation, dense coding, quantum communication and quantum cryptography (1-6). Much attentions was paid to the one-axis counter-twisting Hamiltonian because of creating entanglement and quantum correlations used in spin systems (7-9).

The one-axis counter-twisting Hamiltonian have experiment realization in Bose-Einstein condensate(10), and optical lattice (11). Recently, spin chains were used in quantum teleportation (12-14). Due to their superior capacity and security than qubit states, qutrits, or three level atoms, are employed for quantum teleportation (15). On the other hand, many approaches have been used to address the consequences of noises or decoherences in the real world (16). Milburn for the intrinsic decoherence proposed a scheme to modify the ordinary Schrodinger equation (17-19). The spin chains as the channel for teleportation under decoherence

change from pure state to mixed states, and it affects the fidelity (20). The effect of intrinsic decoherence on entanglement dynamics and quantum teleportation was studied in several works (21-24).

This study aims to investigate the time evolution of entanglement for two-qutrit state under one-axis counter-twisting (OAT) Hamiltonian (7) with intrinsic decoherence effects (17), and the teleportation via this channel. The paper is set up as follows. Section 1 introduces the system's Hamiltonian in the presence and absence of a magnetic field and obtains the density matrix of the system with intrinsic decoherence. We examine the quantum system's entanglement in section 2. We examine the teleportation via this channel in section 3. Finally, section 5 is devoted to discussion.

Materials and Methods

1. The Hamiltonian of the system

Kitagawa and Ueda introduced two nonlinear interaction so called one-axis, and two-axes counter-twisting Hamiltonian to generate correlations and spin

* Corresponding author: Tel: +989166125496; Email: a.naji@scu.ac.ir

squeezing (7). We consider the interaction of two three-level atoms by OAT Hamiltonian. This Hamiltonian for the system is given by:

$$H = \chi J_x^2 \tag{1}$$

where $J_x = \sum_{i=1}^N J_{ix}$ is the x component of the collective angular momentum for spin 1.

Moreover, we study OAT interaction in the presence of magnetic fields with the other Hamiltonian is written as

$$H_1 = \chi J_x^2 + B J_z \tag{2}$$

where B is the magnetic field in the Z direction and χ is Hamiltonian coefficient.

The master equation describing the intrinsic decoherence under Markovian approximations is given by (17):

$$\frac{d\rho(t)}{dt} = -i[H, \rho(t)] - \frac{\Gamma}{2}[H, [H, \rho(t)]] \tag{3}$$

where Γ is the intrinsic decoherence rate. The formal solution of above master equation can be expressed as (19):

$$\rho(t) = \sum_{k=0}^{\infty} \frac{(\Gamma t)^k}{k!} M^k \rho(0) M^{\dagger k} \tag{4}$$

where $\rho(0)$ is the density operator of the initial state and M^k is defined by:

$$M^k = H^k e^{-iHt} e^{-\frac{\Gamma t}{2} H^2} \tag{5}$$

Based on Eq (4), it is easy to show that under intrinsic decoherence, the dynamics of the density operator for above-mentioned system which is initially in the state $\rho(0)$ is given by (25):

$$\hat{\rho}(t) = \sum_{m,n} \exp\left[\frac{-\Gamma}{2}(E_m - E_n)^2 - i(E_m - E_n)t\right] \times \langle \psi_m | \hat{\rho}(0) | \psi_n \rangle | \psi_m \rangle \langle \psi_n | \tag{6}$$

where the system is initially in the state $\rho(0)$; E_i ($i = m, n$) and ψ_i ($i = m, n$) are eigenvalues, and corresponding eigenvectors of \hat{H} respectively.

A qutrit system is described by the basis $|0\rangle = \begin{pmatrix} 1 \\ 0 \\ 0 \end{pmatrix}$,

$$|1\rangle = \begin{pmatrix} 0 \\ 1 \\ 0 \end{pmatrix}, |2\rangle = \begin{pmatrix} 0 \\ 0 \\ 1 \end{pmatrix} \text{ in three dimensional Hilbert space.}$$

We assume that two-qutrit system is initially prepared at

one qutrit is in $|1\rangle$ state and the other qutrit is in $|0\rangle$ state as the follows:

$$|\psi_0\rangle = |1\rangle \otimes |0\rangle \tag{7}$$

Therefore, $\rho(0)$ can be written as:

$$\rho_0 = |1,0\rangle\langle 1,0| = \begin{pmatrix} 0 & 0 & 0 & 0 & 0 & 0 & 0 & 0 & 0 \\ 0 & 1 & 0 & 0 & 0 & 0 & 0 & 0 & 0 \\ 0 & 0 & 0 & 0 & 0 & 0 & 0 & 0 & 0 \\ 0 & 0 & 0 & 0 & 0 & 0 & 0 & 0 & 0 \\ 0 & 0 & 0 & 0 & 0 & 0 & 0 & 0 & 0 \\ 0 & 0 & 0 & 0 & 0 & 0 & 0 & 0 & 0 \\ 0 & 0 & 0 & 0 & 0 & 0 & 0 & 0 & 0 \\ 0 & 0 & 0 & 0 & 0 & 0 & 0 & 0 & 0 \\ 0 & 0 & 0 & 0 & 0 & 0 & 0 & 0 & 0 \end{pmatrix} \tag{8}$$

The Hamiltonian (1) can be written in the following matrix form:

$$H = -\hbar \begin{pmatrix} \frac{\chi}{2} & 0 & \frac{\chi}{4} & 0 & \frac{\chi}{2} & 0 & \frac{\chi}{4} & 0 & 0 \\ 0 & \frac{3\chi}{4} & 0 & \frac{\chi}{2} & 0 & \frac{\chi}{2} & 0 & \frac{\chi}{4} & 0 \\ \frac{\chi}{4} & 0 & \frac{\chi}{2} & 0 & \frac{\chi}{2} & 0 & 0 & 0 & \frac{\chi}{4} \\ 0 & \frac{\chi}{2} & 0 & \frac{3\chi}{4} & 0 & \frac{\chi}{4} & 0 & \frac{\chi}{2} & 0 \\ \frac{\chi}{2} & 0 & \frac{\chi}{2} & 0 & \chi & 0 & \frac{\chi}{2} & 0 & \frac{\chi}{2} \\ 0 & \frac{\chi}{2} & 0 & \frac{\chi}{4} & 0 & \frac{3\chi}{4} & 0 & \frac{\chi}{2} & 0 \\ \frac{\chi}{4} & 0 & 0 & 0 & \frac{\chi}{2} & 0 & \frac{\chi}{2} & 0 & \frac{\chi}{4} \\ 0 & \frac{\chi}{4} & 0 & \frac{\chi}{2} & 0 & \frac{\chi}{2} & 0 & \frac{3\chi}{4} & 0 \\ 0 & 0 & \frac{\chi}{4} & 0 & \frac{\chi}{2} & 0 & \frac{\chi}{4} & 0 & \frac{\chi}{2} \end{pmatrix} \tag{9}$$

where the basis is $\{|0,0\rangle, |0,1\rangle, |0,2\rangle, |1,0\rangle, |1,1\rangle, |1,2\rangle, |2,0\rangle, |2,1\rangle, |2,2\rangle\}$, and Hamiltonian affect these states as in the following:

Using Eq. (9) and Eq. (8) and Eq. (6), we can obtain $\rho(t)$ of the whole system. This matrix is too complicated to be given here.

2. Entanglement of the system

Negativity is a straightforward, calculable metric. Vidal et al. have demonstrated that negativity is an entanglement monotone and a suitable entanglement measure (26). It is also demonstrated that the negativity can be measured experimentally using a quantum circuit devoid of noise (27). The negativity $N(\rho)$ for an arbitrary bipartite system is defined as in the following (26):

$$N(\rho) = \frac{\|\rho^{T_A}\| - 1}{2} \quad (10)$$

where $\|\rho^{T_A}\| = \text{Tr} \sqrt{(\rho^{T_A})^\dagger \rho^{T_A}}$ denotes the trace norm of ρ^{T_A} . The ρ^{T_A} is the partial transpose ρ with respect to the subsystem A. The negativity $N(\rho)$ is

equivalent to the absolute value of the sum of negative eigenvalues of ρ^{T_A} .

To discuss the entanglement dynamics in the system discussed in section 2, we can calculate the negativity by Eqs. (6) and (10). We have presented the negativity of two atoms as a function of time for various Γ in Figure 1. The plot shows that the entanglement

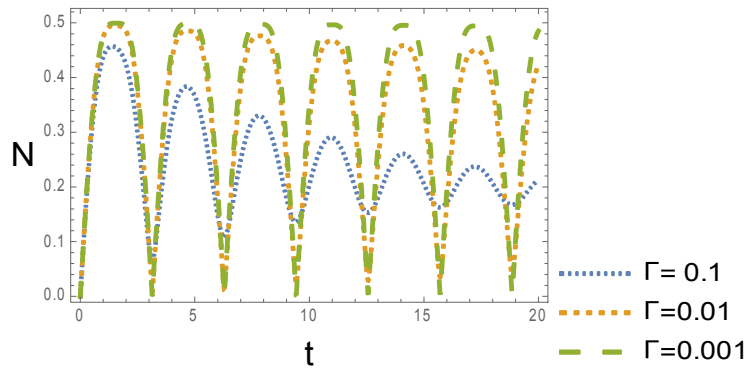


Figure 1. Negativity as a function of time for various values of Γ assuming $\chi = 1$.

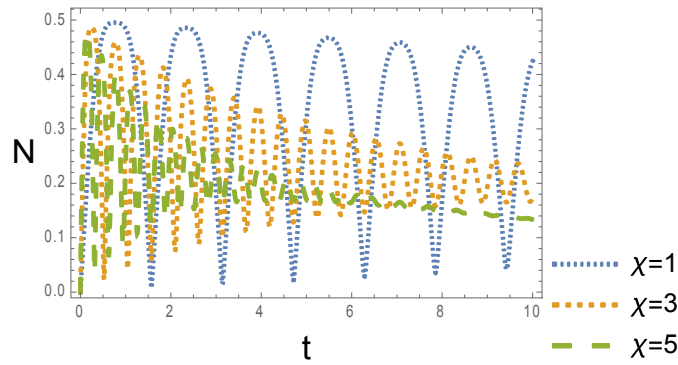


Figure 2. Negativity as a function of time for various values χ and assuming $\Gamma=0.01$.

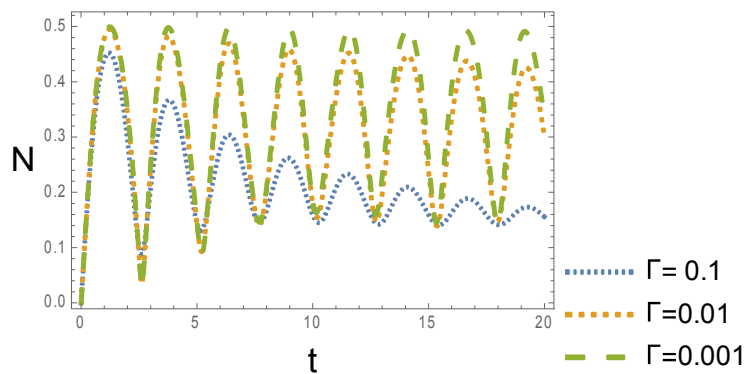


Figure 3. Negativity as a function of time for various values of Γ for $\chi = 1$, $B=1$.

evolves periodically with decreasing amplitude by passing time. It is observed that the amplitude of entanglement is a decreasing function of Γ but its frequency is an independent function of Γ . In Figure 2, we showed the time evolution of negativity for different values χ . It is deduced that the negativity is a decreasing function of χ . Moreover, for given values of χ the entanglement is initially an oscillating function of time, but it tends to be a constant value with the passage of time. Also, the frequency is an increasing function of χ and the amplitude is a decreasing function of χ . So, negativity goes to the constant more rapidly for higher values of χ

We examine the effects of the magnetic field on the system using the Hamiltonian H_1 . In Figure 3, the negativity was plotted as a function of Γ and t for Hamiltonian H_1 . It is observed that the negativity is decreased with the increase of Γ . Besides, the entanglement is an oscillating function of time for small value of Γ . In the comparison with Figure 1, It is found that the magnetic field optimize the entanglement in the average.

In Figure 4, we have presented the negativity as a function of time and different values of B assuming $\Gamma=0.01$. In the comparison with Figure 2, It is observed that the amplitude of the entanglement is increasing function of B . On the other hand, the frequency of entanglement is decreasing function of magnetic fields and over time the negativity tends to be a constant value.

3. Teleportation

Bose (28) investigates teleportation utilizing spin

chains. According to this standard teleportation, Alice placed her qutrit in the i 'th position of a spin chain, while Bob placed his qutrit in the j 'th position. Then, Alice will use this entangled spin chain as Bob's channel to transmit an unknown state. After some operations on qutrit 1 and 3, Alice measures the two qutrits in her possession, and then sends this information to Bob. Depending on Alice's classical message, Bob performs some unitary operations on his half of the EPR pair and he can inform of the original state.

Alice is initially given the pure state $\rho_{in} = |\psi_{in}\rangle\langle\psi_{in}|$, where $|\psi_{in}\rangle = \frac{1}{\sqrt{3}}(|0\rangle + |1\rangle + |2\rangle)$.

$$\rho_{in} = \frac{1}{3} \begin{pmatrix} 1 & 1 & 1 \\ 1 & 1 & 1 \\ 1 & 1 & 1 \end{pmatrix} \tag{11}$$

The aim of Alice is to send this state eq (11) via the channel with the density matrix in equation (6). The output state is given by (28)

$$\rho_{out} = \sum_{j=0}^8 Tr[E^j \rho(t)] \{ \Gamma^j \rho_{in} \Gamma^j \} \tag{12}$$

where Γ^j ($j = 1, \dots, 8$) refers to Gell-Mann matrices and Γ^0 is the identity matrix for qutrits systems. Also, E^j 's are the density matrices of maximum entangled qutrit states as $\phi^0 = (1/\sqrt{3})(|2,0\rangle + |1,1\rangle + |0,2\rangle)$, $\phi^1 = (1/\sqrt{3})(|1,0\rangle + |0,1\rangle + |2,2\rangle)$, $\phi^2 = (1/\sqrt{3})(|0,0\rangle + |2,1\rangle + |1,2\rangle)$,

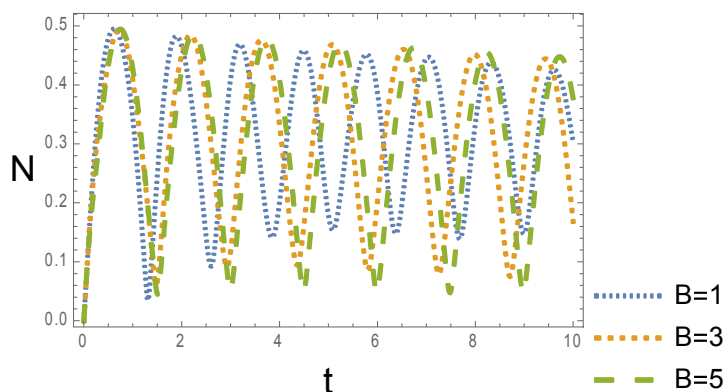


Figure 2. Negativity as a function of time for various values B assuming $\Gamma=0.01$.

$$\phi^3 = (1/\sqrt{3}) \left(|2,0\rangle + e^{\frac{2\pi i}{3}} |1,1\rangle + e^{-\frac{2\pi i}{3}} |0,2\rangle \right),$$

$$\phi^4 = (1/\sqrt{3}) \left(|1,0\rangle + e^{\frac{2\pi i}{3}} |0,1\rangle + e^{-\frac{2\pi i}{3}} |2,2\rangle \right),$$

$$\phi^5 = (1/\sqrt{3}) \left(|0,0\rangle + e^{\frac{2\pi i}{3}} |2,1\rangle + e^{-\frac{2\pi i}{3}} |1,2\rangle \right),$$

$$\phi^6 = (1/\sqrt{3}) \left(|2,0\rangle + e^{-\frac{2\pi i}{3}} |1,1\rangle + e^{\frac{2\pi i}{3}} |0,2\rangle \right),$$

$$\phi^7 = (1/\sqrt{3}) \left(|1,0\rangle + e^{-\frac{2\pi i}{3}} |0,1\rangle + e^{\frac{2\pi i}{3}} |2,2\rangle \right),$$

$$\phi^8 = (1/\sqrt{3}) \left(|0,0\rangle + e^{-\frac{2\pi i}{3}} |2,1\rangle + e^{\frac{2\pi i}{3}} |1,2\rangle \right).$$

The quality of the teleported state will be measured in terms of fidelity. The fidelity of two states is given by

(29-30)

$$F(\rho_{in}, \rho_{out}) = \{Tr[\sqrt{\sqrt{\rho_{in}} \rho_{out} \sqrt{\rho_{in}}}] \}^2 \quad (14)$$

where ρ_{in} is the input state of the channel and ρ_{out} is the output state of the channel.

We have plotted the fidelity as function of time for various values of Γ in Figure 5. It is observed that the fidelity is decreased by passing time. The amplitude of fluctuation is decreasing function of Γ .

We have plotted the fidelity for various values of χ in Figure 6. It is observed that the frequency of the fluctuation of fidelity is increasing function of χ . The fidelity is decreased rapidly for smaller χ in average.

We have studied the effects of magnetic fields by using Hamiltonian \mathbf{H}_1 . We have plotted this fidelity as function of time in the presence of magnetic field in Figure 7. It is observed that the magnetic fields effectively optimize the fidelity. For smaller value of χ , the magnetic fields cause to increase the fidelity

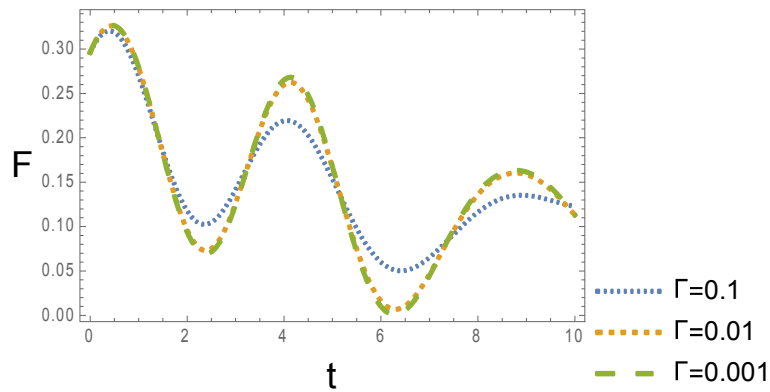


Figure 5. Fidelity as a function of time for various values of Γ for $\chi = 1$.

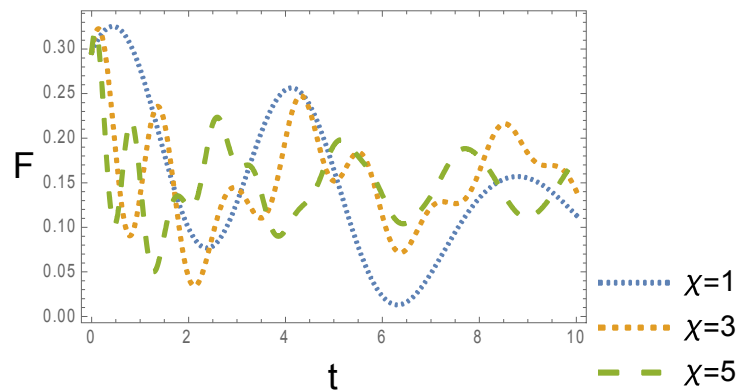


Figure 6. Fidelity as a function of time for various values of χ for $\Gamma = 0.02$.

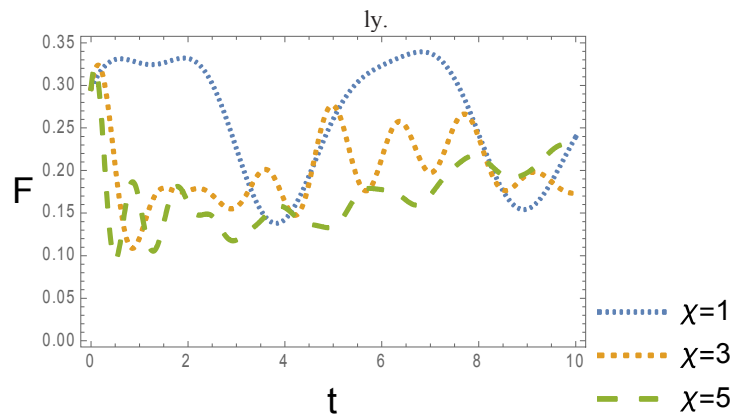


Figure 7. Fidelity as a function of time for various values of χ for $\Gamma = 0.02$, $B=1$.

effectively.

Results and Discussion

In both the presence and absence of a magnetic field, we investigated the dynamics of entanglement in a two-qutrit state governed by the OAT Hamiltonian with the inherent decoherence effects. The analysis of the results showed that the entanglement is decreasing function of both the intrinsic decoherence parameter Γ and the Hamiltonian coefficient χ . Besides, the entanglement is an increasing function of magnetic field and the entanglement goes to constant value with the passage of time.

We studied the teleportation via this entangled spin chain. We observed that the fidelity is decreasing function of parameter Γ . The reason is that the coherence of the system can be preserved in longer time with smaller decoherence parameter therefore the entanglement and fidelity can be enhanced by decreasing the coherence parameter. Additionally, the magnetic field has an impact on fidelity, making this effect more advantageous at lower parameter values. Because the magnetic field makes the spins rotate, they may be correlated. It is observed that with the increase or decrease of the entanglement, the fidelity of channel correspondingly goes up or down. Nevertheless, We deduce that one-axis counter-twisting Hamiltonian generates the entangled states, and it is useful for teleportation in virtue of these qutrit channels.

Considering the application of the teleportation in the transmitting of encoding quantum information and the security of the transfer of high-fidelity information, by manipulating the parameters appropriately, we can have a high-fidelity channel for the transfer of desired states. Furthermore, this channel using one-axis counter-

twisting Hamiltonian can be maximally entangled.

Acknowledgement

We are grateful to the Research Council of Shahid Chamran University of Ahvaz for financial support (GN: SCU.SP1401.12469).

References

1. Nielsen M. A and Chuang I. L. Quantum computation and quantum information. Cambridge university Press 2000.
2. Bouwmeester D, Mattle K, Pan J.W, Weinfurter H, Zeilinger A and Zukowski M. Experimental quantum teleportation of arbitrary quantum states. *Appl Phys B*. 1998;67:749.
3. Bennett C. H and Wiesner S. J. Communication via one and two particle operators on Einstein-Podolsky-Rosen states. *Phys Rev Lett*. 1992;69:2881.
4. Mattle K, Weinfurter H, Kwiat P. G and Zeilinger A. Dense Coding in Experimental Quantum Communication. *Phys Rev Lett*. 1996;76:4546.
5. Schumacher B. Quantum coding. *Phys Rev A*. 1995;51:2738.
6. Bennett C. H, Brassard G, Crepeau C, Jozsa R, Peres A and Wootters W. K. Teleporting an unknown quantum state via dual classical and Einstein- Podolsky- Rosen channels. *Phys Rev Lett*. 1993;70:1895.
7. Kitagawa M and Ueda M. Squeezed spin states. *Phys Rev A*. 1993;47(6):5138-5143.
8. Naji A and Jafarpour M. Squeezing and entanglement in multi-qutrit systems. *Quant Info Process*. 2013;12:2917-2933.
9. Naji A, Shadman N. Generation of entanglement in multi-qutrit systems by nonlinear Hamiltonian. *J Sci Islam Repub Iran*. 2022;32(4).
10. Duan LM, Cirac J. I and Zoller P. Quantum entanglement in spinor Bose-Einstein condensates. *Phys Rev A*. 2002;65:033619.
11. Sorensen A and Molmer K. Spin-spin interaction and spin squeezing in an optical lattice. *Phys Rev Lett*.

- 1999;83:2274.
12. Xi XY, Cheng WW, Huang YX. Entanglement and quantum teleportation in a three-qubit Heisenberg chain with three-site interactions. *Quantum Inf Process.* 2015;14(7):2551-2562.
 13. Zheng L and Zhang G. Intrinsic decoherence in Jaynes-Cummings model with Heisenberg exchange interaction. *Eur Phys J. D* 2017;71:288.
 14. Naderi N, Bordbar M, Hasanvand F. K and Chamgordani A. M. Intrinsic of inhomogeneous magnetic field on the qutrit teleportation via XXZ Heisenberg chain under intrinsic decoherence. *Int J Light Electron Opt.* 2021;247:167948.
 15. Song W. Effect of intrinsic decoherence on entanglement of a two-qutrit 1D optical lattice chain with nonlinear coupling. *Chinese Physics B.* 2009;18(8):3251-3257.
 16. Joos E, Zeh H. D, Kiefer C, Giulini D, Kupsch J and Stamatescu I. O. *Decoherence and the Appearance of a Classical World in Quantum Theory.* Springer Press, 2nd edition 2003.
 17. Milburn GJ. Intrinsic decoherence in quantum mechanics. *Phys Rev A.* 1991;44:5401-5406.
 18. Caves C. M and Milburn G. J. Quantum-mechanical model for continuous position measurements. *Phys Rev D.* 1987;36:5543.
 19. Milburn GJ. Kicked quantized cavity mode: An open systems theory approach. *Phys Rev A.* 1987;36:744.
 20. Jiang C, Wei YZ, Jiang M. Teleportation of an arbitrary two-qubit state via four-qubit cluster state in noisy environment. *Int J Theor Phys.* 2022;61:154.
 21. Qin M and Ren Z. Z. Influence of intrinsic decoherence on entanglement teleportation via a Heisenberg XYZ model with different Dzyaloshincki-Moriya interaction. *Quantum Info Process.* 2015;14:2055-2066.
 22. Bin S, Tian-Hai Z, Jian Z. Influence of intrinsic decoherence on entanglement in two-qubit quantum Heisenberg XYZ chain. *Commun. Theor Phys (Beijing China).* 2005;44:255-258.
 23. Mohammadi H, Akhtarshenas SJ, Kheirandish F. Influence of dephasing on the entanglement teleportation via a two-qubit Heisenberg XYZ system. *Eur Phys J D.* 2011;62:439-447.
 24. Guo J. L, Xia Y and Song H. S. Effects of Dzyaloshinski-Moriya anisotropic interaction on entanglement and teleportation in a two-qubit Heisenberg chain with intrinsic decoherence. *Opt Commun.* 2008;281:2326.
 25. Zheng L and Feng Zhang G. Intrinsic decoherence in Jaynes-Cummings model with Heisenberg exchange interaction. *Eur Phys J D.* 2017;71:288.
 26. Vidal G and Werner R. F. Computable measure of entanglement. *Phy Rev A.* 2002;65:032314.
 27. Carteret H. A. Noiseless quantum circuits for the Peres separability criterion. *Phys Rev Lett.* 2005;94:040502.
 28. Bowen G and Bose S. Teleportation as a depolarizing quantum channel, relative entropy, and classical capacity. *Phys Rev Lett.* 2001;87:267901.
 29. Jozsa R. Fidelity for mixed quantum states. *J Mod Opt.* 1994;41:2315.
 30. Bowdrey MD, Oi DKL, Short AJ, Banaszek K, Jones JA. Fidelity of single qubit maps. *Phys Lett A.* 2002;294:258.

PERSIAN TRANSLATION OF ABSTRACTS

چکیده‌های فارسی

Formulation and Evaluation of Gelatin Nanoparticle Moisturizing Gel from Mesocarp Extract of Watermelon [*Citrullus lanatus* (Thunb.) Matsum. & Nakai] as an Antioxidant

S. D. Okzelia^{1*}, S. A. Azzahara¹, K. Kosasih², and S. I. Yanti¹

¹Department of Pharmacy, Sekolah Tinggi Ilmu Kesehatan Bani Saleh, Bekasi, Indonesia

²Faculty of Pharmacy, Universitas Pancasila, Jakarta, Indonesia

*Email: defi@stikesbanisaleh.ac.id

فرمولاسیون و ارزیابی ژل مرطوب کننده نانوذرات ژلاتین از عصاره مزوکارپ هندوانه [*Citrullus lanatus* (Thunb.) Matsum. & Nakai] به عنوان یک آنتی اکسیدان

ساری دفی اکزلیا^{۱*}، سمیتا آلیفیا آلزهره^۱، کوساسی کوساسیه^۲ و سیلفرا ایندرا یانتی^۱

^۱گروه داروسازی، سکولا تیگی ایلمو کسهاتم صالح، بکاسی، اندونزی

^۲گروه داروسازی، دانشگاه پانکاسیلا، جاکارتا، اندونزی

چکیده

پوست انسان توسط رادیکال‌های آزاد مورد حمله قرار می‌گیرد، بنابراین آنتی‌اکسیدان‌ها برای ترمیم مورد نیاز هستند. مزوکارپ هندوانه [*Citrullus lanatus* (Thunb.) Matsum. & Nakai] دارای ترکیبات آنتی‌اکسیدانی طبیعی مانند سیتروپولین است. ترکیبات آنتی‌اکسیدانی برای تهیه ژل با فناوری نانو ذرات فرموله شدند که هدف تسهیل جذب ماده فعال است. هدف این مطالعه فرمولاسیون ژل مرطوب‌کننده آنتی‌اکسیدانی حاوی نانوذرات ژلاتینی عصاره مزوکارپ هندوانه (GNMW) است. مراحل تحقیق شامل استخراج، تولید و تعیین خصوصیات نانوذرات، فرمولاسیون ژل با غلظت‌های مختلف (F1) ۰,۰۱۱۴٪، (F2) ۰,۰۲۲۸٪ و (F3) ۰,۰۳۴۲٪، ارزیابی آماده سازی ژل، مشاهده آنتی‌اکسیدان بود. با استفاده از روش DPPH و تست رطوبت پوست. نانوذرات تولید شده دارای شکل نامنظم، اندازه ۲۰۰,۳ نانومتر، شاخص پلی پراکندگی ۰,۲۸۸ و ارزش پتانسیل زتا ۱۶,۱۱ میلی ولت بودند. ژل نانوذرات دارای بافت کمی چسبناک، رنگ شفاف و همگن با مقدار ۶.۶۱ - ۷.۲۲ pH بود. ویسکوزیته ۱۴۷۴۰ - ۱۷۱۸۰ cP. قابلیت پخش ۵,۳-۶,۵ سانتی متر داشته و پوست را تحریک نمی‌کند. نتایج فعالیت آنتی‌اکسیدانی عصاره و نانوذرات به ترتیب ۱۱۰/۹۰ میکروگرم بر میلی‌لیتر و ۱۱۴/۱۶ میکروگرم بر میلی‌لیتر بود. ژل نانوذرات F1، F2 و F3 به ترتیب دارای مقادیر IC50 ۱۴۹.۵۲ میکروگرم بر میلی‌لیتر، ۱۳۸,۴۴ میکروگرم بر میلی‌لیتر و ۱۲۷,۱۰ میکروگرم بر میلی‌لیتر بودند. ژل‌ها می‌توانند رطوبت پوست را در محدوده ۳۸,۸۱٪ تا ۶۳,۱۹٪ افزایش دهند. عصاره مزوکارپ هندوانه که با حامل ژلاتین به نانوذرات تبدیل می‌شود، می‌تواند به صورت یک ژل مرطوب‌کننده فرموله شود، استانداردهای یک ژل خوبی را دارا بوده و فعالیت آنتی‌اکسیدانی متوسطی دارد.

واژه‌های کلیدی: ژل مرطوب کننده نانوذرات؛ GNMW؛ ژل آنتی‌اکسیدانی نانوذره

Anticancer Effect and Safety Profile of a 4-Pyridyl Linked Triazolotriazine Derivative against Colorectal Tumor

R. Monfared¹, S. Farzipour^{2,3}, S. Dadashpour¹, Z. Zakeri Khatir¹, S. J. Hosseinimehr^{3*}, F. Talebpour Amiri⁴, H. Irannejad^{1*}

¹ Department of Medicinal Chemistry, Faculty of Pharmacy, Mazandaran University of Medical Sciences, Sari, Islamic Republic of Iran

² Cardiovascular Diseases Research Center, Department of Cardiology, Heshmat Hospital, School of Medicine, Guilan University of Medical Sciences, Rasht, Islamic Republic of Iran

³ Department of Radiopharmacy, Faculty of Pharmacy, Mazandaran University of Medical Sciences, Sari, Islamic Republic of Iran

⁴ Department of Anatomy, Faculty of Medicine, Molecular and Cell Biology Research Center, Mazandaran University of Medical Sciences, Sari, Islamic Republic of Iran

*Email: sjhosseinim@yahoo.com, sjhosseinim@mazums.ac.ir

** Email: irannejadhamid@gmail.com

اثر ضد سرطانی و ایمنی مشتق تری آزولوتری آزین حاوی بخش ۴-پیریدیل در برابر تومور روده

ریحانه منفرد^۱، صغری فرضی پور^{۲،۳}، سکینه داداش پور^۱، زهرا زاگری خطیر^۱، سیدجلال حسین مهر^{۳*}، فرشته طالب پورامیری^۴، حمید ایران نژاد^{۱*}

^۱ گروه شیمی دارویی، دانشکده داروسازی، دانشگاه علوم پزشکی مازندران، ساری، جمهوری اسلامی ایران

^۲ گروه قلب و عروق، مرکز تحقیقات بیماری های قلب و عروق، بیمارستان حشمت، دانشکده پزشکی، دانشگاه علوم پزشکی گیلان، رشت، جمهوری اسلامی ایران

^۳ گروه رادیو فارماسی، دانشکده داروسازی، دانشگاه علوم پزشکی مازندران، ساری، جمهوری اسلامی ایران

^۴ گروه تشریح، مرکز تحقیقات بیولوژی مولکولی و سلولی، دانشکده پزشکی، دانشگاه علوم پزشکی مازندران، ساری، جمهوری اسلامی ایران

چکیده

سرطان دومین عامل مرگ و میر درجهان است و سرطان روده جزء چهارمین شایع در کل دنیا به شمار می‌رود. در این مطالعه، اثر ضد سرطانی و ایمنی ترکیب **۱۰b** با هسته مرکزی تریازولوتری آزین که دارای یک بخش ۳-پیریدین ۴-ایل متیل تیو است، بر روی سلولهای سرطانی روده (HT-29) مورد ارزیابی قرار گرفت. ارزیابی سلولی، IC_{50} پاکلیتاکسل و ترکیب **۱۰b** را پس از ۷۲ ساعت به ترتیب ۰/۳۴ و ۸/۹۲ میکرومولار نشان داد. برای تأیید اثر ضد سرطانی درون تنی ترکیب **۱۰b**، از موش‌های زئوگرافت حامل تومورهای روده انسانی استفاده شد. موش‌های حامل تومور به مدت ده روز با ترکیب **۱۰b** و پاکلیتاکسل تحت درمان قرار گرفتند، سپس کالبدشکافی شدند و بافت قلب، کبد و تومور آنها برای ارزیابی پاتولوژی جدا شد. وزن موش و اندازه تومور روزانه اندازه گیری شد و مرگ و میر ثبت شد. نتایج اندازه‌گیری وزن موش‌ها و اندازه تومور، تغییرات معنی‌داری را در گروه‌های تحت درمان با ترکیب **۱۰b** نشان ندادند. بررسی‌های پاتولوژیک نشان داد که میزان سمیت کبدی و قلبی در موش‌های دریافت کننده ترکیب **۱۰b** کمتر از گروه پاکلیتاکسل بود. جالب و امیدوارکننده است که تمام موش‌های تحت درمان با ترکیب **۱۰b** در طول آزمایش زنده ماندند اما ۵۰ درصد از موش‌های تحت درمان با پاکلیتاکسل و همچنین ۵۰ درصد از موش‌های گروه کنترل فوت شدند. در مجموع، ترکیب **۱۰b** فعالیت ضد توموری قابل قبولی را در شرایط آزمایشگاهی روی سلول‌های روده HT-29 نشان داد و فقدان مرگ و میر در این گروه، ایمنی ترکیب **۱۰b** را تأیید می‌کند.

واژه‌های کلیدی: سرطان روده؛ تری آزولوتری آزین؛ HT-29؛ زئوگرافت؛ تومور

Microstructures and Crystal Size Distribution (CSD) of Chromites from Gysian Silvana Ophiolite Serpentinites, Urmia, Iran

M. Modjarrad*

Department of Geology, Faculty of Sciences, Urmia University, Urmia, Islamic Republic of Iran

*Email: m.modjarrad@urmia.ac.ir

ریزساخترها و توزیع ابعاد بلوری (CSD) کرومیت های سرپانتینیت افیولیت گیسیان سیلوانا، ارومیه، ایران

منیره مجرد *

گروه زمین شناسی، دانشکده علوم، دانشگاه ارومیه، ارومیه، جمهوری اسلامی ایران

چکیده

یکی از اجزاء افیولیت گیسیان سیلوانا در جنوب ارومیه (نزدیکی مرز ایران با ترکیه و عراق) و در ادامه روند نئوتتیس در شمالغرب ایران، سرپانتینیت ها هستند که دارای لیزاردیت/کریزوتیل و مگنتیت بعنوان فازهای اصلی و کرومیت (کروم اسپینل) و اندکی الیوین و ارتوپیروکسن می باشند. ریزساخترهای متعددی از قبیل غربالی، تیغه ای، رشته ای و ساعت شنی در این واحد دیده شده است. وجود صفحات [001] لیزاردیتی در حاشیه هسته های کمتر متبلور شده بافت شبکه ای از دیگر بافتها در این سنگها می باشد. از آنجا که آنتی گوریت در این سنگها وجود ندارد، لذا عمق فرورانش تختال نئوتتیس در این بخش از ایران احتمالاً کم بوده است. در این پژوهش، پراکنش ابعاد بلوری کرومیت های سرپانتینیت گیسیان مطالعه شده است. سه نوع الگوی CSD برای کرومیت ها شناسایی و پارامترهای هسته بندی و رشد آنها از روی مقادیر عرض از مبدأ و شیب منحنی استخراج شده است. نوع اول الگوی خطی داشته و نسبت نرخ هسته بندی به رشد (J/G) در آن حدود ۱۲ و Gt آن ۱/۲۸، نوع دوم دارای تحذب و غیر خطی بوده که در نتیجه جوش خوردگی یا درشت شدگی استوالد در بخش دانه ریزها بوده و J/G در آن ۱۳ تا ۱۵ و Gt آن ۱/۳۳ می باشد. نوع سوم پیچیده بوده و دو جمعیت آماری در دو بخش مجزا را نشان داده و در آن دانه ریزها و دانه درشت ها با دو قطعه الگوی خطی همپوشانی دارند. نرخ هسته بندی به رشد دانه ریزها دو برابر دانه درشت ها بوده و بدلیل هسته های بسیار، رشد ناچیز بوده است. Gt برای دانه ریزها ۱/۶ و برای دانه درشت ها ۱/۱ بوده است. با در نظر گرفتن نرخ رشد ثابت 10^{-9} سانتیمتر بر ثانیه برای بلورهای سیلیکاته، زمان برای رشد بلورهای درشت ۶ برابر بلورهای ریز بوده است. چنین الگوی CSD دو تکه ممکن است نشانه ای از فرایندهای حین صعود بوده یا دانه های ریز محصول دگرسانی کانیهای مافیک دیگر و غیر اولیه باشند.

واژه های کلیدی: کرومیت؛ CSD؛ گیسیان؛ ارومیه؛ ایران

Heavy Tailed Distribution of Binary Classification Model

D. M. Oladimeji*, E. S. Oguntade, S. O. Olarenwaju

Department of Statistics, Faculty of Sciences, University of Abuja, Abuja, Nigeria

**Email: oladimejidamilare@yahoo.com*

توزیع دم‌سنگین برای مدل طبقه‌بندی دوتایی

اولادیمجی، د. م.*، اوگونتاد، ای. س.، اولارنواجو، س. و.

گروه آمار، دانشکده علوم، دانشگاه ابوجا، ابوجا، نیجریه

چکیده

در این پژوهش توزیع چوله دم‌سنگین وارون وایبول به عنوان یک تابع پیوند در مدل طبقه‌بندی دوتایی معرفی می‌شود. انگیزه این انتخاب نیاز به رویدادهای نادر یا فرین در فرآیندهای تصادفی است. در این مطالعه مدلی معرفی می‌شود که مبتنی بر توزیع وارون وایبول (نوع دوم) است و پارامترهای آن با روش‌های ماکسیمم درست‌نمایی برآورد می‌شوند. وقتی خروجی‌ها با نتایج حاصل از سایر توابع پیوند مانند توزیع‌های وایبول نوع اول و نوع سوم مبتنی بر توزیع‌های مقادیر فرین با استفاده از داده‌های طبقه‌بندی استاندارد و همچنین داده‌های واقعی مقایسه می‌شوند، مشخص می‌شود که توزیع وارون وایبول (نوع دوم) عملکرد استثنایی از خود نشان می‌دهد. این ارزیابی عملکرد چندین معیار شامل معیار اطلاعات آکایک، معیار اطلاعات بیزی، مساحت زیر منحنی و امتیاز بریر را در نظر می‌گیرد. بخش نتیجه‌گیری، بیانگر آن است که مدل پیشنهادی نیرومندی قابل توجهی را در عملکرد خود نشان می‌دهد و آن را به یک انتخاب مناسب برای مدل‌سازی مسائل طبقه‌بندی دوتایی تبدیل می‌کند.

واژه‌های کلیدی: توزیع مقادیر فرین؛ وارون وایبول؛ مدل طبقه‌بندی؛ توزیع دم‌سنگین

Bootstrap Confidence Intervals for the Parameter of the Poisson-Sujatha Distribution and Their Applications to Agriculture

W. Panichkitkosolkul^{1*} and Ch. Ponkaew²

¹ Department of Mathematics and Statistics, Thammasat University, Pathumthani, 12120 Thailand

² Department of Mathematics, Faculty of Science and Technology, Phetchabun Rajabhat University, Phetchabun, 67000 Thailand

* Email: wararit@mathstat.sci.tu.ac.th

فواصل اطمینان بوت استرپ برای پارامتر توزیع پواسون-سوجاتا و کاربرد آنها در کشاورزی

واراریت پانیچکیتکوسولکول^{۱*} و شوجیات پنکااو^۲

^۱ گروه ریاضی و آمار، دانشگاه تاماسات، پاتوتانی، ۱۲۱۲۰، تایلند

^۲ گروه ریاضی، دانشکده علوم و تکنولوژی، دانشگاه پتاج بون، پتاج بون، ۶۷۰۰۰، تایلند

چکیده

در برخی از موقعیت‌های دنیای واقعی، فرد با داده‌های شمارشی با پراکندگی بیش از حد مواجه می‌شود به طوری که توزیع پواسون معمولی با داده‌ها مطابقت ندارد. در شرایط فعلی، استفاده از ترکیبی از توزیع‌های Poisson و Poisson-Sujatha (PS) مناسب است. توزیع PS برای داده‌های شمارشی مورد بررسی قرار گرفته است، که مورد توجه تعدادی از رشته‌ها، از جمله زیست‌شناسی، پزشکی، جمعیت‌شناسی، و کشاورزی است. با این حال، هیچ تحقیقی در مورد ایجاد فواصل اطمینان بوت استرپ برای پارامتر آن انجام نشده است. احتمالات پوشش و میانگین طول فواصل اطمینان بوت استرپ به دست آمده از روش‌های صدک، پایه و بایاس تصحیح و شتاب بوت استرپ با استفاده از شبیه‌سازی مونت کارلو مقایسه شد. نتایج نشان داد که دستیابی به سطح اطمینان اسمی با استفاده از فواصل اطمینان بوت استرپ برای اندازه‌های نمونه کوچک، بدون توجه به تنظیمات دیگر، غیرممکن است. علاوه بر این، زمانی که حجم نمونه بزرگ بود، تفاوت زیادی در عملکرد چندین بازه اطمینان بوت استرپ وجود نداشت. فاصله اطمینان بوت استرپ تصحیح شده و تسریع شده عملکرد برتر را در مقایسه با روش‌های دیگر در همه موارد مورد بررسی نشان داد. علاوه بر این، اثربخشی فواصل اطمینان راه‌اندازی از طریق کاربرد آنها در مجموعه داده‌های کشاورزی ثابت شد. محاسبات شواهد قابل توجهی را به نفع فواصل اطمینان بوت استرپ پیشنهادی ارائه می‌دهد.

واژه‌های کلیدی: تخمین بازه‌ای؛ توزیع پواسون؛ توزیع مختلط؛ داده‌های شمارش؛ روش بوت استرپ

Qutrit Teleportation and Entanglement Evolved by the One-axis Counter-Twisting Hamiltonian under the Intrinsic Decoherence

A. Naji*

Department of Physics, Faculty of Sciences, Shahid Chamran University of Ahvaz, Ahvaz, Islamic Republic of Iran

**Email: a.naji@scu.ac.ir*

ترابرد و درهم‌تنیدگی کیوتریتی تحول یافته توسط هامیلتونی پیچش تک محوری تحت واہمدوسی ذاتی

آزیتا ناجی*

گروه فیزیک، دانشکده علوم، دانشگاه شهید چمران اهواز، اهواز، جمهوری اسلامی ایران

چکیده

در این مقاله درهم‌تنیدگی و ترابرد کوانتومی یک حالت دو-کیوتریتی تحت هامیلتونی پیچش تک محوری در حضور و غیاب میدان مغناطیسی با اثرات واہمدوسی ذاتی مطالعه شده است. درهم‌تنیدگی و وفاداری به صورت تابعی از پارامتر واہمدوسی ذاتی، ضریب هامیلتونی و میدان مغناطیسی بررسی شد. نتایج نشان داد که وفاداری و درهم‌تنیدگی هر دو تابعی از پارامتر واہمدوسی ذاتی و ضریب هامیلتونی هستند. هم‌چنین، در حضور میدان مغناطیسی منفیت و وفاداری به طور موثر بهبود می‌یابند. مطابق نمودارها وقتی که درهم‌تنیدگی کانال بیشینه است بهترین وفاداری توسط آن به دست می‌آید.

واژه‌های کلیدی: درهم‌تنیدگی؛ ترابرد؛ واہمدوسی ذاتی؛ هامیلتونی پیچش تک محوری

===== **JOURNAL OF SCIENCES** =====

ISLAMIC REPUBLIC OF IRAN

SUBSCRIPTION FORM

Please enter my annual subscription to the Journal of Sciences, Islamic Republic of Iran including 4 quarterly issues for the Year Vol. No.

	Iran	Other Countries
<input type="checkbox"/> Personal	R. 30,000	\$ 80.00
<input type="checkbox"/> Institutional	R. 40,000	\$ 100.00
<input type="checkbox"/> Student	R. 16,000	\$ 50.00
<input type="checkbox"/> Check enclosed		<input type="checkbox"/> Bill me

Name: _____ **City:** _____ **Country:** _____
Mailing Address: _____

Check or money order must be made to order of:
Journal of Sciences, Islamic Republic of Iran, University of Tehran
Enghelab Ave., P.O. Box 13145-478, Tehran, Iran

Payment can be made via our transfer account.

Iran: Account No. 5225458914 Mellat Bank, Branch of University of Tehran, Central Income of Vice President of Research.

Foreign: Account No. 162454986 tejarat Bank, Branch of University of Tehran, Islamic Republic of Iran.

* Please allow 6-8 weeks for delivery.

===== **JOURNAL OF SCIENCES** =====

ISLAMIC REPUBLIC OF IRAN

SUBSCRIPTION FORM

Please enter my annual subscription to the Journal of Sciences, Islamic Republic of Iran including 4 quarterly issues for the Year Vol. No.

	Iran	Other Countries
<input type="checkbox"/> Personal	R. 30,000	\$ 80.00
<input type="checkbox"/> Institutional	R. 40,000	\$ 100.00
<input type="checkbox"/> Student	R. 16,000	\$ 50.00
<input type="checkbox"/> Check enclosed		<input type="checkbox"/> Bill me

Name: _____ **City:** _____ **Country:** _____
Mailing Address: _____

Check or money order must be made to order of:
Journal of Sciences, Islamic Republic of Iran, University of Tehran
Enghelab Ave., P.O. Box 13145-478, Tehran, Iran

Payment can be made via our transfer account.

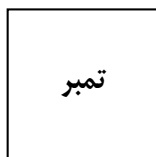
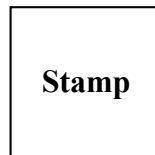
Iran: Account No. 5225458914 Mellat Bank, Branch of University of Tehran, Central Income of Vice President of Research.

Foreign: Account No. 162454986 tejarat Bank, Branch of University of Tehran, Islamic Republic of Iran.

* Please allow 6-8 weeks for delivery.

To:
Journal of Sciences
Islamic Republic of Iran

University of Tehran
Enghelab Ave., Tehran
P.O. Box 13145-478
Islamic Republic of Iran



گیرنده:
تهران - مجله بین المللی علوم پایه جمهوری اسلامی ایران
تهران، خیابان انقلاب، دانشگاه تهران،
صندوق پستی ۴۷۸ - ۱۳۱۴۵

Cover Legend:

“Abu Reyhan al-Biruni (973-1048) was one of the greatest scholars and philosopher in the history of Islamic civilization. He was equally well versed in a number of fields including mathematics, astronomy, physical and natural sciences, geography, history, chronology, and linguistics. George Sarton has called the first half of the 11th century «the age of Biruni». He wrote over 150 works, including 18 volumes on astronomy, 15 volumes on geography, 13 on literature, 12 volumes on astrology, 6 on religious ideology, 6 on astrolabes, 5 on timing devices, 5 on comets and 4 on the physics of light and optics. His scientific contributions also include the accurate determination of the density of eighteen different metals and minerals. He calculated the sine and cosine of angles from zero to 90 degrees and recorded them in a table. He made a remarkably accurate determination of the radius of the earth, which is very close to the latest estimate. He wrote dissertations regarding comets and meteorites, sun rays, light, twilight and dawn, time and space, astrolabes, methods to determine Qibla, the values of numerals, the relativity between precious stones and metals, ways of determining the longitude and latitude of cities, and the distances between them, and devised a method of measuring the earth’s circumference, and complex problems of trigonometry. In addition to his native language (Persian) he also mastered Arabic, Sanskrit, Hebrew, Greek, Syriac and Turkish.”

“Ref.: Noori-Dalooi, M.R., J. Sci. I.R. Iran, Vol. 1, No. 1, pp. 2-3,. Autumn 1988”

JOURNAL OF SCIENCES

ISLAMIC REPUBLIC OF IRAN

University of Tehran

**Indexed by Thomson Reuters, Scopus, Islamic World Science
Citation Center (ISC), Scientific Information Database (SID)
and/Abstracted in**

Biological Abstracts

Biosis Selective Coverage Unique

Biosis Previews

Zoological Records

Chemical Abstracts

Methods in Organic Synthesis

Mathematical Reviews

Current Mathematical Publications

MathSciNet